ON THE EVOLUTION OF A DETACHING RETINA: MECHANICS, MATHEMATICAL MODELING, AND ANALYSIS

by

JOSEPH M. LAKAWICZ

A dissertation submitted to the

School of Graduate Studies

Rutgers, The State University of New Jersey

in partial fulfillment of the requirements

for the degree of

Doctor of Philosophy

Graduate Program in Mechanical & Aerospace Engineering

Written under the direction of

William J. Bottega

and approved by

———————————————

———————————————

———————————————

———————————————

New Brunswick, New Jersey

OCTOBER, 2018

ABSTRACT OF THE DISSERTATION

ON THE EVOLUTION OF A DETACHING RETINA: MECHANICS, MATHEMATICAL MODELING, AND ANALYSIS

By JOSEPH M. LAKAWICZ

Dissertation Director:

William J. Bottega

Retinal detachment is an affliction of the eye in which the nine layers of the neurosensory retina detach from the outer layers of the eye along its interface with the retinal pigment epithelium. This dissertation represents a study of the application of mechanics based mathematical modeling to age-related and myopia-induced retinal detachments. A review of the theory of shells of arbitrary shape which provides clarification on the change in curvature of the shell is also presented. A corresponding multi-directional growth law for the propagation of detachments of arbitrary shape is established.

A mechanics based mathematical model for retinal detachment in the emmetropic eye that takes contraction of the vitreous and extension of its fibrils, along with a pressure difference across the retina, as the impetus for detachment propagation is presented. A second mechanics based mathematical model for retinal detachment due to the geometric changes of the eye associated with the evolution of myopia is also developed. The model for myopic retinal detachment includes deformation of the retina due to biological growth of the retina, as well as elastic deformation imposed on the retina by the myopic change in shape of the much stiffer choroid and sclera. The models are formulated as propagating boundary value problems in the calculus of variations. This approach yields the self-consistent governing equilibrium equations, boundary conditions, and transversality conditions that establish the

location of the propagating boundaries that correspond to equilibrium configurations of each the detaching ocular systems. Axisymmetric conditions are considered and exact analytical solutions to the corresponding boundary value problems are obtained for detaching retinas with and without a tear. The effects of changes in material and geometric parameters, as well as the influence of the presence and size of the retinal tear, on detachment propagation are also studied.

The emmetropic model predicts that retinal detachment propagates catastrophically, which is in agreement with clinical observations. From application of the emmetropic model presented herein, a value of the bond energy of the retina to retinal pigment epithelium interface is estimated using material properties found in the literature. Simulations based on the analytical solutions for the myopic model of the detaching retina are performed for a detachment in the retina located at either the posterior or superior pole of the eye. The results support the clinical finding of an increased prevalence of retinal detachment in myopic eyes and provide insight into the potential causation for the increased prevalence.

Acknowledgements

I would first and foremost like to thank my advisor, Dr. William J. Bottega, for his teachings, guidance, and assistance in the research and writing of this dissertation. I would also like to thank Dr. Haym Benaroya, Dr. Haim Baruh, and Dr. Howard Fine for serving on my doctoral committee and for their thoughts and comments in their review of the dissertation. Cynthia Cartegna is to be thanked for her help and support in the submission process. Also, thanks to my peers, Michael Pavlou, Peinan Ge, Peter Balogh, and Dan Cordasco, for their thoughts on and contributions to my research.

I would like to acknowledge and thank my wife, Alaina, for her love and support throughout my academic studies. The time I have invested into my research and dissertation required great patience and compromise on her part. I also want to thank my parents, Joe and Rosemarie, my brother Adam, and my sister Erika for their love and support during my academic studies.

Table of Contents

List of Tables

List of Figures

Chapter 1

Introduction

1.1 Motivation

Retinal detachment is an affliction of the eye in which the nine layers of the neurosensory retina detach from the outer layers of the eye along its interface with the retinal pigment epithelium (RPE). The RPE remains securely attached to the choroid on the inner surface of the eye, while the choroid in turn remains attached to the sclera. Common risk factors for retinal detachment include advanced age, myopia, cataract surgery, and trauma. Patients experiencing retinal detachment may experience light flashes, floaters, peripheral visual field loss, and blurred vision (Gariano & Kim [25]). Surgical intervention is often successful at restoring visual acuity when the detachment does not involve the clinical macula but detachment involving the macula often has a permanent adverse effect on vision (Wilkinson & Rice [84]).

Retinal detachments are classified as exudative, tractional, or rhegmatogenous (see, for example Gariano & Kim [25]). Exudative retinal detachment occurs due to an accumulation of fluid in the subretinal space, which is often the result of an underlying disease. Tractional retinal detachment results from mechanical forces on the retina that arise from the fibrotic scar tissue associated with previous hemorrhage, injury, surgery, infection of inflammation. Rhegmatogenous retinal detachment (RRD) is the most common type and occurs when a tear forms in the retina, allowing fluid to enter the subretinal space. In a review of epidemiology studies concerning RRD dating from 1970 to 2009, Mitry *et al.* [52] found a median annual incidence rate of 1.05 per 10,000 of population. Incidence varied with geographical population, but the largest annual incidence of RRD occurred in the 60-70 year age group with a secondary peak in young myopic patients.

The vitreous body is the most important intraocular tissue in the pathogenesis of retinal

detachment (Wilkinson & Rice [84]). In young healthy eyes, the vitreous body is composed of a gel that fills the vitreous cavity and is randomly interspersed with collagen fibrils. As the eye ages, the vitreous liquefies leading to the collapse of the matrix of collagen fibrils which, in turn exerts traction on the vitreoretinal interface (Sebag [71]). Often the vitreous will separate from the retina in an acute manner beginning at the posterior of eye, which is know as posterior vitreous detachment (PVD). The traction acting on the retina from the vitreous fibrils in addition to the onset of PVD are factors that predispose elderly patients to retinal tears and RRD.

Retinal detachment is also known to have a much higher prevalence in individuals with myopic eyes when compared to individuals with emmetropic or hyperopic eyes (Wilkinson & Rice [84]). According to Wilkinson & Rice [84], RRD is associated with the risk factors of vitreous liquefaction, PVD, and lattice degeneration. These risk factors are also more prevalent in myopic eyes than non-myopic eyes (Akiba [1] and Celorio & Pruett [13]). Myopic foveoschisis is another common complication affecting eyes with high myopia and is often accompanied by foveal retinal detachment without the presence of a macular hole (Alkuraya [2]).

This dissertation presents a study of the application of mechanics based mathematical modeling to age-related and myopia-induced retinal detachments. A brief summary of some applications of theoretical fluid and solid mechanics to the ocular system is found in Gonzalez & Fitt [30], in which tonometry, scleral buckle surgery, and retinal detachment was considered. The following section shows a more complete review of the literature concerning the application of mechanics and mathematical modeling to the study of the ocular system, with a focus on retinal detachment specifically.

1.2   A Survey of Relevant Literature

Some of the earliest work in the literature concerned with applying the principals of mechanics to the ocular system was done in studying the relationship between force/displacement and intraocular pressure (IOP) in tonometry. Friedenwald [24] modeled the cornea as a shell using membrane theory which assumes that the corneal tissue provides no resistance

to bending. The author however comments that the results of the model suggest that the cornea does offer a small but real resistance to bending. Schwartz *et al.* [70] later approached the same problem by modeling the cornea using a shallow shell theory that includes the effects of transverse shear (Naghdi [55]) to accurately model the pressure distribution that arises between the indenter and the cornea. Seeking to improve the model of tonometry, Mow [54] applied a small deflection sandwich-shell theory (Reissner [61]) to better incorporate the material properties of the layers of the cornea. Finite element modeling was applied to this problem by Kobayashi *et al.* [40] to incorporate the nonspherical geometry and nonhomogenous material properties of the corneo-sclera shell and was later advanced in Woo *et al.* [86] to incorporate nonlinear elastic material properties.

In seeking a mechanical explanation for the onset of myopia, Greene [31] studied the stress exerted on the posterior sclera from the extraocular muscles, as well as the stress that would develop in the sclera from changes in IOP during accommodation and convergence. The author took the stress that developed in the sclera to be the superposition of the stress in a spherical pressure vessel resulting from the IOP with the stress field resulting from a point force acting on a flat plate for the extraocular muscles. Consideration was given to the optic nerve by a discussion of the stress concentration that develops in a plate with a circular hole. Another model considering mechanical forces is found in Michels *et al.* [50], where the authors provide a discussion of the forces in epiretinal membranes that can facilitate retinal detachment. The authors also discuss the effect that application of a scleral buckle has on these forces in order to potentially bring the detached retina back into contact with the RPE. In other studies on retinal reattachment, Voltairas *et al.* [80] modeled reattachment due to the magnetic forces between a magnetic silicone band and a silicone ferrofluid internal tamponade. In their two dimensional model, a retina with a tear is represented by a rigid rod hinged at one end. Foster & Chou [22] studied the interaction of surface tension and buoyancy forces in retinal reattachment through injection of gas or perfluoron into the eye during pneumatic retinopexy, with the retina modeled as a two dimensional flap.

The deformation of the eye due to the application of a cerclage is studied in Keeling *et al.* [39], where the eye is modeled as a spherical elastic membrane that is filled with an

incompressible fluid. The cerclage is modeled as a linear elastic cylindrical band applied around the eye and the resulting intraoperative and postoperative shape of the eye is determined through minimization of a potential energy functional. The shape of the eyeball after application of an elastic scleral buckle is also determined in Ismail *et al.* [35] by modeling the eye as a spherical membrane. Foster *et al.* [23] studied the effects of the fluid motion of the vitreous after application of a scleral buckle. The authors modeled this system by laminar flow over a flat plate with an indentation that represented the indentation in the eye wall due to the scleral buckle. The retina was modeled as a flat elastic membrane initially separated from the eye wall and finite element simulations were performed. Finite element models for the shape of the eye after application of segmented scleral buckles and encircling scleral buckles are found in Wang *et al.* [83] and Lanchares *et al.* [44], respectively.

David *et al.* [17] modeled the eye wall as a thin isotropic spherical shell and studied the axisymmetric vibrational response induced on the eye by the external muscles during saccadic motion. The muscles were modeled as band loading acting around the equator and the saccades were given by a step function. The authors varied the radius of the eye and the tissue thickness and found that the stress in the eye wall increases with increasing eye radius and decreasing tissue thickness. They proposed this as an explanation for why myopic eyes have a larger tendency toward retinal detachment. Subsequently, David *et al.* [18] represented saccadic motion as a sine wave and presented the corresponding analytical viscoelastic and numerical Newtonian solutions for the fluid motion of the spherical vitreous cavity. The authors evaluated the time-dependent fluid shear stress acting on the eye wall and found larger shear stress with increasing eye size.

The stress exherted on the retina by a vitreous membrane undergoing saccadic motion was studied in Repetto *et al.* [62]. In their model for small-amplitude eye rotations, the vitreous was represented by a Newtonian, incompressible fluid in irrotational motion within a spherical cavity separated by an impermeable, pre-stressed elastic membrane. In an experimental study, Repetto *et al.* [63] sought to verify the results of David *et al.* [18] by studying the motion of glycerol, a high viscosity Newtonian fluid, in a spherical cavity subject to sinusoidal motion. The authors then proceeded to determine the experimental motion under more realistic saccadic motion and found that the maximum shear stress at

the wall was not strongly dependent on the amplitude of the saccade. In similar work, Dyson *et al.* [19] studied the wall shear stress due to saccadic motion of the vitreous in normal eyes (hollow sphere filled with viscoelastic fluid) and post vitrectomy eyes (hollow sphere filled with a fluid of known viscosity). The authors found the wall shear stress to be larger in normal eyes than in post-operative eyes.

Repetto *et al.* [64] studied the influence of saccadic motion on PVD using a two dimensional planar model, in which the gel-like vitreous is represented by a viscoelastic solid separated by an elastic membrane from the detached portion, which is given as a Newtonian fluid. Finite element simulations of the rotation of the eye found the largest traction on the retina near the attachments points of the membrane representing the posterior vitreous cortex. This traction was found to be the same order of magnitude as the adhesive force between the retina and RPE, measured from animal subjects in Kita & Marmor [37]. The influences of myopia and scleral buckling on the fluid shear stress due to saccadic motions of the vitreous was studied in Meskauskas *et al.* [49]. The vitreous humor was modeled as a viscoelastic fluid and the shear stress acting on the retina from the vitreous was found analytically for emmetropic and myopic spheroids. The shape changes associated with myopia led to much higher shear stresses in myopic eyes and stress concentrations were found around the indentation in the eye wall representing a scleral buckle.

Chou & Siegel [16] developed a model for exudative retinal detachment which included flows across the retina due to pressure differences and active RPE pump flows, along with retinal adhesion forces and tension in the retina. The retinal detachment was represented by a two dimensional blister lifting off from a flat layer and the bending stiffness of the retina was neglected. The forces included in the model are balanced and the resulting stress is said to result in detachment of infinite extent if it exceeds the adhesive force per unit area of the retina to RPE. Additionally the dependence of the shape of the detached retinal blister on the stretching elasticity of the retina and the adhesive force was found. Exudative retinal detachment was also modeled by Avtar & Srivastava [5], in which the authors consider the fluid flow in the subretinal space. The RPE was treated as a fixed plane and the retina was modeled as a beam under the condition of plane strain.

Numerous studies have focused on finite element modeling of trauma to the ocular

system. Uchio *et al.* [77] and Stitzel *et al.* [75] developed finite element models of the eye to predict globe rupture under impact loading and blunt trauma. Similarly, Rossi *et al.* [67] and Bhardwaj *et al.* [6] used finite element models to study the deformation of the eye globe under blast loading. Liu *et al.* [46] also used a finite element model of the eye to study blunt trauma, but focused on retinal detachment due to that trauma. In the model, the eye is struck by a BB and compresses, which is then followed by a decompression stage. During decompression the negative pressure acting on the retina is of large enough magnitude to exceed the adhesion force between the retina and RPE, measured from animal subjects in Kita & Marmor [37], resulting in the prediction of retinal detachment near and anterior to the equator. The model also predicts when the impact speed of the BB is large enough, the retina will experience sufficient straining in order to cause a break in the retina.

Of the models reviewed thus far regarding the mechanics of the ocular system and retinal detachment, none have adequetely described the fundamental mechanics of detachment propagation. To this end, a mechanics based mathematical model for quasi-static and axisymmetric retinal detachment, incorporating an energy based criterion for detachment propagation, was developed by Bottega *et al.* [12]. The model considered retinas with and without central tears, with contraction of the vitreous and extension of its fibrils, along with a pressure difference across the retina, taken as the stimuli for detachment propagation. The problem was approached as a propagating boundary value problem in the calculus of variations, where the boundaries of the detaching retina are allowed to vary arbitrarily, as well as the deflections of the retina along and transverse to the meridian. The variational formulation yields the self-consistent energy release rate that governs detachment propagation, in addition to the corresponding equilibrium equations, boundary, and matching conditions.

In Bottega *et al.* [12], the meridian displacements of the retina were treated as negligible in order to simplify the coupled equations of equilibrium derived therein into a single differential equation in terms of the radial displacements. When considering deformations of a complete sphere under symmetric loading, the meridian displacements do in fact vanish identically and the obtained solution remains exact. For the present case, however, the uniform symmetry of the sphere is altered by the presence of the detached region and/or

the tear in the retina. As a result, inclusion of the meridian displacements is necessary in order to accurately predict the behavior of the detaching retina. In Lakawicz *et al.* [42], the meridian displacements were retained and exact analytical solutions to the model were presented. Inclusion of the meridian displacements resulted in substantially larger transverse displacements of the retina, while the critical stress for detachment propagation was substantially decreased.

The solutions found in Lakawicz *et al.* [42] were later employed in Ge *et al.* [27] and [26] to study the influence of an equatorial cerclage, and the effects of its material properties, on the deformation of the outer eye and the corresponding influence on the closure of posterior retinal detachment, respectively. The results of Ge *et al.* [27] and [26] improve upon the previous studies in the literature on the effects of an equatorial cerclage by including the effects of bending of the retina which occur in the vicinity of the detached portion of the retina. Pavlou [58] approached the propagation of the vitreo-retinal interface during PVD as caused by saccadic motion of the eye in a manner similar to the model of retinal detachment found in Bottega *et al.* [12]. A two dimensional viscoelastic boundary value problem was formulated in the calculus of variations in order to obtain a detachment criterion for the vitreous during a saccade. The results of that study indicate that if a saccade is large enough to cause the propagation of PVD, then the vitreous will detach until it reaches a point of abnormal vitreo-retinal adhesion.

In Lakawicz *et al.* [43], a mechanics based mathematical model of retinal detachment due to the geometric changes of the eye associated with the evolution of myopia was developed. The model included deformation of the retina due to biological growth of the retina, as well as elastic deformation imposed on the retina by the myopic change in shape of the much stiffer choroid and sclera. From analysis of the *energy release rate*, it was seen that at severe levels of myopia, even in the absence of stress acting on the retina, a sufficient energy release for detachment propagation was achieved. Correspondingly, the critical stress for detachment propagation was found to be lower for the myopic retina when compared to that of the emmetropic retina. The results support the clinical finding of an increased prevalence of retinal detachment in myopic eyes and provide insight into the potential causation for the increased prevalence.

1.3   Outline of the Dissertation

This dissertation presents a study of the application of mechanics based mathematical modeling to age-related and myopia-induced retinal detachments. The dissertation is presented in five chapters. Chapter 2 reviews the theory of the bending of shells that is employed in the later Chapters and establishes a growth law for detachment propagation in layered shells. In Chapter 3, the solution found in Lakawicz *et al.* [42] for the model of retinal detachment propagation in emmetropic eyes is presented and results are discussed in further detail. In Chapter 4, the mechanics based mathematical model for retinal detachment propagation in myopic eyes developed in Lakawicz *et al.* [43] is presented. Finally, Chapter 5 offers a thorough discussion of the results found in this study, followed by a review of potential issues to explore in future work.

Chapter 2

A Growth Law for Detachment Propagation in Layered Shells

In studying the propagation of retinal detachment, the retina is modeled as a thin elastic shell delaminating from the much stiffer choroid and sclera. As such, the model is that of the inner elastic layer of a layered composite shell detaching from a rigid outer layer. Before proceeding to the analysis of retinal detachment propagation, the kinematic and constitutive relations associated with the first-order linear theory of thin, elastic shells is presented. The potential energy functional for a generic shell of revolution is formulated and the theorem of stationary potential energy is applied, where the detachment boundary of the detaching inner layer of the composite shell is allowed to vary arbitrarily. This leads to the governing differential equations and boundary conditions, as well as the transversality condition that governs the location of the curvilinear detachment boundary of the evolving structure. The transversality condition yields the general form of the multi-directional growth law for a layered shell structure, analogous to the growth law for layered plates derived by Bottega [7].

The general theory of thin elastic shells found its initial development in the work of A.E.H. Love [47] in the late 19th century. Love applied the Kirchhoff assumptions associated with plate theory, along with assumptions on the thinness of the shell, in his first-order approximation shell theory. Despite its success, Love's theory suffered from inconsistencies in its treatment of small terms. As summarized in Naghdi [56], Love's theorem 1) was not invariant under coordinate transformation, 2) strains did not vanish for rigid body displacements, 3) did not satisfy the balance of moments about the transverse axis, and 4) did not satisfy the theorem of reciprocity. Many attempts were made to refine Love's theory, noteworthy of which is Reissner [60], which removed many of the inconsistencies of

Love's theory but still suffered from the fact that its strains did not vanish under rigid-body rotation for all possible shell geometries. The Koiter-Sanders theory for thin shells (Koiter [41], Sanders [68]) is widely credited with total elimination of the inconsistencies in Love's theory.

The derivation of the linear theory of thin, elastic shells presented herein follows the derivation found in Møllmann [53] of the Koiter-Sanders theory for thin shells. The linear theory considers infinitesimal displacements and rotations of the shell. In addition, the effects of transverse shear stresses and the deformation through the thickness of the shell are neglected. In the derivation, the work of Ventsel & Krauthammer [78] and Soedel [74] served as additional sources of reference.

2.1 The Geometry of the Middle Surface

A thin shell is a curvilinear structure whose thickness, h, is small when compared to its radius of curvature, R. The middle surface lies equal distances from the two bounding curved surfaces of the shell. The form of the middle surface and the thickness of the shell completely define the geometry of the shell structure. The position vector, r, of any point along the middle surface measured from the origin is determined by the orthogonal curvilinear coordinates θ_1 and θ_2, as shown in Figure 2.1.
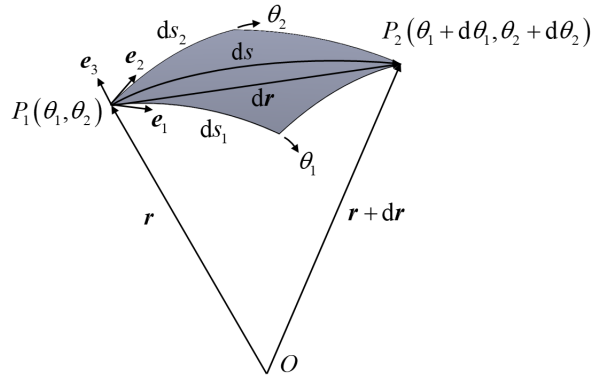
Figure 2.1: A differential element of the middle surface of a shell.

The derivatives of the position vector with respect to the curvilinear coordinates give the tangent vectors to the curvilinear coordinate curves. It follows that these derivatives

represent the curvilinear base vectors, $\boldsymbol{a}_1$ and $\boldsymbol{a}_2$, for the middle surface, defined as

$$\boldsymbol{a}_1 = \frac{\partial \boldsymbol{r}}{\partial \theta_1} \quad \text{and} \quad \boldsymbol{a}_2 = \frac{\partial \boldsymbol{r}}{\partial \theta_2} \tag{2.1}$$

The third basis vector for the middle surface, $\boldsymbol{a}_3 = \boldsymbol{a}_1 \times \boldsymbol{a}_2$, is given by the normal vector to the surface directed away from the origin.

On the differential surface element shown in Figure 2.1, the infinitesimal linear change in distance between points P_1 and P_2 follows as

$$\mathrm{d}\boldsymbol{r} = \frac{\partial \boldsymbol{r}}{\partial \theta_1} \mathrm{d}\theta_1 + \frac{\partial \boldsymbol{r}}{\partial \theta_2} \mathrm{d}\theta_2 = \sum_{i=1}^{2} \frac{\partial \boldsymbol{r}}{\partial \theta_i} \mathrm{d}\theta_i = \sum_{i=1}^{2} \boldsymbol{a}_i \mathrm{d}\theta_i \tag{2.2}$$

In the same figure, the arc length between points P_1 and P_2 is given as $\mathrm{d}s$. In the limit of the infinitesimal surface element, the magnitude of $\mathrm{d}\boldsymbol{r}$ is $\mathrm{d}s$, which is given as

$$\mathrm{d}s^2 = \mathrm{d}\boldsymbol{r} \cdot \mathrm{d}\boldsymbol{r} = \frac{\partial \boldsymbol{r}}{\partial \theta_1} \cdot \frac{\partial \boldsymbol{r}}{\partial \theta_1} (\mathrm{d}\theta_1)^2 + 2\frac{\partial \boldsymbol{r}}{\partial \theta_1} \cdot \frac{\partial \boldsymbol{r}}{\partial \theta_2} (\mathrm{d}\theta_1 \mathrm{d}\theta_2) + \frac{\partial \boldsymbol{r}}{\partial \theta_2} \cdot \frac{\partial \boldsymbol{r}}{\partial \theta_2} (\mathrm{d}\theta_2)^2$$
$$\mathrm{d}s^2 = \left| \frac{\partial \boldsymbol{r}}{\partial \theta_1} \right|^2 (\mathrm{d}\theta_1)^2 + \left| \frac{\partial \boldsymbol{r}}{\partial \theta_2} \right|^2 (\mathrm{d}\theta_2)^2 \tag{2.3}$$

From Eq. (2.3), it is defined that

$$A_1 = |\boldsymbol{a}_1| = \left| \frac{\partial \boldsymbol{r}}{\partial \theta_1} \right| = \sqrt{\frac{\partial \boldsymbol{r}}{\partial \theta_1} \cdot \frac{\partial \boldsymbol{r}}{\partial \theta_1}} \tag{2.4a}$$

$$A_2 = |\boldsymbol{a}_2| = \left| \frac{\partial \boldsymbol{r}}{\partial \theta_2} \right| = \sqrt{\frac{\partial \boldsymbol{r}}{\partial \theta_2} \cdot \frac{\partial \boldsymbol{r}}{\partial \theta_2}} \tag{2.4b}$$

where A_1 and A_2 are referred to as the Lamé parameters of the surface. In comparing Eqs. (2.1) and (2.4) it is seen that physically, the Lamé parameters represent the length of the curvilinear base vectors $\boldsymbol{a}_1$ and $\boldsymbol{a}_2$, respectively.

Substitution of Eq. (2.4) into Eq. (2.3) results in

$$\mathrm{d}s^2 = \mathrm{d}s_1^2 + \mathrm{d}s_2^2 = A_1^2 (\mathrm{d}\theta_1)^2 + A_2^2 (\mathrm{d}\theta_2)^2 \tag{2.5}$$

which is known as the *first fundamental form* of the surface. The coefficients of the first fundamental form are identified in index notation as

$$a_{ij} = \boldsymbol{a}_i \cdot \boldsymbol{a}_j = a_{ji} \tag{2.6}$$

where in this derivation, i, j represent the indices 1, 2 and there is no summation taken on the indices unless a summation symbol is explicitly shown. Hence, from Eq. (2.1), and the

mutual orthogonality of the base vectors, the coefficients in Eq. (2.6) are given explicitly as

$$a_{11} = A_1^2, \qquad a_{12} = a_{21} = 0, \qquad a_{22} = A_2^2 \tag{2.7}$$

The first fundamental form defines the intrinsic geometry of the surface which includes the distance along an arc between two points on the surface and the area of the surface. Hence, changes in the first fundamental form will lead to the strain measures governing the change of length of the surface.

The normal curvature of the differential shell element is defined as

$$K\boldsymbol{a}_3 = -\frac{\mathrm{d}\boldsymbol{t}}{\mathrm{d}s} \tag{2.8}$$

where K is the normal curvature, $\boldsymbol{a}_3$ is the base vector normal to the curve, and $\boldsymbol{t}$ is the unit vector tangent to the curve, all as shown in Figure 2.2. Equation (2.8) can then be rewritten as follows

$$
\begin{aligned}
K &= -\frac{\mathrm{d}\boldsymbol{t}}{\mathrm{d}s} \cdot \boldsymbol{a}_3 \\
K &= -\frac{\mathrm{d}}{\mathrm{d}s}\left(\boldsymbol{t} \cdot \boldsymbol{a}_3\right) + \frac{\mathrm{d}\boldsymbol{a}_3}{\mathrm{d}s} \cdot \boldsymbol{t} \\
K &= \frac{\mathrm{d}\boldsymbol{a}_3}{\mathrm{d}s} \cdot \boldsymbol{t}
\end{aligned}
\tag{2.9}
$$

since $\boldsymbol{a}_3$ and $\boldsymbol{t}$ are mutually orthogonal.
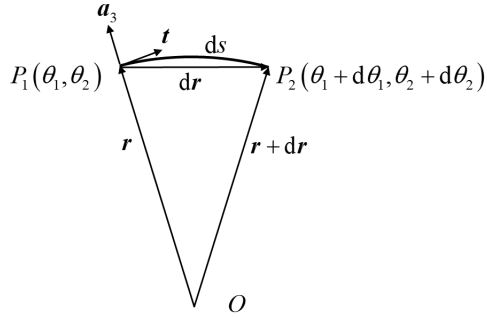
Figure 2.2: The normal curvature of a differential element of the middle surface.

From Figure 2.2, the unit tangent vector is given by

$$\boldsymbol{t} = \frac{\mathrm{d}\boldsymbol{r}}{\mathrm{d}s} \tag{2.10}$$

In addition, it follows that

$$\frac{\mathrm{d}\boldsymbol{a}_3}{\mathrm{d}s} = \frac{\partial \boldsymbol{a}_3}{\partial \theta_1}\frac{\mathrm{d}\theta_1}{\mathrm{d}s} + \frac{\partial \boldsymbol{a}_3}{\partial \theta_2}\frac{\mathrm{d}\theta_2}{\mathrm{d}s} = \sum_{i=1}^{2} \frac{\partial \boldsymbol{a}_3}{\partial \theta_i}\frac{\mathrm{d}\theta_i}{\mathrm{d}s} \tag{2.11}$$

Substitution of Eqs. (2.10) and (2.11), along with Eq. (2.2), into the final result of Eq. (2.9), yields

$$K = \frac{\sum_{i=1}^{2} \sum_{j=1}^{2} \frac{\partial \boldsymbol{a}_3}{\partial \theta_i} \cdot \boldsymbol{a}_j \mathrm{d}\theta_i \mathrm{d}\theta_j}{\mathrm{d}s^2} \tag{2.12}$$

The relation in the numerator of Eq. (2.12) is identified as the *second fundamental form* of the surface. The coefficients of the second fundamental form are given in index notation as

$$b_{ij} = \frac{\partial \boldsymbol{a}_3}{\partial \theta_i} \cdot \boldsymbol{a}_j = -\boldsymbol{a}_3 \cdot \frac{\partial \boldsymbol{a}_j}{\partial \theta_i} = -\boldsymbol{a}_3 \cdot \frac{\partial \boldsymbol{a}_i}{\partial \theta_j} = b_{ji} \tag{2.13}$$

where the mutual orthogonality of the basis vectors has again been employed.

Equation (2.12) can be rewritten through substitution of Eqs. (2.6) and (2.13) as

$$K = \frac{b_{11}\left(\mathrm{d}\theta_1\right)^2 + 2b_{12}\mathrm{d}\theta_1\mathrm{d}\theta_2 + b_{22}\left(\mathrm{d}\theta_2\right)^2}{a_{11}\left(\mathrm{d}\theta_1\right)^2 + 2a_{12}\mathrm{d}\theta_1\mathrm{d}\theta_2 + a_{22}\left(\mathrm{d}\theta_2\right)^2} \tag{2.14}$$

Hence, the coefficients of the second fundamental form characterize the normal curvature of the θ_1 and θ_2 coordinate curves, while the normal curvature of the surface is given by the ratio of the first and second fundamental forms. Since the coordinate curves are mutually orthogonal, the coefficient b_{12}, which characterizes the twisting of the coordinate curves, must vanish as did the coefficient a_{12} in Eq. (2.6).

It remains to define the association between the unit vectors $(\boldsymbol{e}_1, \boldsymbol{e}_2, \boldsymbol{e}_3)$ shown in Figure 2.1, and the curvilinear base vectors $(\boldsymbol{a}_1, \boldsymbol{a}_2, \boldsymbol{a}_3)$. We take the unit vectors to be in the direction of the base vectors. Hence,

$$\boldsymbol{e}_1 = \frac{\boldsymbol{a}_1}{|\boldsymbol{a}_1|} = \frac{\boldsymbol{a}_1}{A_1} \quad \text{and} \quad \boldsymbol{e}_2 = \frac{\boldsymbol{a}_2}{|\boldsymbol{a}_2|} = \frac{\boldsymbol{a}_2}{A_2} \tag{2.15}$$

with

$$\boldsymbol{e}_3 = \boldsymbol{e}_1 \times \boldsymbol{e}_2 = \frac{1}{A_1 A_2}\left(\boldsymbol{a}_1 \times \boldsymbol{a}_2\right) = \boldsymbol{a}_3 \tag{2.16}$$

The derivatives of the unit vectors with respect to the curvilinear coordinates θ_1 and θ_2 are needed in the derivation. Consider Eq. $(2.9)_3$, with the normal curvature replaced by $K = 1/R$ where R is the radius of curvature. If the curve shown in Figure 2.2 is taken to be the θ_1 coordinate curve, Eq. (2.9) becomes

$$\frac{1}{R_1} = \frac{\mathrm{d}\boldsymbol{e}_3}{\mathrm{d}s_1} \cdot \boldsymbol{e}_1 = \frac{1}{A_1}\frac{\partial \boldsymbol{e}_3}{\partial \theta_1} \cdot \boldsymbol{e}_1 \tag{2.17}$$

where R_1 is the principal radius of curvature in the θ_1 direction and $\mathrm{d}s_1 = A_1\mathrm{d}\theta_1$, as given in Eq. (2.3). Rearranging Eq. (2.17) yields

$$\frac{\partial \boldsymbol{e}_3}{\partial \theta_1} = \frac{A_1}{R_1}\boldsymbol{e}_1 \tag{2.18}$$

Similarly, if Figure 2.2 is taken to represent the θ_2 coordinate curve, it is found that

$$\frac{\partial \boldsymbol{e}_3}{\partial \theta_2} = \frac{A_2}{R_2}\boldsymbol{e}_2 \tag{2.19}$$

where R_2 is the principal radius of curvature in the θ_2 direction. Substitution of Eqs. (2.18) or (2.19) into Eq. (2.13) provides proof that the coefficient b_{12} does indeed vanish.

The derivatives of the unit vectors $\boldsymbol{e}_1$ and $\boldsymbol{e}_2$ follow. First, the identities $\boldsymbol{e}_1 \cdot \boldsymbol{e}_1 = 1$ and $\boldsymbol{e}_1 \cdot \boldsymbol{e}_3 = 0$ are differentiated with respect to the coordinate θ_2. Hence,

$$\frac{\partial}{\partial \theta_2}(\boldsymbol{e}_1 \cdot \boldsymbol{e}_1) = \frac{\partial \boldsymbol{e}_1}{\partial \theta_2}\cdot \boldsymbol{e}_1 = 0 \tag{2.20}$$

$$\frac{\partial}{\partial \theta_2}(\boldsymbol{e}_1 \cdot \boldsymbol{e}_3) = \frac{\partial \boldsymbol{e}_1}{\partial \theta_2}\cdot \boldsymbol{e}_3 + \boldsymbol{e}_1 \cdot \frac{\partial \boldsymbol{e}_3}{\partial \theta_2} = \frac{\partial \boldsymbol{e}_1}{\partial \theta_2}\cdot \boldsymbol{e}_3 = 0 \tag{2.21}$$

Similarly, the identities $\boldsymbol{e}_2 \cdot \boldsymbol{e}_2 = 1$ and $\boldsymbol{e}_2 \cdot \boldsymbol{e}_3 = 0$ are differentiated with respect to the coordinate θ_1. Hence,

$$\frac{\partial}{\partial \theta_1}(\boldsymbol{e}_2 \cdot \boldsymbol{e}_2) = \frac{\partial \boldsymbol{e}_2}{\partial \theta_1}\cdot \boldsymbol{e}_2 = 0 \tag{2.22}$$

$$\frac{\partial}{\partial \theta_1}(\boldsymbol{e}_2 \cdot \boldsymbol{e}_3) = \frac{\partial \boldsymbol{e}_2}{\partial \theta_1}\cdot \boldsymbol{e}_3 + \boldsymbol{e}_2 \cdot \frac{\partial \boldsymbol{e}_3}{\partial \theta_1} = \frac{\partial \boldsymbol{e}_2}{\partial \theta_1}\cdot \boldsymbol{e}_3 = 0 \tag{2.23}$$

With these identities, the derivatives of $\boldsymbol{e}_1$ and $\boldsymbol{e}_2$ with respect to their tangent directions are obtained as follows

$$\frac{\partial \boldsymbol{e}_1}{\partial \theta_2}\cdot \boldsymbol{e}_2 = \left(\frac{1}{A_1}\frac{\partial \boldsymbol{a}_1}{\partial \theta_2} + \frac{1}{A_1^2}\frac{\partial A_1}{\partial \theta_2}\boldsymbol{a}_1\right)\cdot \boldsymbol{e}_2 = \frac{1}{A_1}\frac{\partial \boldsymbol{a}_1}{\partial \theta_2}\cdot \boldsymbol{e}_2 \tag{2.24}$$

From Eq. (2.1), it is seen that $\frac{\partial \boldsymbol{a}_1}{\partial \theta_2} = \frac{\partial \boldsymbol{a}_2}{\partial \theta_1}$, which when substituted into Eq. (2.24) yields

$$\frac{\partial \boldsymbol{e}_1}{\partial \theta_2}\cdot \boldsymbol{e}_2 = \frac{1}{A_1}\frac{\partial \boldsymbol{a}_2}{\partial \theta_1}\cdot \boldsymbol{e}_2 = \frac{1}{A_1}\left(\frac{\partial A_2}{\partial \theta_1}\boldsymbol{e}_2 + A_2\frac{\partial \boldsymbol{e}_2}{\partial \theta_1}\right)\cdot \boldsymbol{e}_2 \tag{2.25}$$

with Eq. (2.22) the final result is

$$\frac{\partial \boldsymbol{e}_1}{\partial \theta_2}\cdot \boldsymbol{e}_2 = \frac{1}{A_1}\frac{\partial A_2}{\partial \theta_1} \tag{2.26}$$

Combining Eqs. (2.20), (2.21), and (2.26) shows that $\frac{\partial \boldsymbol{e}_1}{\partial \theta_2}$ only has a component in the $\boldsymbol{e}_2$ and hence, that

$$\frac{\partial \boldsymbol{e}_1}{\partial \theta_2} = \frac{1}{A_1}\frac{\partial A_2}{\partial \theta_1}\boldsymbol{e}_2 \tag{2.27}$$

Performing the operations indicated in Eqs. (2.24)-(2.27) with the indices 1 and 2 reversed along with Eqs. (2.22) and (2.23) yields

$$\frac{\partial \boldsymbol{e}_2}{\partial \theta_1} = \frac{1}{A_2} \frac{\partial A_1}{\partial \theta_2} \boldsymbol{e}_1 \tag{2.28}$$

To obtain the remaining derivatives, the identities $\boldsymbol{e}_1 \cdot \boldsymbol{e}_1 = 1$, $\boldsymbol{e}_1 \cdot \boldsymbol{e}_2 = 0$, and $\boldsymbol{e}_1 \cdot \boldsymbol{e}_3 = 0$ are differentiated with respect to the coordinate θ_1. Hence,

$$\frac{\partial}{\partial \theta_1} (\boldsymbol{e}_1 \cdot \boldsymbol{e}_1) = \frac{\partial \boldsymbol{e}_1}{\partial \theta_1} \cdot \boldsymbol{e}_1 = 0 \tag{2.29}$$

$$\frac{\partial}{\partial \theta_1} (\boldsymbol{e}_1 \cdot \boldsymbol{e}_2) = \frac{\partial \boldsymbol{e}_1}{\partial \theta_1} \cdot \boldsymbol{e}_2 + \boldsymbol{e}_1 \cdot \frac{\partial \boldsymbol{e}_2}{\partial \theta_1} = \frac{\partial \boldsymbol{e}_1}{\partial \theta_1} \cdot \boldsymbol{e}_2 + \frac{1}{A_2} \frac{\partial A_1}{\partial \theta_2} = 0 \tag{2.30}$$

$$\frac{\partial}{\partial \theta_1} (\boldsymbol{e}_1 \cdot \boldsymbol{e}_3) = \frac{\partial \boldsymbol{e}_1}{\partial \theta_1} \cdot \boldsymbol{e}_3 + \boldsymbol{e}_1 \cdot \frac{\partial \boldsymbol{e}_3}{\partial \theta_1} = \frac{\partial \boldsymbol{e}_1}{\partial \theta_1} \cdot \boldsymbol{e}_3 + \frac{A_1}{R_1} = 0 \tag{2.31}$$

where Eq. (2.30) employs the relation of Eq. (2.18) and Eq. (2.31) employs the relation of Eq. (2.28). The components of $\frac{\partial \boldsymbol{e}_1}{\partial \theta_1}$ are taken from Eqs. (2.29)-(2.31), which results in

$$\frac{\partial \boldsymbol{e}_1}{\partial \theta_1} = -\frac{1}{A_2} \frac{\partial A_1}{\partial \theta_2} \boldsymbol{e}_2 - \frac{A_1}{R_1} \boldsymbol{e}_3 \tag{2.32}$$

Similar operations with the indices reversed yields

$$\frac{\partial \boldsymbol{e}_2}{\partial \theta_2} = -\frac{1}{A_1} \frac{\partial A_2}{\partial \theta_1} \boldsymbol{e}_1 - \frac{A_2}{R_2} \boldsymbol{e}_3 \tag{2.33}$$

Compiling the results of Eqs. (2.18)-(2.33) gives the derivatives of the unit vectors as

$$\frac{\partial \boldsymbol{e}_1}{\partial \theta_1} = -\frac{1}{A_2} \frac{\partial A_1}{\partial \theta_2} \boldsymbol{e}_2 - \frac{A_1}{R_1} \boldsymbol{e}_3 \tag{2.34a}$$

$$\frac{\partial \boldsymbol{e}_1}{\partial \theta_2} = \frac{1}{A_1} \frac{\partial A_2}{\partial \theta_1} \boldsymbol{e}_2 \tag{2.34b}$$

$$\frac{\partial \boldsymbol{e}_2}{\partial \theta_1} = \frac{1}{A_2} \frac{\partial A_1}{\partial \theta_2} \boldsymbol{e}_1 \tag{2.34c}$$

$$\frac{\partial \boldsymbol{e}_2}{\partial \theta_2} = -\frac{1}{A_1} \frac{\partial A_2}{\partial \theta_1} \boldsymbol{e}_1 - \frac{A_2}{R_2} \boldsymbol{e}_3 \tag{2.34d}$$

$$\frac{\partial \boldsymbol{e}_3}{\partial \theta_1} = \frac{A_1}{R_1} \boldsymbol{e}_1 \tag{2.34e}$$

$$\frac{\partial \boldsymbol{e}_3}{\partial \theta_2} = \frac{A_2}{R_2} \boldsymbol{e}_2 \tag{2.34f}$$

The geometry of the middle surface is now fully defined. Next, the derivation of the associated kinematic relations is presented.

2.2 Kinematic Relations

The displacement of a point on the middle surface which deforms from a reference position, $\boldsymbol{r}$, to the current position, $\boldsymbol{r}^*$ is given by the displacement vector, $\boldsymbol{u}$. The relation between the reference position and the current position of that point follows as

$$\boldsymbol{r}^*\left(\theta_1, \theta_2\right) = \boldsymbol{r}\left(\theta_1, \theta_2\right) + \boldsymbol{u}\left(\theta_1, \theta_2\right) \tag{2.35}$$

where the components of the displacement vector are defined as

$$\boldsymbol{u}\left(\theta_1, \theta_2\right) = u_1\left(\theta_1, \theta_2\right)\boldsymbol{e}_1 + u_2\left(\theta_1, \theta_2\right)\boldsymbol{e}_2 - w\left(\theta_1, \theta_2\right)\boldsymbol{e}_3 \tag{2.36}$$

In this form, the displacement normal to the middle surface, w, is positive when displacing inward from the reference surface.

2.2.1 Strain

An element of the middle surface with length $\mathrm{d}s$ in the reference configuration and length $\mathrm{d}s^*$ in the deformed configuration is considered. As discussed following Eq. (2.7), the strain is related to the first fundamental form, which is given in Eq. (2.5). The strain is a measure of the relative elongation of a material line element of the middle surface and thus is taken to be given by

$$\varepsilon = \frac{1}{2}\frac{\left(\mathrm{d}s^*\right)^2 - \left(\mathrm{d}s\right)^2}{\left(\mathrm{d}s\right)^2} \tag{2.37}$$

and hence, in tensor notation, ε_{ij}, as

$$\varepsilon_{ij} = \frac{1}{2}\frac{a_{ij}^* - a_{ij}}{A_i A_j} = \frac{1}{2}\frac{\left(a_{ij} + \Delta a_{ij}\right) - a_{ij}}{A_i A_j} = \frac{1}{2}\frac{\Delta a_{ij}}{A_i A_j} \tag{2.38}$$

where Δ is an infinitesimal increment in the given variable. In this form, the change in the coefficients of the first fundamental form of the surface will yield a symmetric strain tensor. If the term $a_{ij}^* - a_{ij}$ in the numerator of Eq. (2.37) vanishes, then the length of the surface element remains unchanged and there is no extension or compression of the middle surface. Through substitution of Eqs. (2.1), (2.6), and (2.35), the numerator of Eq. (2.38) is rewritten as

$$\begin{aligned} \Delta a_{ij} = a_{ij}^* - a_{ij} &= \frac{\partial\left(\boldsymbol{r} + \boldsymbol{u}\right)}{\partial\theta_i} \cdot \frac{\partial\left(\boldsymbol{r} + \boldsymbol{u}\right)}{\partial\theta_j} - \frac{\partial\boldsymbol{r}}{\partial\theta_i} \cdot \frac{\partial\boldsymbol{r}}{\partial\theta_j} \\ \Delta a_{ij} &= \frac{\partial\boldsymbol{r}}{\partial\theta_i} \cdot \frac{\partial\boldsymbol{u}}{\partial\theta_j} + \frac{\partial\boldsymbol{u}}{\partial\theta_i} \cdot \frac{\partial\boldsymbol{r}}{\partial\theta_j} + \frac{\partial\boldsymbol{u}}{\partial\theta_i} \cdot \frac{\partial\boldsymbol{u}}{\partial\theta_j} \end{aligned} \tag{2.39}$$

Substitution of Eq. (2.39) into Eq. (2.38) yields the nonlinear strain tensor as

$$\varepsilon_{ij} = \frac{1}{2A_iA_j}\left(\frac{\partial \boldsymbol{r}}{\partial \theta_i}\cdot\frac{\partial \boldsymbol{u}}{\partial \theta_j} + \frac{\partial \boldsymbol{u}}{\partial \theta_i}\cdot\frac{\partial \boldsymbol{r}}{\partial \theta_j} + \frac{\partial \boldsymbol{u}}{\partial \theta_i}\cdot\frac{\partial \boldsymbol{u}}{\partial \theta_j}\right)$$
$$\varepsilon_{ij} = \frac{1}{2A_iA_j}\left(\frac{\partial \boldsymbol{u}}{\partial \theta_j}\cdot\boldsymbol{a}_i + \frac{\partial \boldsymbol{u}}{\partial \theta_i}\cdot\boldsymbol{a}_j + \frac{\partial \boldsymbol{u}}{\partial \theta_i}\cdot\frac{\partial \boldsymbol{u}}{\partial \theta_j}\right)$$

(2.40)

In linearizing the strain tensor, the last term in the second line of Eq. (2.40) is neglected as it is nonlinear. This yields

$$\varepsilon_{ij} = \frac{1}{2A_iA_j}\left(\frac{\partial \boldsymbol{u}}{\partial \theta_j}\cdot\boldsymbol{a}_i + \frac{\partial \boldsymbol{u}}{\partial \theta_i}\cdot\boldsymbol{a}_j\right) \tag{2.41}$$

The components of the linear strain tensor of the middle surface are found in terms of the displacement components through substitution of Eqs. (2.1) and (2.36), along with Eqs. (2.18)-(2.34), into Eq. (2.41). Hence,

$$\varepsilon_{11} = \frac{1}{A_1}\frac{\partial u_1}{\partial \theta_1} + \frac{u_2}{A_1A_2}\frac{\partial A_1}{\partial \theta_2} - \frac{w}{R_1} \tag{2.42a}$$

$$\varepsilon_{22} = \frac{1}{A_2}\frac{\partial u_2}{\partial \theta_2} + \frac{u_1}{A_1A_2}\frac{\partial A_2}{\partial \theta_1} - \frac{w}{R_2} \tag{2.42b}$$

$$\varepsilon_{12} = \varepsilon_{21} = \frac{1}{2}\left[\frac{A_2}{A_1}\frac{\partial}{\partial \theta_1}\left(\frac{u_2}{A_2}\right) + \frac{A_1}{A_2}\frac{\partial}{\partial \theta_2}\left(\frac{u_1}{A_1}\right)\right] \tag{2.42c}$$

A geometric representation of the change in length of the base vectors due to the straining of the middle surface is shown in Figure 2.3. From that figure, it is clear the differential
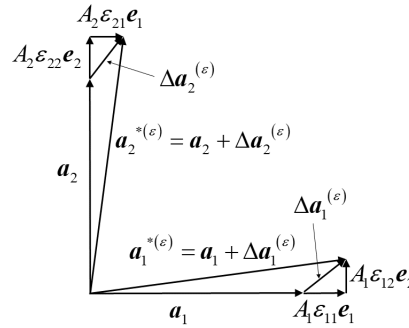
Figure 2.3: Change in length of the curvilinear base vectors due to straining of the middle surface.

change in length of the base vector due to straining, $\Delta\boldsymbol{a}^{(\varepsilon)}$, can be represented as

$$\Delta\boldsymbol{a}_i^{(\varepsilon)} = A_i\sum_{j=1}^{2}\varepsilon_{ij}\boldsymbol{e}_j \tag{2.43}$$

Next, consideration is given to the additional deformation that occurs due to rotation of the middle surface.

2.2.2 Rotation

The total change in the base vectors of the middle surface when deforming from the reference configuration to the current configuration, $\Delta \boldsymbol{a}$, is given as

$$\Delta \boldsymbol{a}_i = \boldsymbol{a}_i^* - \boldsymbol{a}_i = \frac{\partial (\boldsymbol{r} + \boldsymbol{u})}{\partial \theta_i} - \frac{\partial \boldsymbol{r}}{\partial \theta_i} = \frac{\partial \boldsymbol{u}}{\partial \theta_i} \tag{2.44}$$

The increment in the base vectors can also be represented as

$$\Delta \boldsymbol{a}_i = \Delta \boldsymbol{a}_i^{(\varepsilon)} + \Delta \boldsymbol{a}_i^{(\beta)} \tag{2.45}$$

where $\Delta \boldsymbol{a}^{(\beta)}$ is the increment in the base vector due to a rotation, $\boldsymbol{\beta}$. Hence,

$$\Delta \boldsymbol{a}_i^{(\beta)} = \boldsymbol{\beta} \times \boldsymbol{a}_i \tag{2.46}$$

Since there is assumed to be no strain through the thickness of the shell, Eqs. (2.45) and (2.46) yield

$$\Delta \boldsymbol{a}_3 = \boldsymbol{\beta} \times \boldsymbol{a}_3 \tag{2.47}$$

Substitution of Eqs. (2.43), (2.44), and (2.46) into Eq. (2.45) yields

$$\frac{\partial \boldsymbol{u}}{\partial \theta_i} - \boldsymbol{\beta} \times \boldsymbol{a}_i = A_i \sum_{j=1}^{2} \varepsilon_{ij} \boldsymbol{e}_j \tag{2.48}$$

Taking the scalar product of Eq. (2.48) with $\boldsymbol{a}_j$ and $\boldsymbol{a}_3$ results in

$$\left(\frac{\partial \boldsymbol{u}}{\partial \theta_i} - \boldsymbol{\beta} \times \boldsymbol{a}_i \right) \cdot \boldsymbol{a}_j = A_i A_j \varepsilon_{ij} \tag{2.49}$$

and

$$\left(\frac{\partial \boldsymbol{u}}{\partial \theta_i} - \boldsymbol{\beta} \times \boldsymbol{a}_i \right) \cdot \boldsymbol{a}_3 = 0 \tag{2.50}$$

respectively.

With some manipulation, Eq. (2.50) is rewritten as

$$\boldsymbol{\beta} \cdot (\boldsymbol{e}_3 \times \boldsymbol{a}_i) = -\frac{\partial \boldsymbol{u}}{\partial \theta_i} \cdot \boldsymbol{e}_3 \tag{2.51}$$
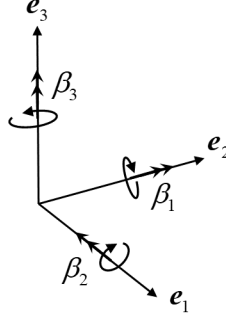
Figure 2.4: Orientation of the components of the rotation vector.

The rotation vector is defined as follows

$$\boldsymbol{\beta}\left(\theta_1,\theta_2\right) = -\beta_2\left(\theta_1,\theta_2\right)\boldsymbol{e}_1 + \beta_1\left(\theta_1,\theta_2\right)\boldsymbol{e}_2 + \beta_3\left(\theta_1,\theta_2\right)\boldsymbol{e}_3 \tag{2.52}$$

which is visually depicted in Figure 2.4. When defined in this sense, β_1 is the normal rotation about interior surfaces of the shell with unit normal in the θ_1 direction and β_2 is the normal rotation about interior surfaces of the shell with unit normal in the θ_2 direction.

Substitution of Eqs. (2.36) and (2.52) into Eq. (2.51), followed by expansion on the indices $i = 1$ and $i = 2$ yields the in-plane components of the rotation vector for the middle surface. Hence,

$$\beta_1 = \frac{1}{A_1}\left(u_1\frac{A_1}{R_1} + \frac{\partial w}{\partial \theta_1}\right) \tag{2.53a}$$

$$\beta_2 = \frac{1}{A_2}\left(u_2\frac{A_2}{R_2} + \frac{\partial w}{\partial \theta_2}\right) \tag{2.53b}$$

It remains to determine the component of the rotation vector about the $\boldsymbol{e}_3$ axis. Here, expansion of Eq. (2.49) first on $i = 1$, $j = 2$ and then on $i = 2$, $j = 1$ yields

$$\left(\frac{\partial \boldsymbol{u}}{\partial \theta_1} - \boldsymbol{\beta} \times \boldsymbol{a}_1\right) \cdot \boldsymbol{a}_2 = A_1 A_2 \varepsilon_{12} \tag{2.54}$$

and

$$\left(\frac{\partial \boldsymbol{u}}{\partial \theta_2} - \boldsymbol{\beta} \times \boldsymbol{a}_2\right) \cdot \boldsymbol{a}_1 = A_2 A_1 \varepsilon_{21} \tag{2.55}$$

respectively. Since $\varepsilon_{12} = \varepsilon_{21}$, Eqs. (2.54) and (2.55) are combined as follows

$$\left(\frac{\partial \boldsymbol{u}}{\partial \theta_1} - \boldsymbol{\beta} \times \boldsymbol{a}_1\right) \cdot \boldsymbol{a}_2 = \left(\frac{\partial \boldsymbol{u}}{\partial \theta_2} - \boldsymbol{\beta} \times \boldsymbol{a}_2\right) \cdot \boldsymbol{a}_1 \tag{2.56}$$

Carrying through the dot products given in Eq. (2.56) results in

$$\frac{\partial \boldsymbol{u}}{\partial \theta_1} \cdot \boldsymbol{a}_2 - \frac{\partial \boldsymbol{u}}{\partial \theta_2} \cdot \boldsymbol{a}_1 = 2\boldsymbol{\beta} \cdot (\boldsymbol{a}_1 \times \boldsymbol{a}_2) = 2A_1 A_2 (\boldsymbol{\beta} \cdot \boldsymbol{e}_3) \tag{2.57}$$

Substitution of Eqs. (2.36) and (2.52) into Eq. (2.51) yields the final form for β_3 as

$$\beta_3 = \frac{1}{2A_1 A_2} \left[\frac{\partial (A_2 u_2)}{\partial \theta_1} - \frac{\partial (A_1 u_1)}{\partial \theta_2} \right] \tag{2.58}$$

Hence, the rotation vector given in Eq. (2.52) has components as defined in Eqs. (2.53) and (2.58).

2.2.3   Bending

In Section 2.2.1, the strain of the middle surface was determined by finding the change in length of an element of the surface that results from the change in the first fundamental form of the surface. Similarly, the bending effects of the middle surface are determined by the change in curvature of the middle surface through the change in the second fundamental form of the surface. The coefficients of the second fundamental form were given in Eq. (2.13), and their changes when going from the reference configuration to the current configuration follow as

$$\begin{aligned}
\Delta b_{ij} = b_{ij}^* - b_{ij} &= \frac{\partial \boldsymbol{a}_3^*}{\partial \theta_i} \cdot \frac{\partial (\boldsymbol{r} + \boldsymbol{u})}{\partial \theta_j} - \frac{\partial \boldsymbol{a}_3}{\partial \theta_i} \cdot \frac{\partial \boldsymbol{r}}{\partial \theta_j} \\
\Delta b_{ij} &= \frac{\partial \boldsymbol{a}_3^*}{\partial \theta_i} \cdot \boldsymbol{a}_j + \frac{\partial \boldsymbol{a}_3^*}{\partial \theta_i} \cdot \frac{\partial \boldsymbol{u}}{\partial \theta_j} - \frac{\partial \boldsymbol{a}_3}{\partial \theta_i} \cdot \boldsymbol{a}_j \\
\Delta b_{ij} &= \frac{\partial}{\partial \theta_i} (\Delta \boldsymbol{a}_3) \cdot \boldsymbol{a}_j + \frac{\partial}{\partial \theta_i} (\boldsymbol{a}_3 + \Delta \boldsymbol{a}_3) \cdot \Delta \boldsymbol{a}_j
\end{aligned} \tag{2.59}$$

where Eq. (2.44) is used to obtain the last line of Eq. (2.59). When the last term of the last line in Eq. (2.59) is expanded, the term $\frac{\partial}{\partial \theta_i} (\Delta \boldsymbol{a}_3) \cdot \Delta \boldsymbol{a}_j$ is obtained, which is small when compared to the first term of the same line and must be neglected. Hence, the change in the second fundamental form follows as

$$\Delta b_{ij} = b_{ij}^* - b_{ij} = \frac{\partial}{\partial \theta_i} (\Delta \boldsymbol{a}_3) \cdot \boldsymbol{a}_j + \frac{\partial}{\partial \theta_i} (\boldsymbol{a}_3) \cdot \Delta \boldsymbol{a}_j \tag{2.60}$$

Substitution of Eqs. (2.44) and (2.47) into Eq. (2.60) results in

$$\Delta b_{ij} = \frac{\partial}{\partial \theta_i} (\boldsymbol{\beta} \times \boldsymbol{a}_3) \cdot \boldsymbol{a}_j + \frac{\partial}{\partial \theta_i} (\boldsymbol{a}_3) \cdot \frac{\partial \boldsymbol{u}}{\partial \theta_j} \tag{2.61}$$

From Eqs. (2.18) and (2.19), along with Eqs. (2.15) and (2.16), it is seen that

$$\frac{\partial \boldsymbol{a}_3}{\partial \theta_i} = \frac{1}{R_i} \boldsymbol{a}_i \tag{2.62}$$

which, when substituted into Eq. (2.61) yields

$$\Delta b_{ij} = \frac{\partial \boldsymbol{\beta}}{\partial \theta_i} \cdot (\boldsymbol{a}_3 \times \boldsymbol{a}_j) + \frac{1}{R_i} \boldsymbol{a}_i \cdot \left(\frac{\partial \boldsymbol{u}}{\partial \theta_j} - \boldsymbol{\beta} \times \boldsymbol{a}_j \right) \tag{2.63}$$

The last term in Eq. (2.63) is of the same form as that of Eq. (2.49) which, when substituted into Eq. (2.63) results in

$$\Delta b_{ij} = \frac{\partial \boldsymbol{\beta}}{\partial \theta_i} \cdot (\boldsymbol{a}_3 \times \boldsymbol{a}_j) + \frac{A_i A_j}{R_i} \varepsilon_{ij} \tag{2.64}$$

The bending measure of the middle surface is defined as

$$k_{ij} = \frac{1}{A_i A_j} \frac{\partial \boldsymbol{\beta}}{\partial \theta_i} \cdot \left(\boldsymbol{a}_3 \times \boldsymbol{a}_j \right) \tag{2.65}$$

which renders Eq. (2.64) to the form

$$\Delta b_{ij} = A_i A_j \left(k_{ij} + \frac{1}{R_i} \varepsilon_{ij} \right) \tag{2.66}$$

From Eq. (2.13), it is seen that the coefficients of the second fundamental form and hence, Δb_{ij}, are symmetric with respect to the indices i and j. The term k_{ij} introduced in Eq. (2.65) is however, not symmetric in these indices, which is illustrated by first expanding Eq. (2.66) with $i = 1$, $j = 2$, followed by expansion with $i = 2$, $j = 1$ to obtain

$$\begin{aligned} \Delta b_{12} &= A_1 A_2 \left(k_{12} + \frac{1}{R_1} \varepsilon_{12} \right) \\ \Delta b_{21} &= A_1 A_2 \left(k_{21} + \frac{1}{R_2} \varepsilon_{21} \right) \end{aligned} \tag{2.67}$$

respectively. Since $\Delta b_{12} = \Delta b_{21}$ and $\varepsilon_{12} = \varepsilon_{21}$, subtraction of the second line of Eq. (2.67) from the first line yields

$$k_{12} - k_{21} = \left(\frac{1}{R_1} - \frac{1}{R_2} \right) \varepsilon_{12} \tag{2.68}$$

Hence, k_{ij} is only symmetric when $R_1 = R_2$.

In order to characterize the bending of the middle surface by a symmetric tensor, an alternative form for the change in the coefficients of the second fundamental form is considered. Hence, since $b_{ij} = b_{ji}$,

$$\Delta b_{ij} = \tfrac{1}{2} \left(\Delta b_{ij} + \Delta b_{ji} \right) \tag{2.69}$$

It then follows from Eq. (2.66) that

$$\Delta b_{ij} = \tfrac{1}{2} A_i A_j \left(k_{ij} + \frac{1}{R_i} \varepsilon_{ij} + k_{ji} + \frac{1}{R_j} \varepsilon_{ji} \right)$$

$$\Delta b_{ij} = A_i A_j \left[\tfrac{1}{2} \left(k_{ij} + k_{ji} \right) + \tfrac{1}{2} \left(\frac{1}{R_i} + \frac{1}{R_j} \right) \varepsilon_{ij} \right] \tag{2.70}$$

The bending measures of the middle surface, χ_{ij}, are then defined as

$$\chi_{ij} = \tfrac{1}{2} \left(k_{ij} + k_{ji} \right) = \chi_{ji} \tag{2.71}$$

which is symmetric in the indices i and j. Equation (2.71) is substituted into Eq. (2.70) to obtain the final form of the change in the coefficients of the second fundamental form as follows

$$\Delta b_{ij} = A_i A_j \left[\chi_{ij} + \tfrac{1}{2} \left(\frac{1}{R_i} + \frac{1}{R_j} \right) \varepsilon_{ij} \right] \tag{2.72}$$

It is clear that the change in the coefficients of the second fundamental form is dependent on both the bending and stretching of the middle surface.

The explicit form of the bending measures is found through substitution of Eq. (2.65) into Eq. (2.71), which yields

$$\chi_{ij} = \frac{1}{2 A_i A_j} \left[\frac{\partial \boldsymbol{\beta}}{\partial \theta_i} \cdot \left(\boldsymbol{a}_3 \times \boldsymbol{a}_j \right) + \frac{\partial \boldsymbol{\beta}}{\partial \theta_j} \cdot \left(\boldsymbol{a}_3 \times \boldsymbol{a}_i \right) \right] \tag{2.73}$$

The components of the bending measure tensor of the middle surface are found through expansion of Eq. (2.73) on the i and j indices, followed by the indicated operations. This results in

$$\chi_{11} = \frac{1}{A_1} \left(\frac{\partial \beta_1}{\partial \theta_1} + \frac{\beta_2}{A_2} \frac{\partial A_1}{\partial \theta_2} \right) \tag{2.74a}$$

$$\chi_{22} = \frac{1}{A_2} \left(\frac{\partial \beta_2}{\partial \theta_2} + \frac{\beta_1}{A_1} \frac{\partial A_2}{\partial \theta_1} \right) \tag{2.74b}$$

$$\chi_{12} = \chi_{21} = \frac{1}{2} \left[\frac{A_1}{A_2} \frac{\partial}{\partial \theta_2} \left(\frac{\beta_1}{A_1} \right) + \frac{A_2}{A_1} \frac{\partial}{\partial \theta_1} \left(\frac{\beta_2}{A_2} \right) + \left(\frac{1}{R_2} - \frac{1}{R_1} \right) \beta_3 \right] \tag{2.74c}$$

The bending measures depend solely on the rotations β_1, β_2, and β_3 and not upon the strains.

The six quantities ε_{ij} and χ_{ij} determine the changes in the first and second fundamental forms of the middle surface. While not shown here, these quantities also satisfy the equations of compatibility and vanish for rigid body rotations. In this sense, ε_{ij} and χ_{ij} completely determine the deformed configuration of the middle surface of the shell.

To conclude the characterization of the deformation of the middle surface, the changes of curvature and torsion of the middle surface are now derived. The quantities χ_{ij}, identified above as the bending measures of the middle surface of the shell, are often referred to in the literature as the changes of curvature of the middle surface but, this identification is not accurate. The normal curvature of the middle surface shown in Figure 2.2 is again considered. To maintain consistency with the definition of the rotation vector given in Eq. (2.52), the components of the normal change in curvature are taken about the vector normal to the component of interest. Hence,

$$K = \frac{\mathrm{d}\boldsymbol{a}_3}{\mathrm{d}s_i} \cdot \boldsymbol{e}_j = \frac{1}{A_i} \frac{\partial \boldsymbol{a}_3}{\partial \theta_i} \cdot \frac{1}{A_j} \boldsymbol{a}_j = \frac{\frac{\partial \boldsymbol{a}_3}{\partial \theta_i} \cdot \boldsymbol{a}_j}{A_i A_j} = \frac{b_{ij}}{A_i A_j} \tag{2.75}$$

The increment in the curvature in deforming from the reference configuration to the current configuration of the middle surface follows as

$$\Delta \left(\frac{b_{ij}}{A_i A_j} \right) = \frac{1}{A_i A_j} \left[\Delta b_{ij} - b_{ij} \left(\frac{\Delta A_i}{A_i} + \frac{\Delta A_j}{A_j} \right) \right] \tag{2.76}$$

A relation for the terms in parenthesis above is found from Eq. (2.38), by considering only the diagonal terms of the strain tensor.

$$\varepsilon_{ii} = \frac{1}{2} \frac{\Delta a_{ii}}{A_i^2} = \frac{\Delta A_i}{A_i} \quad \text{(no sum over } i) \tag{2.77}$$

Substitution of Eqs. (2.77) and (2.72) into Eq. (2.76) results in

$$\Delta \left(\frac{b_{ij}}{A_i A_j} \right) = \chi_{ij} + \frac{1}{2} \left(\frac{1}{R_i} + \frac{1}{R_j} \right) \varepsilon_{ij} - \frac{b_{ij}}{A_i A_j} \left(\varepsilon_{ii} + \varepsilon_{jj} \right) \tag{2.78}$$

The coefficients of the second fundamental form are given explicitly through combination of Eq. (2.13) with Eq. (2.62) as

$$b_{11} = A_1^2/R_1, \quad b_{12} = b_{21} = 0, \quad b_{22} = A_2^2/R_2 \tag{2.79}$$

From Eq. (2.79), the coefficients can be rewritten in an alternative representation as follows

$$b_{ij} = \tfrac{1}{2} A_i A_j \left(\frac{1}{R_i} + \frac{1}{R_j} \right) \delta_{ij} \tag{2.80}$$

where

$$\delta_{ij} = \begin{cases} 1 & \text{for } i = j \\ 0 & \text{for } i \neq j \end{cases} \tag{2.81}$$

is the Kronecker delta.

The changes of curvature and torsion, κ_{ij}, are obtained by substituting Eq. (2.80) into Eq. (2.78). Hence,

$$\kappa_{ij} = \Delta\left(\frac{b_{ij}}{A_i A_j}\right) = \chi_{ij} + \frac{1}{2}\left(\frac{1}{R_i} + \frac{1}{R_j}\right)\left[\varepsilon_{ij} - 2\varepsilon_{ii}\delta_{ij}\right] \quad \text{(no sum over } \varepsilon_{ii}) \qquad (2.82)$$

Explicitly, the changes of curvature κ_{11} and κ_{22} and the changes of torsion $\kappa_{12} = \kappa_{21}$ are

$$\kappa_{11} = \Delta\left(b_{11}/A_1^2\right) = \chi_{11} - \frac{1}{R_1}\varepsilon_{11} \qquad (2.83\text{a})$$

$$\kappa_{22} = \Delta\left(b_{22}/A_2^2\right) = \chi_{22} - \frac{1}{R_2}\varepsilon_{22} \qquad (2.83\text{b})$$

$$\kappa_{12} = \kappa_{21} = \Delta\left(b_{12}/A_1 A_2\right) = \chi_{12} + \frac{1}{2}\left(\frac{1}{R_1} + \frac{1}{R_2}\right)\varepsilon_{12} \qquad (2.83\text{c})$$

The changes of curvature and torsion are dependent on both the bending measures, χ_{ij}, and stretching measures, ε_{ij}, of the middle surface as a result of the initial curvature of the shell. For a plate, which has zero initial curvature and infinite radii of curvature ($R_1 = R_2 = \infty$), it is seen from Eqs. (2.83) that the changes of curvature and the bending measures are identical, $\kappa_{ij} = \chi_{ij}$.

The distinction between the changes of curvature and the bending measures for shells is important when considering contact between the strata of a layered shell, as well as when formulating the bending energy. The kinematic relations necessary for characterizing the deformation of the middle surface of a shell of a given geometry are now fully defined.

2.2.4   The Spherical Shell

The subsequent chapters of this dissertation are concerned with the application of the general theory of shells to spherical geometries. When considering a spherical coordinate system, the general shell coordinates are taken as $\theta_1 = \varphi$ and $\theta_2 = \theta$. The principal radii of curvature in both directions are each equal to the radius of the sphere in its reference configuration, $R_1 = R_2 = R$. Lastly, for a spherical shell, the Lamé parameters take the form

$$A_1 = R, \quad A_2 = R\sin\varphi \qquad (2.84)$$

The components of the displacement vector, shown for general coordinates in Eq. (2.36), are taken as

$$\boldsymbol{u}\left(\varphi,\theta\right)=u\left(\varphi,\theta\right)\boldsymbol{e}_1+v\left(\varphi,\theta\right)\boldsymbol{e}_2-w\left(\varphi,\theta\right)\boldsymbol{e}_3 \tag{2.85}$$

for the spherical shell with the transverse displacement positive toward the center of the shell. (If the transverse displacement were taken as positive outward, then w would change sign in Eq. (2.85) and all subsequent equations.)

The strain in the middle surface of the spherical shell is obtained through substitution of Eqs. (2.84) and (2.85) into Eq. (2.42). Hence,

$$\varepsilon_{\varphi\varphi}=\frac{1}{R}\left(\frac{\partial u}{\partial\varphi}-w\right) \tag{2.86a}$$

$$\varepsilon_{\theta\theta}=\frac{1}{R}\left(u\cot\varphi+\frac{1}{\sin\varphi}\frac{\partial v}{\partial\theta}-w\right) \tag{2.86b}$$

$$\varepsilon_{\varphi\theta}=\varepsilon_{\theta\varphi}=\frac{1}{2R}\left(\frac{1}{\sin\varphi}\frac{\partial u}{\partial\theta}+\frac{\partial v}{\partial\varphi}-v\cot\varphi\right) \tag{2.86c}$$

The components of the rotation of the middle surface for the spherical shell follow from Eqs. (2.53) and (2.58) as

$$\beta_{\varphi}=\frac{1}{R}\left(u+\frac{\partial w}{\partial\varphi}\right) \tag{2.87a}$$

$$\beta_{\theta}=\frac{1}{R}\left(v+\frac{1}{\sin\varphi}\frac{\partial w}{\partial\theta}\right) \tag{2.87b}$$

$$\beta_{\rho}=\frac{1}{2R}\left(\frac{\partial v}{\partial\varphi}+v\cot\varphi-\frac{1}{\sin\varphi}\frac{\partial u}{\partial\theta}\right) \tag{2.87c}$$

where $\beta_3=\beta_{\rho}$ is the component of the rotation vector about the $\boldsymbol{e}_3$ axis.

The bending measures of the middle surface, Eq. (2.74), are then given in terms of the rotation components as

$$\chi_{\varphi\varphi}=\frac{1}{R}\frac{\partial\beta_{\varphi}}{\partial\varphi} \tag{2.88a}$$

$$\chi_{\theta\theta}=\frac{1}{R}\left(\frac{1}{\sin\varphi}\frac{\partial\beta_{\theta}}{\partial\theta}+\beta_{\varphi}\cot\varphi\right) \tag{2.88b}$$

$$\chi_{\varphi\theta}=\chi_{\theta\varphi}=\frac{1}{2R}\left(\frac{1}{\sin\varphi}\frac{\partial\beta_{\varphi}}{\partial\theta}-\beta_{\theta}\cot\varphi+\frac{\partial\beta_{\theta}}{\partial\varphi}\right) \tag{2.88c}$$

which can further be written in terms of the displacements through substitution of Eqs.

(2.87) into Eqs. (2.88). This results in

$$\chi_{\varphi\varphi} = \frac{1}{R^2} \left(\frac{\partial u}{\partial \varphi} + \frac{\partial^2 w}{\partial \varphi^2} \right) \tag{2.89a}$$

$$\chi_{\theta\theta} = \frac{1}{R^2} \left[\frac{1}{\sin\varphi} \frac{\partial v}{\partial \theta} + \frac{1}{\sin^2\varphi} \frac{\partial^2 w}{\partial \theta^2} + \cot\varphi \left(u + \frac{\partial w}{\partial \varphi} \right) \right] \tag{2.89b}$$

$$\chi_{\varphi\theta} = \chi_{\theta\varphi} = \frac{1}{2R^2} \left[\frac{1}{\sin\varphi} \left(\frac{\partial u}{\partial \theta} - 2\cot\varphi \frac{\partial w}{\partial \theta} + 2\frac{\partial^2 w}{\partial \varphi \partial \theta} \right) - v\cot\varphi + \frac{\partial v}{\partial \varphi} \right] \tag{2.89c}$$

Lastly, the changes of curvature and torsion for the spherical shell follow from Eq. (2.83) as

$$\kappa_{\varphi\varphi} = \frac{1}{R^2} \left(\frac{\partial^2 w}{\partial \varphi^2} + w \right) \tag{2.90a}$$

$$\kappa_{\theta\theta} = \frac{1}{R^2} \left(\frac{1}{\sin^2\varphi} \frac{\partial^2 w}{\partial \theta^2} + \cot\varphi \frac{\partial w}{\partial \theta} + w \right) \tag{2.90b}$$

$$\kappa_{\varphi\theta} = \kappa_{\theta\varphi} = \frac{1}{R^2} \left[\frac{1}{\sin\varphi} \left(\frac{\partial^2 w}{\partial \varphi \partial \theta} - \cot\varphi \frac{\partial w}{\partial \theta} + \frac{\partial u}{\partial \theta} \right) - v\cot\varphi + \frac{\partial v}{\partial \varphi} \right] \tag{2.90c}$$

where it is noted that both $\kappa_{\varphi\varphi}$ and $\kappa_{\theta\theta}$ are dependent solely on the transverse displacement of the spherical shell.

To further illustrate the distinction between the bending measures and the changes of curvature, consider the problem of uniform contraction/expansion of a complete spherical shell. In this case, the displacement of the shell would be purely in the transverse direction independent of the angular coordinates. The shell is not undergoing bending and, hence, the bending measures of Eqs. (2.89) vanish identically. However, the curvature of the shell is changing and the changes of curvature are identified through Eqs. (2.90) as $\kappa_{\varphi\varphi} = \kappa_{\theta\theta} = \pm\frac{w}{R^2}$, where the sign is determined by whether the shell is contracting or expanding.

2.3   Constitutive Relations

With the kinematic relations for the middle surface of the shell established, it is necessary to determine the dependency of the internal resultant forces and moments on the strains and bending measures. Here, the Kirchhoff assumptions of plate theory are extended to shells to obtain the distribution of the displacements and strains through the thickness of the shell. From there, the stress distribution and the moment of the stress distribution are integrated through the thickness to obtain the local resultant forces and moments acting on an element of the shell.

Kirchhoff's assumptions state, that a normal to the undeformed middle surface of the shell remains straight and normal to the deformed middle surface and that the thickness of the shell remains constant during deformation. This is enforced through taking the transverse normal and shear strains acting on the middle surface to vanish. Kirchhoff also neglects the normal stress transverse to the middle surface as small compared to the other normal stress components. The in-plane displacements are taken to vary linearly throughout the thickness of the shell, while the transverse displacement does not very through the thickness. Hence,

$$\tilde{u}_1(\theta_1, \theta_2, \rho) = u_1(\theta_1, \theta_2) + \rho\beta_1 \tag{2.91a}$$

$$\tilde{u}_2(\theta_1, \theta_2, \rho) = u_2(\theta_1, \theta_2) + \rho\beta_2 \tag{2.91b}$$

$$\tilde{w}(\theta_1, \theta_2, \rho) = w(\theta_1, \theta_2) \tag{2.91c}$$

where ρ is the radial coordinate measured outward from the middle surface. In Eqs. (2.91), $u_1(\theta_1, \theta_2)$ and $u_2(\theta_1, \theta_2)$ are the previously introduced in-plane displacements of the middle surface and $\tilde{u}_1(\theta_1, \theta_2, \rho)$ and $\tilde{u}_2(\theta_1, \theta_2, \rho)$ are the in-plane distribution of the displacements through the thickness. The variation of $\tilde{w}(\theta_1, \theta_2, \rho)$ through the thickness is taken to be of higher order.

The distribution of the strains through the thickness is found by posing the strains of the middle surface, found in Eqs. (2.42), in terms of the distribution of the displacements through the thickness given above. The normal strain distributions follow as

$$\tilde{\varepsilon}_{11}(\theta_1, \theta_2, \rho) = \frac{1}{\tilde{A}_1}\frac{\partial \tilde{u}_1}{\partial \theta_1} + \frac{\tilde{u}_2}{\tilde{A}_1\tilde{A}_2}\frac{\partial \tilde{A}_1}{\partial \theta_2} - \frac{\tilde{w}}{\tilde{R}_1} \tag{2.92a}$$

$$\tilde{\varepsilon}_{22}(\theta_1, \theta_2, \rho) = \frac{1}{\tilde{A}_2}\frac{\partial \tilde{u}_2}{\partial \theta_2} + \frac{\tilde{u}_1}{\tilde{A}_1\tilde{A}_2}\frac{\partial \tilde{A}_2}{\partial \theta_1} - \frac{\tilde{w}}{\tilde{R}_2} \tag{2.92b}$$

It was shown in Section 2.2.1 that ε_{ij} is symmetric with respect to its indices, such that $\varepsilon_{12} = \varepsilon_{21}$. It is, however, possible to write the in-plane shear strains in an alternate form in terms of the rotation about the $\boldsymbol{e}_3$ axis. The in-plane shear strain distributions through the thickness of the shell then take the form,

$$\tilde{\varepsilon}_{12}(\theta_1, \theta_2, \rho) = \frac{1}{\tilde{A}_1}\frac{\partial \tilde{u}_2}{\partial \theta_1} - \frac{\tilde{u}_1}{\tilde{A}_1\tilde{A}_2}\frac{\partial \tilde{A}_1}{\partial \theta_2} - \beta_3 \tag{2.93a}$$

$$\tilde{\varepsilon}_{21}(\theta_1, \theta_2, \rho) = \frac{1}{\tilde{A}_2}\frac{\partial \tilde{u}_1}{\partial \theta_2} - \frac{\tilde{u}_2}{\tilde{A}_1\tilde{A}_2}\frac{\partial \tilde{A}_2}{\partial \theta_1} + \beta_3 \tag{2.93b}$$

In Eqs. (2.92) and (2.93), the principal radii and the Lamé parameters at a distance ρ from the middle surface are, respectively,

$$\tilde{R}_1 = R_1 \left(1 + \rho/R_1\right) \quad \text{and} \quad \tilde{R}_2 = R_2 \left(1 + \rho/R_2\right) \tag{2.94a}$$

$$\tilde{A}_1 = A_1 \left(1 + \rho/R_1\right) \quad \text{and} \quad \tilde{A}_2 = A_2 \left(1 + \rho/R_2\right) \tag{2.94b}$$

Substitution of Eqs. (2.91) into Eqs. (2.92) and (2.93) yields the distribution of the strains through the thickness of the shell as

$$\tilde{\varepsilon}_{11} = \varepsilon_{11} + \rho \left[\frac{1}{A_1} \frac{\partial \beta_1}{\partial \theta_1} + \frac{\beta_2}{A_1 A_2} \frac{\partial A_1}{\partial \theta_2} \right] \tag{2.95a}$$

$$\tilde{\varepsilon}_{22} = \varepsilon_{22} + \rho \left[\frac{1}{A_2} \frac{\partial \beta_2}{\partial \theta_2} + \frac{\beta_1}{A_1 A_2} \frac{\partial A_2}{\partial \theta_1} \right] \tag{2.95b}$$

$$\tilde{\varepsilon}_{12} = \varepsilon_{12} + \rho \left[\frac{1}{A_1} \frac{\partial \beta_2}{\partial \theta_1} - \frac{\beta_1}{A_1 A_2} \frac{\partial A_1}{\partial \theta_2} - \frac{\beta_3}{R_1} \right] \tag{2.95c}$$

$$\tilde{\varepsilon}_{21} = \varepsilon_{12} + \rho \left[\frac{1}{A_2} \frac{\partial \beta_1}{\partial \theta_2} - \frac{\beta_2}{A_1 A_2} \frac{\partial A_2}{\partial \theta_1} + \frac{\beta_3}{R_2} \right] \tag{2.95d}$$

where terms of order ρ/R are neglected as small when compared to unity.

The bracketed terms in Eqs. (2.95) are identified through further investigation of the parameter k_{ij} in Eq. (2.65). Combining Eqs. (2.68) and (2.71) yields

$$k_{ij} = \chi_{ij} + \tfrac{1}{2} \left(\frac{1}{R_i} - \frac{1}{R_j} \right) \varepsilon_{ij} \tag{2.96}$$

From Eq. (2.96), it is clear that $k_{11} = \chi_{11}$ and $k_{22} = \chi_{22}$. If Eq. (2.96) is expanded for $i \neq j$, it is seen that the bracketed term in Eq. (2.95c) is identified as k_{12} and that the bracketed term in Eq. (2.95d) is identified as k_{21}. Hence, Eqs. (2.95) are rewritten as follows

$$\tilde{\varepsilon}_{11} = \varepsilon_{11} + \rho k_{11} \tag{2.97a}$$

$$\tilde{\varepsilon}_{22} = \varepsilon_{22} + \rho k_{22} \tag{2.97b}$$

$$\tilde{\varepsilon}_{12} = \varepsilon_{12} + \rho k_{12} \tag{2.97c}$$

$$\tilde{\varepsilon}_{21} = \varepsilon_{12} + \rho k_{21} \tag{2.97d}$$

It was shown in Section 2.2.3 that $k_{12} \neq k_{21}$, unless $R_1 = R_2$. This will be addressed when considering the resultant twisting moments acting on a cross-section of the shell.

The stress distribution through the thickness is related to the strain distribution by Hooke's Law. Hence,

$$\sigma_{11}(\theta_1, \theta_2, \rho) = \frac{E}{1 - \nu^2} (\tilde{\varepsilon}_{11} + \nu \tilde{\varepsilon}_{22}) \tag{2.98a}$$

$$\sigma_{22}(\theta_1, \theta_2, \rho) = \frac{E}{1 - \nu^2} (\tilde{\varepsilon}_{22} + \nu \tilde{\varepsilon}_{11}) \tag{2.98b}$$

$$\sigma_{12}(\theta_1, \theta_2, \rho) = \frac{E}{1 + \nu} \tilde{\varepsilon}_{12} \tag{2.98c}$$

$$\sigma_{21}(\theta_1, \theta_2, \rho) = \frac{E}{1 + \nu} \tilde{\varepsilon}_{21} \tag{2.98d}$$

where E is the Young's modulus of the shell and ν is its Poisson's ratio. The underlying Kirchhoff assumptions take $\sigma_{33} \ll \sigma_{11}, \sigma_{22}$. The resultant internal forces and moments per unit length are obtained by integrating the stress distributions through the thickness, h, of the shell.

The integrals that identify the resultant membrane forces are of the following form

$$N_{11} = \int_{-h/2}^{h/2} \sigma_{11} \left(1 + \frac{\rho}{R_2} \right) \mathrm{d}\rho \tag{2.99a}$$

$$N_{22} = \int_{-h/2}^{h/2} \sigma_{22} \left(1 + \frac{\rho}{R_1} \right) \mathrm{d}\rho \tag{2.99b}$$

$$N_{12} = \int_{-h/2}^{h/2} \sigma_{12} \left(1 + \frac{\rho}{R_2} \right) \mathrm{d}\rho \tag{2.99c}$$

$$N_{21} = \int_{-h/2}^{h/2} \sigma_{21} \left(1 + \frac{\rho}{R_1} \right) \mathrm{d}\rho \tag{2.99d}$$

Terms of order ρ/R are again neglected as small when compared to unity. Carrying through the integration yields

$$N_{11} = C (\varepsilon_{11} + \nu \varepsilon_{22}) \tag{2.100a}$$

$$N_{22} = C (\varepsilon_{22} + \nu \varepsilon_{11}) \tag{2.100b}$$

$$N_{12} = N_{21} = C (1 - \nu) \varepsilon_{12} \tag{2.100c}$$

where

$$C = \frac{Eh}{1 - \nu^2} \tag{2.101}$$

is the membrane stiffness of the shell.

Likewise, the bending and twisting moments per unit length are obtained by integrating the moment of the stress distributions through the thickness of the shell. Hence,

$$\tilde{M}_{11} = \int_{-h/2}^{h/2} \sigma_{11}\rho\left(1 + \frac{\rho}{R_2}\right)\mathrm{d}\rho \tag{2.102a}$$

$$\tilde{M}_{22} = \int_{-h/2}^{h/2} \sigma_{22}\rho\left(1 + \frac{\rho}{R_1}\right)\mathrm{d}\rho \tag{2.102b}$$

$$\tilde{M}_{12} = \int_{-h/2}^{h/2} \sigma_{12}\rho\left(1 + \frac{\rho}{R_2}\right)\mathrm{d}\rho \tag{2.102c}$$

$$\tilde{M}_{21} = \int_{-h/2}^{h/2} \sigma_{21}\rho\left(1 + \frac{\rho}{R_1}\right)\mathrm{d}\rho \tag{2.102d}$$

After neglecting terms of order ρ/R as small when compared to unity, integration yields the bending and twisting moments per unit length as

$$\tilde{M}_{11} = D\left(k_{11} + \nu k_{22}\right) \tag{2.103a}$$

$$\tilde{M}_{22} = D\left(k_{22} + \nu k_{11}\right) \tag{2.103b}$$

$$\tilde{M}_{12} = D\left(1 - \nu\right)k_{12} \tag{2.103c}$$

$$\tilde{M}_{21} = D\left(1 - \nu\right)k_{21} \tag{2.103d}$$

where

$$D = \frac{Eh^3}{12(1 - \nu^2)} \tag{2.104}$$

is the bending stiffness of the shell.

The resultant in-plane shear forces, N_{12} and N_{21} in Eq. (2.100c), are equal since ε_{ij} was shown to be symmetric with respect to its indices in Section 2.2.1. Since k_{ij} is not, in general, symmetric with respect to its indices, neither are the resultant moments appearing in Eq. (2.103). As such the resultant bending moments in Eq. (2.103), $\tilde{M}_{ij}$, have been identified with a tilde to identify them as non-symmetric with respect to the indices.

The non-symmetric resultant bending moments, $\tilde{M}_{ij}$, can be represented as the sum of a symmetric component, M_{ij}, and a skew-symmetric component, M_{ij}^{skew}, as follows

$$\tilde{M}_{ij} = M_{ij} + M_{ij}^{skew} \tag{2.105}$$

where the symmetric and skew-symmetric bending moment components are defined as

$$M_{ij} = \tfrac{1}{2} \left(\tilde{M}_{ij} + \tilde{M}_{ji} \right) = M_{ji} \tag{2.106a}$$

$$M_{ij}^{skew} = \tfrac{1}{2} \left(\tilde{M}_{ij} - \tilde{M}_{ji} \right) = -M_{ji}^{skew} \tag{2.106b}$$

Substitution of Eqs. (2.103) into Eq. (2.106a) yields the symmetric bending components

$$M_{11} = D \left(\chi_{11} + \nu \chi_{22} \right) \tag{2.107a}$$

$$M_{22} = D \left(\chi_{22} + \nu \chi_{11} \right) \tag{2.107b}$$

$$M_{12} = M_{21} = D \left(1 - \nu \right) \chi_{12} \tag{2.107c}$$

while, substitution of Eqs. (2.103) into Eq. (2.106b) yields the skew-symmetric bending components

$$M_{11}^{skew} = M_{22}^{skew} = 0 \tag{2.108a}$$

$$M_{12}^{skew} = \tfrac{1}{2} D \left(1 - \nu \right) \left(k_{12} - k_{21} \right) \tag{2.108b}$$

$$M_{21}^{skew} = \tfrac{1}{2} D \left(1 - \nu \right) \left(k_{21} - k_{12} \right) \tag{2.108c}$$

Equations (2.100), (2.103), (2.107), and (2.108) will be used to present the elastic strain energy of the shell in terms of the six contact quantities N_{11}, N_{22}, N_{12}, M_{11}, M_{22}, and M_{12}.

2.4   Elastic Strain Energy

The elastic strain energy of the shell takes the form

$$U = \frac{1}{2} \iiint\limits_{\theta_1\ \theta_2\ \rho} \left(\sigma_{11}\tilde{\varepsilon}_{11} + \sigma_{22}\tilde{\varepsilon}_{22} + \sigma_{12}\tilde{\varepsilon}_{12} + \sigma_{21}\tilde{\varepsilon}_{21} \right) \tilde{A}_1 \tilde{A}_2 \mathrm{d}\theta_1 \mathrm{d}\theta_2 \mathrm{d}\rho \tag{2.109}$$

Integrating through the thickness, and incorporating Eqs. (2.97), (2.99), and (2.102), gives

$$U = \frac{1}{2} \iint\limits_{\theta_1\ \theta_2} \left(N_{11}\varepsilon_{11} + N_{22}\varepsilon_{22} + N_{12}\varepsilon_{12} + N_{21}\varepsilon_{21} \right.$$
$$\left. + \tilde{M}_{11}k_{11} + \tilde{M}_{22}k_{22} + \tilde{M}_{12}k_{12} + \tilde{M}_{21}k_{21} \right) A_1 A_2 \mathrm{d}\theta_1 \mathrm{d}\theta_2 \tag{2.110}$$

where terms of order ρ/R have been neglected as small compared to unity.

As $\tilde{M}_{ij}$ is not symmetric with respect to its indices, Eq. (2.110) is shown in terms of seven contact quantities rather than the common form of six contact quantities. In order

to rectify this, Eq. (2.110) is rewritten as

$$U = \frac{1}{2} \iint_{\theta_1 \theta_2} \sum_{i=1}^{2} \sum_{j=1}^{2} \left(N_{ij}\varepsilon_{ij} + \tilde{M}_{ij}k_{ij} \right) A_1 A_2 \mathrm{d}\theta_1 \mathrm{d}\theta_2 \tag{2.111}$$

Substitution of Eqs. (2.96) and (2.105) into the summation in Eq. (2.111) yields

$$\begin{aligned}
N_{ij}\varepsilon_{ij} + \tilde{M}_{ij}k_{ij} &= N_{ij}\varepsilon_{ij} + \left(M_{ij} + M_{ij}^{skew} \right) \left[\chi_{ij} + \frac{1}{2}\left(\frac{1}{R_i} - \frac{1}{R_j} \right) \varepsilon_{ij} \right] \\
&= \left[N_{ij} + \frac{1}{2}\left(\frac{1}{R_i} - \frac{1}{R_j} \right) M_{ij}^{skew} \right] \varepsilon_{ij} + M_{ij}\chi_{ij}
\end{aligned} \tag{2.112}$$

where the property that the sum of the products of the components of a symmetric and a skew-symmetric quantity vanish identically has been incorporated. Substitution of Eqs. (2.106b), (2.103c), (2.103d), and (2.68), respectively, into Eq. (2.112) results in

$$\begin{aligned}
N_{ij}\varepsilon_{ij} + \tilde{M}_{ij}k_{ij} &= \left[N_{ij} + \frac{1}{4}\left(\frac{1}{R_i} - \frac{1}{R_j} \right)\left(\tilde{M}_{ij} - \tilde{M}_{ji} \right) \right] \varepsilon_{ij} + M_{ij}\chi_{ij} \\
&= \left[N_{ij} + \frac{1}{4}D\left(1 - \nu \right)\left(\frac{1}{R_i} - \frac{1}{R_j} \right)\left(k_{ij} - k_{ji} \right) \right] \varepsilon_{ij} + M_{ij}\chi_{ij} \\
&= \left[N_{ij} + \frac{1}{4}D\left(1 - \nu \right)\left(\frac{1}{R_i} - \frac{1}{R_j} \right)^2 \varepsilon_{ij} \right] \varepsilon_{ij} + M_{ij}\chi_{ij}
\end{aligned} \tag{2.113}$$

Finally, Eq. (2.100c) is substituted into the last line of Eq. (2.113) to obtain

$$N_{ij}\varepsilon_{ij} + \tilde{M}_{ij}k_{ij} = \left[1 + \frac{1}{48}h^2 \left(\frac{1}{R_i} - \frac{1}{R_j} \right)^2 \right] N_{ij}\varepsilon_{ij} + M_{ij}\chi_{ij} \tag{2.114}$$

As terms of order ρ/R have been neglected with respect to unity in the development of the constitutive relations and the strain energy, terms of order $(\rho/R)^2$ must also be neglected with respect to unity for a consistent formulation. Hence, the second term within the brackets of Eq. (2.114) must be neglected since the thickness, h, is of the same order as the radial coordinate ρ. Equation (2.114) is then substituted back into Eq. (2.111), which results in

$$U = \frac{1}{2} \iint_{\theta_1 \theta_2} \sum_{i=1}^{2} \sum_{j=1}^{2} \left(N_{ij}\varepsilon_{ij} + M_{ij}\chi_{ij} \right) A_1 A_2 \mathrm{d}\theta_1 \mathrm{d}\theta_2 \tag{2.115}$$

Expansion of the summation in Eq. (2.115) results in the standard form of the elastic strain energy as

$$U = \frac{1}{2} \iint_{\theta_1 \theta_2} \left(N_{11}\varepsilon_{11} + N_{22}\varepsilon_{22} + 2N_{12}\varepsilon_{12} + M_{11}\chi_{11} + M_{22}\chi_{22} + 2M_{12}\chi_{12} \right) A_1 A_2 \mathrm{d}\theta_1 \mathrm{d}\theta_2 \tag{2.116}$$

which is represented in standard form in terms of the six contact quantities identified in Eqs. (2.100) and (2.107).

2.5 Detachment Propagation in Layered Shells

The kinematic and constitutive equations presented in Sections 2.2 and 2.3, respectively, along with the elastic strain energy presented in the previous Section, are now applied to model the evolution of a detaching layered composite elastic shell. Shells with a compliant inner layer separating from a rigid outer layer are considered and the delamination boundary between layers is allowed to take on an arbitrary shape.

2.5.1 Geometry of a Delaminating Composite Shell

The shell is divided into three regions; Region $\mathcal{R}_1$: the 'lift zone', Region $\mathcal{R}_2$: the 'contact zone' where the shell layers maintain sliding contact with each other, and Region $\mathcal{R}_3$: the 'intact region' where the shell layers remain perfectly bonded, all as shown in Figure 2.5.
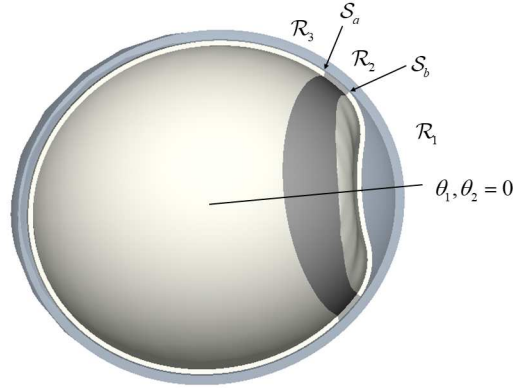
Figure 2.5: Cross section of the delaminating shell, depicting the 'lift zone' $\mathcal{R}_1$, 'contact zone' $\mathcal{R}_2$, and 'intact region' $\mathcal{R}_3$, which are separated by surfaces $\mathcal{S}_b$ and $\mathcal{S}_a$, respectively.

The 'lift zone' is the area where the two shell layers have separated and are no longer in contact with each other. It is defined from the origin of the shell at $\theta_1 = \theta_2 = 0$ up to a lift zone boundary surface identified as $\mathcal{S}_b$. Alternatively, if a hole identified as boundary Surface $\mathcal{S}_c$, which encloses the origin, is present, the lift zone is defined as the region between Surfaces $\mathcal{S}_c$ and $\mathcal{S}_b$.

In the 'contact zone', the bond between the shell layers has been broken, but the shell layers remain in sliding contact with one another (Bottega [8], [9], [10], and [11]). The

transverse deflection, w, of each layer must remain identical for the two layers to remain in contact, though the in-plane displacements, u_1 and u_2 need not be the same. The contact zone is identified as the region extending from Surface $\mathcal{S}_b$ to the contact zone boundary surface identified as $\mathcal{S}_a$

The 'intact region' describes the region of the structure where the two shells remain perfectly adhered to one another and cannot move independently of each other. As the outer layer is assumed rigid for the current case, the inner layer will conform to the shape of the the outer in the intact region. The intact region is defined in the area from Surface $\mathcal{S}_a$ to the pole opposite of $\theta_1 = \theta_2 = 0$.

2.5.2 Energy Formulation

The problem is approached as a propagating boundary value problem in the calculus of variations, where the location of the boundary surfaces between the lift zone and contact zone and between the contact zone and intact region are allowed to vary arbitrarily, as well as the elastic deflections of the detaching inner shell layer.

The potential energy functional, Π, for the composite shell structure is comprised of the elastic strain energy of the inner layer, U, and the work done by the applied loads acting on the inner layer, $\mathcal{W}$. In addition, we include a constraint functional, Λ, to ensure the appropriate continuity of the displacements with the rigid outer layer in the contact zone and in the intact region. Lastly, the energy of detachment, Γ, is the energy released as detachment propagates and the bond between the shell layers is broken.

The potential energy functional follows as

$$\Pi = \sum_{j=1}^{3} (U_j - \mathcal{W}_j) - \Lambda + \Gamma \tag{2.117}$$

where U_j is the elastic strain energy of Eq. (2.116) for Region $\mathcal{R}_j$ ($j = 1 - 3$). Hence,

$$U_j = \frac{1}{2} \int_{\mathcal{R}_j} \left(N_{11}^{(j)} \varepsilon_{11}^{(j)} + N_{22}^{(j)} \varepsilon_{22}^{(j)} + 2N_{12}^{(j)} \varepsilon_{12}^{(j)} \right.$$
$$\left. + M_{11}^{(j)} \chi_{11}^{(j)} + M_{22}^{(j)} \chi_{22}^{(j)} + 2M_{12}^{(j)} \chi_{12}^{(j)} \right) A_1 A_2 \mathrm{d}\theta_1 \mathrm{d}\theta_2 \tag{2.118}$$

The work, $\mathcal{W}_j$, done by general distributed loads, $\boldsymbol{q}^{(j)}(\theta_1, \theta_2)$, in deforming the shell structure in Region $\mathcal{R}_j$ is

$$\mathcal{W}_j = \int\limits_{\mathcal{R}_j} \left(q_1^{(j)} u_1^{(j)} + q_2^{(j)} u_2^{(j)} + q_3^{(j)} w_j \right) A_1 A_2 \mathrm{d}\theta_1 d\theta_2 \tag{2.119}$$

The constraint functional is given as

$$\Lambda = \int\limits_{\mathcal{R}_2} \hat{\sigma}_2 w_2 A_1 A_2 \mathrm{d}\theta_1 d\theta_2 + \int\limits_{\mathcal{R}_3} \left(\hat{\tau}_1^{(3)} u_1^{(3)} + \hat{\tau}_2^{(3)} u_2^{(3)} + \hat{\sigma}_3 w_3 \right) A_1 A_2 \mathrm{d}\theta_1 d\theta_2 \tag{2.120}$$

where $\hat{\sigma}_2$, $\hat{\sigma}_3$, $\hat{\tau}_1^{(3)}$, and $\hat{\tau}_2^{(3)}$ are Lagrange multipliers that ensure continuity of the transverse and meridian displacements of the shell layers in the intact region and continuity of the transverse displacement in the contact zone. Physically, the Lagrange multipliers correspond to the interfacial radial normal stress between the shell layers in the contact zone and the interfacial radial normal stress and meridian shear stresses in the intact region, respectively.

The energy of detachment is given as

$$\Gamma = \int\limits_{\mathcal{R}_1 + \mathcal{R}_2} 2\gamma A_1 A_2 \mathrm{d}\theta_1 d\theta_2 - \int\limits_{\mathcal{R}_{1_0} + \mathcal{R}_{2_0}} 2\gamma A_1 A_2 \mathrm{d}\theta_1 d\theta_2 \tag{2.121}$$

where γ is the energy required to produce a unit area of detachment between the shell layers and is a material property of that particular interface. Regions $\mathcal{R}_{1_0}$ and $\mathcal{R}_{2_0}$ comprise the initial configuration of the delaminated shell prior to the propagation of detachment.

Applying the Principle of Stationary Potential Energy to Eq. (2.117), while allowing the displacements $u_1^{(j)}$, $u_2^{(j)}$, and w_j, along with the boundary Surfaces $\mathcal{S}_a$ and $\mathcal{S}_b$ to vary, yields the self-consistent governing equations, boundary conditions, and transversality conditions of the evolving shell structure. The Principle of Stationary Potential Energy is mathematically represented as

$$\delta \Pi = 0 \tag{2.122}$$

2.5.3 Governing Equations

Substitution of Eq. (2.117) into Eq. (2.122) and performing the indicated variations gives the equations of equilibrium for the inner shell layer in Region $\mathcal{R}_j$ (for $j = 1, 2, 3$) as

$$\frac{\partial}{\partial\theta_1}\left(A_2 N_{11}^{(j)}\right) + \frac{\partial}{\partial\theta_2}\left(A_1 N_{12}^{(j)}\right) - \frac{\partial A_2}{\partial\theta_1}N_{22}^{(j)} + \frac{\partial A_1}{\partial\theta_2}N_{12}^{(j)}$$
$$+ \frac{A_1 A_2}{R_1}Q_1^{(j)} + \frac{A_1}{2}\left(\frac{1}{R_1} - \frac{1}{R_2}\right)\frac{\partial M_{12}^{(j)}}{\partial\theta_2} = -A_1 A_2\left(q_1 + \hat{\tau}_1^{(j)}\right) \tag{2.123a}$$

$$\frac{\partial}{\partial\theta_1}\left(A_2 N_{12}^{(j)}\right) + \frac{\partial}{\partial\theta_2}\left(A_1 N_{22}^{(j)}\right) + \frac{\partial A_2}{\partial\theta_1}N_{12}^{(j)} - \frac{\partial A_1}{\partial\theta_2}N_{11}^{(j)}$$
$$+ \frac{A_1 A_2}{R_2}Q_2^{(j)} + \frac{A_2}{2}\left(\frac{1}{R_2} - \frac{1}{R_1}\right)\frac{\partial M_{12}^{(j)}}{\partial\theta_1} = -A_1 A_2\left(q_2 + \hat{\tau}_2^{(j)}\right) \tag{2.123b}$$

$$\frac{\partial}{\partial\theta_1}\left(A_2 Q_1^{(j)}\right) + \frac{\partial}{\partial\theta_2}\left(A_1 Q_2^{(j)}\right) - A_1 A_2\left(\frac{N_{11}^{(j)}}{R_1} + \frac{N_{22}^{(j)}}{R_2}\right) = A_1 A_2\left(q_3 + \hat{\sigma}_j\right) \tag{2.123c}$$

where

$$Q_1^{(j)} = \frac{1}{A_1 A_2}\left[\frac{\partial}{\partial\theta_1}\left(A_2 M_{11}^{(j)}\right) + \frac{\partial}{\partial\theta_2}\left(A_1 M_{12}^{(j)}\right) - \frac{\partial A_2}{\partial\theta_1}M_{22}^{(j)} + \frac{\partial A_1}{\partial\theta_2}M_{12}^{(j)}\right] \tag{2.124a}$$

$$Q_2^{(j)} = \frac{1}{A_1 A_2}\left[\frac{\partial}{\partial\theta_1}\left(A_2 M_{12}^{(j)}\right) + \frac{\partial}{\partial\theta_2}\left(A_1 M_{22}^{(j)}\right) + \frac{\partial A_2}{\partial\theta_1}M_{12}^{(j)} - \frac{\partial A_1}{\partial\theta_2}M_{11}^{(j)}\right] \tag{2.124b}$$

represent the transverse shear forces in Region $\mathcal{R}_j$.

On the right hand side of Eqs. (2.123)

$$\hat{\sigma}_1 = \hat{\tau}_1^{(1)} = \hat{\tau}_1^{(2)} = \hat{\tau}_2^{(1)} = \hat{\tau}_2^{(2)} = 0 \tag{2.125}$$

while $\hat{\sigma}_2$, $\hat{\sigma}_3$, $\hat{\tau}_1^{(3)}$, and $\hat{\tau}_2^{(3)}$ are the Lagrange multipliers identified in the previous Section. Additionally, from the constraint functional,

$$u_1^{(3)} = 0 \tag{2.126a}$$

$$u_2^{(3)} = 0 \tag{2.126b}$$

$$w_2 = w_3 = 0 \tag{2.126c}$$

since the outer shell layer is taken to be rigid.

2.5.4 Boundary Conditions

The boundary conditions for the detaching shell layer are also found from the variational formulation. The boundary conditions acting on a hole defined by Surface $\mathcal{S}_c$ are found to

be

$$N_{nn}^{(1)}\bigg|_{\mathcal{S}_c} = 0, \qquad M_{nn}^{(1)}\bigg|_{\mathcal{S}_c} = 0, \qquad V_n^{(1)}\bigg|_{\mathcal{S}_c} = 0, \qquad V_t^{(1)}\bigg|_{\mathcal{S}_c} = 0 \tag{2.127}$$

where the effective resultant transverse shear force, $V_n^{(j)}$ and the effective resultant in-plane shear force, $V_s^{(j)}$, that act on the boundary surface are, respectively,

$$V_n^{(j)} = Q_n^{(j)} + \frac{1}{A_t}\frac{\partial M_{nt}^{(j)}}{\partial \theta_t} \tag{2.128a}$$

$$V_t^{(j)} = N_{nt}^{(j)} + \frac{1}{2}\left(\frac{3}{R_t} - \frac{1}{R_n}\right)M_{nt}^{(j)} \tag{2.128b}$$

In Eqs. (2.127) the subscript n represents the direction normal to the boundary and the subscript t represents the direction tangential to the boundary. An orthogonal coordinate transformation relates the θ_1, θ_2 coordinates to the n, t coordinates as shown in Figure 2.6. The transformation in terms of the rotation angle, α, about the e_3 axis is given as

$$\boldsymbol{B} = \begin{bmatrix} \cos\alpha & \sin\alpha \\ -\sin\alpha & \cos\alpha \end{bmatrix} \tag{2.129}$$
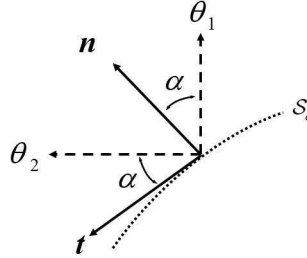
Figure 2.6: Coordinate transformation from θ_1, θ_2 coordinates to normal, n, and tangential, t, coordinates.

Moreover, the in-plane displacements transform as

$$\begin{Bmatrix} u_n \\ u_t \end{Bmatrix} = \boldsymbol{B} \begin{Bmatrix} u_1 \\ u_2 \end{Bmatrix} \tag{2.130}$$

Finally, the resultant membrane forces and bending moments in n, t coordinates are, respectively,

$$\begin{bmatrix} N_{nn} & N_{nt} \\ N_{nt} & N_{tt} \end{bmatrix} = \boldsymbol{B}\begin{bmatrix} N_{11} & N_{12} \\ N_{21} & N_{22} \end{bmatrix}\boldsymbol{B}^T \tag{2.131a}$$

$$\begin{bmatrix} M_{nn} & M_{nt} \\ M_{nt} & M_{tt} \end{bmatrix} = \boldsymbol{B} \begin{bmatrix} M_{11} & M_{12} \\ M_{21} & M_{22} \end{bmatrix} \boldsymbol{B}^T \tag{2.131b}$$

while the strains and bending measures transform similarly as

$$\begin{bmatrix} \varepsilon_{nn} & \varepsilon_{nt} \\ \varepsilon_{nt} & \varepsilon_{tt} \end{bmatrix} = \boldsymbol{B} \begin{bmatrix} \varepsilon_{11} & \varepsilon_{12} \\ \varepsilon_{21} & \varepsilon_{22} \end{bmatrix} \boldsymbol{B}^T \tag{2.132a}$$

$$\begin{bmatrix} \chi_{nn} & \chi_{nt} \\ \chi_{nt} & \chi_{tt} \end{bmatrix} = \boldsymbol{B} \begin{bmatrix} \chi_{11} & \chi_{12} \\ \chi_{21} & \chi_{22} \end{bmatrix} \boldsymbol{B}^T \tag{2.132b}$$

Through these relations, the relevant parameters in n, t coordinates can be written in terms of θ_1, θ_2 coordinates,

The remaining boundary conditions depend on the existence or absence of the contact zone, Region $\mathcal{R}_2$. Although the model allows for a contact zone, one may not be physically realizable for a given detachment size and load condition. The transversality conditions, which are discussed in Section 2.5.5, determine the size and existence of the contact zone.

When a *contact zone is present*, the boundary conditions on Surface $\mathcal{S}_b$ are

$$u_n^{(1)}\bigg|_{\mathcal{S}_b} = u_n^{(2)}\bigg|_{\mathcal{S}_b}, \quad u_t^{(1)}\bigg|_{\mathcal{S}_b} = u_t^{(2)}\bigg|_{\mathcal{S}_b}, \quad w_1\bigg|_{\mathcal{S}_b} = 0, \quad \beta_n^{(1)}\bigg|_{\mathcal{S}_b} = \beta_n^{(2)}\bigg|_{\mathcal{S}_b}$$
$$N_{nn}^{(1)}\bigg|_{\mathcal{S}_b} = N_{nn}^{(2)}\bigg|_{\mathcal{S}_b}, \quad V_t^{(1)}\bigg|_{\mathcal{S}_b} = V_t^{(2)}\bigg|_{\mathcal{S}_b} \tag{2.133}$$

while the boundary conditions on Surface $\mathcal{S}_a$ are

$$u_n^{(2)}\bigg|_{\mathcal{S}_a} = 0, \quad u_t^{(2)}\bigg|_{\mathcal{S}_a} = 0 \tag{2.134}$$

When a *contact zone is absent*, Region $\mathcal{R}_2$ does not exist and we take Surface $\mathcal{S}_b$ and $\mathcal{S}_a$ to coincide as the boundary surface between the lift zone, $\mathcal{R}_1$, and the intact region, $\mathcal{R}_3$. In this case, the conditions stated in Eqs. (2.133) and (2.134) are negated and the boundary conditions on $\mathcal{S}_a$ are

$$u_n^{(1)}\bigg|_{\mathcal{S}_a} = 0, \quad u_t^{(1)}\bigg|_{\mathcal{S}_a} = 0, \quad w_1\bigg|_{\mathcal{S}_a} = 0, \quad \beta_n^{(1)}\bigg|_{\mathcal{S}_a} = 0 \tag{2.135}$$

For arbitrarily shaped boundary surfaces, the boundary conditions in Eqs. (2.127) and (2.133)-(2.135) must be satisfied point-wise along the specified boundary surface.

Surfaces $\mathcal{S}_b$ and $\mathcal{S}_a$ are not fixed. Rather, they are found as part of the solution to the mathematical problem. Allowing the location of these surfaces to vary arbitrarily when performing the variations yields the transversality conditions that establish the location of the propagating boundaries that correspond to equilibrium configurations of the detaching shell structure.

2.5.5 Transversality Conditions

Two possibilities are considered: (i) a contact zone is present and (ii) a contact zone is absent.

(i) When a *contact zone is present*, the condition that establishes the location of the propagating contact zone boundary surface, $\mathcal{S}_b$, is found to be

$$\left[\mathcal{H}_n^{(1)} - \mathcal{F}_n^{(1)} \right]_{\mathcal{S}_b} = \left[\mathcal{H}_n^{(2)} - \mathcal{F}_n^{(2)} \right]_{\mathcal{S}_b} \tag{2.136}$$

where

$$\mathcal{F}_n^{(j)} = \frac{1}{2} \left[N_{nn}^{(j)} \varepsilon_{nn}^{(j)} + N_{tt}^{(j)} \varepsilon_{tt}^{(j)} + 2N_{nt}^{(j)} \varepsilon_{nt}^{(j)} + M_{nn}^{(j)} \chi_{nn}^{(j)} + M_{tt}^{(j)} \chi_{tt}^{(j)} + 2M_{nt}^{(j)} \chi_{nt}^{(j)} \right] \tag{2.137}$$

and

$$\mathcal{H}_n^{(j)} = \frac{1}{A_n} \left[N_{nn}^{(j)} \frac{\partial u_n^{(j)}}{\partial \theta_n} + V_t^{(j)} \frac{\partial u_t^{(j)}}{\partial \theta_n} - V_n^{(j)} \frac{\partial w_j}{\partial \theta_n} + M_{nn}^{(j)} \frac{\partial \beta_n^{(j)}}{\partial \theta_n} \right] \tag{2.138}$$

In addition, the condition that establishes the location of the propagating detachment boundary surface, $\mathcal{S}_a$, takes the form

$$\mathcal{G} \Big|_{\mathcal{S}_a} = \left[\mathcal{H}_n^{(2)} - \mathcal{F}_n^{(2)} \right]_{\mathcal{S}_a} = 2\gamma \tag{2.139}$$

In Eq. (2.139), the function $\mathcal{G} \Big|_{\mathcal{S}_a}$ is identified as the *energy release rate* (energy released per unit increase of the detachment boundary) of the detaching inner shell layer.

(ii) When a *contact zone is absent*, Eq. (2.136) becomes invalid. For this case, $\mathcal{S}_a$ and $\mathcal{S}_b$ represent the same boundary surface and Eq. (2.139) is superfluous. The transversality condition that establishes the detachment boundary surface, $\mathcal{S}_a$, for this case is found to be given by

$$\mathcal{G} \Big|_{\mathcal{S}_a} = \left[\mathcal{H}_n^{(1)} - \mathcal{F}_n^{(1)} \right]_{\mathcal{S}_a} = 2\gamma \tag{2.140}$$

The multi-directional growth laws given in Eqs. (2.136), (2.139), and (2.140) are associated with the following Griffith-type criterion [32]: if $\mathcal{G}\big|_{\mathcal{S}_a^*} \geq 2\gamma$ for some initial value, $\mathcal{S}_a^*$, of the detachment surface, $\mathcal{S}_a$, propagation of that detachment surface will occur with $\mathcal{S}_a$ increasing until the equality is satisfied. If $\mathcal{G}\big|_{\mathcal{S}_a^*} < 2\gamma$, propagation will not occur. Hence, the growth laws for an arbitrarily shaped surface must be satisfied point-wise along the boundary surface. The surface will propagate and evolve to a final equilibrium configuration for which $\mathcal{G}\big|_{\mathcal{S}_a} < 2\gamma$ at all points along the boundary. When a contact zone is present, the contact zone boundary will evolve until Eq. (2.136) is satisfied at all points along the contact zone boundary. Equations (2.139) and (2.140) are analogous to the growth law for arbitrary shaped delaminations in layered plates derived in Bottega [7], for which contact zones were not considered.

Chapter 3

The Mechanics of Retinal Detachment in Emmetropic Eyes

3.1 Introduction

The theory of thin elastic shells and the corresponding growth law for detachment propaga-
tion in layered shells developed in the previous Chapter is now applied to model the propa-
gation of retinal detachment in emmetropic eyes. The retina is modeled as a thin spherical
elastic shell while treating the much stiffer RPE-choroid-sclera composite structure as rigid.
Axisymmetric deformation and detachment is considered, and linear strain-displacement
relations are assumed for the retina. This mechanics based mathematical model for retinal
detachment, which incorporates an energy-based criterion for detachment propagation, was
originally developed in Bottega *et al.* [12]. The goal of that study was to provide a substan-
tial first step in elucidating the mechanics of the phenomenon since, to the knowledge of
the authors, no analytical studies directly pertaining to the mechanics of a detaching retina
had been reported in the literature to that date.

In Bottega *et al.* [12], the meridian displacements of the retina are treated as negligible
in order to simplify the coupled equations of equilibrium derived therein into a single dif-
ferential equation in terms of the radial displacements. When considering deformations of
a complete sphere under symmetric loading, the meridian displacements do in fact vanish
identically and the obtained solution remains exact. For the present case, however, the
uniform symmetry of the sphere is altered by the presence of the detached region and/or
the tear. As a result, while the meridian displacements will be small compared to the radial
displacements, their effects will not necessarily be negligible. In order to improve upon the

---

Portions of this Chapter previously appeared as: Lakawicz, J.M., Bottega, W.J., Prenner, J.L., and
Fine, H.F., 2015. An analysis of the mechanical behaviour of a detaching retina. *Math. Med. Biol.*, 32(2),
137-161.

results of Bottega *et al.* [12], the meridian displacements are retained and a more accurate analytical solution for the model for retinal detachment in emmetropic eyes is obtained.

This Chapter aims to improve upon the results of Bottega *et al.* [12] by retaining the contribution of meridian displacements and, hence, providing a more accurate solution to the mathematical model for retinal detachment propagation in emmetropic eyes either with or without a central tear in the retina. In young healthy eyes, the vitreous body is composed of a gel that fills the vitreous cavity and is randomly interspersed with collagen fibrils. As the eye ages, the vitreous liquefies leading to the collapse of the matrix of collagen fibrils which, in turn exerts traction on the vitreoretinal interface (Sebag [71]). Additionally, when fluid accumulates in the subretinal space or enters the subretinal space through a hole/tear in the retina, the pressure in the subretinal space may exceed the intraocular pressure (IOP) which could induce retinal detachment. Hence, contraction of the vitreous and extension of its fibrils, along with a pressure difference across the retina, are taken as the stimuli for detachment propagation. In this regard, the model represents the three types of retinal detachment, known as exudative, tractional, and rhegmatogenous retinal detachment, the latter being the most common type of retinal detachment (see, for example, Gariano & Kim [25]).

The problem is approached as a propagating boundary value problem in the calculus of variations, where the interior boundary between the lift zone and the contact zone, φ_1, and the boundary between the contact zone and the intact region, φ_2, are allowed to vary arbitrarily (see Figure 3.1), as well as the deflections of the retina along and transverse to the meridian. In addition to the equilibrium equations, boundary, and matching conditions, the variational formulation yields the self-consistent energy release rate that governs detachment, and formulae for critical stress and critical deflections that provide a rational basis for measuring critical parameters. The equilibrium equations, boundary conditions, and energy release rate, all follow from the theory presented in Chapter 2 when applied specifically to spherical elastic shells with axisymmetric deflection profiles.

The formulation of the mathematical model for retinal detachment propagation in the emmetropic eye is presented in Section 3.2, which follows. Exact solutions for the equilibrium equations derived in the formulation are presented in Section 3.3. Results based on
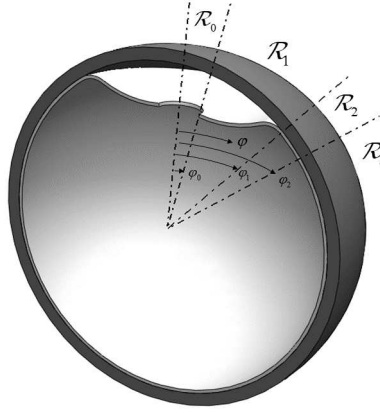
Figure 3.1: Cross section of the eye with a detaching retina, depicting a tear in Region $\mathcal{R}_0$; 'lift zone' $\mathcal{R}_1$, 'contact zone' $\mathcal{R}_2$, and 'intact region' $\mathcal{R}_3$. For the case of no tear in the retina, Region $\mathcal{R}_0$ is not present.

those solutions are presented in Section 3.5. Pertinent results are then compared with those of Bottega *et al.* [12], demonstrating the importance of retaining the meridian displacements in such analyses.

3.2 Problem Formulation

In this section, the formulation of the problem of quasi-static retinal detachment in emmetropic eyes due to stress acting on the retina from vitreous fibrils, as well as due to the presence of a pressure difference across the retina is stated. In this idealized model the retina, sclera, and choroid are treated as spherical structures and axisymmetric deformations and detachment are considered. In this context, the retina is modeled as a thin elastic shell detaching from a 'rigid' RPE-choroid-sclera composite structure.

The retina is modeled as a spherical elastic shell of radius R, thickness h, Young's modulus E, and Poisson's ratio ν. Spherical coordinates, (r, θ, φ), are used to describe the evolving ocular structure, where r is the radial coordinate, θ is the polar angle, and φ is the azimuth angle. Symmetry is assumed about the $\varphi = 0$ axis and over the domain $0 \leq \theta \leq 2\pi$, with the center of the detached region located at the coordinates $r = R$, $\varphi = 0$. The transverse displacement of the center surface of the retina, $w(\varphi)$, is taken as positive inward, while the meridian displacement, $u(\varphi)$, is taken as positive in the direction

of increasing azimuth angle, φ. Due to the axisymmetry about $\varphi = 0$, the deformation will be the same for all values of the polar angle, θ.

The domain of the retina is $r \in [R - h/2, R + h/2]$, $\varphi \in [\varphi_0, \pi]$, $\theta \in [0, 2\pi]$, where φ_0 is the meridian angle of the tear. The case of a retina without a tear ($\varphi_0 = 0$) and the case of a retina with a tear ($\varphi_0 > 0$), as depicted in Figure 3.1, are considered. The region of the retinal tear is designated as $\mathcal{R}_0$: $\varphi \in [0, \varphi_0]$, while the detached segment of the retina is divided into two regions; Region $\mathcal{R}_1$: $\varphi \in [\varphi_0, \varphi_1]$, the 'lift zone', and Region $\mathcal{R}_2$: $\varphi \in [\varphi_1, \varphi_2]$, the 'contact zone'. The latter corresponds to a region of sliding contact and borders on Region $\mathcal{R}_3$: $\varphi \in [\varphi_2, \pi]$, where the bond between the retina and the RPE remains intact.

A pressure difference across the retina, p, which accounts for fluid entering the subretinal pocket that develops as the retina detaches, and stress from the fibrils of the contracting vitreous, σ_v, act as the loading parameters in the mathematical model. The stress from the vitreous fibrils is a distributed stress that acts on the retina in the sense shown in Figure 3.2. It is assumed that the pressure in the subretinal space, p_1, is greater in magnitude
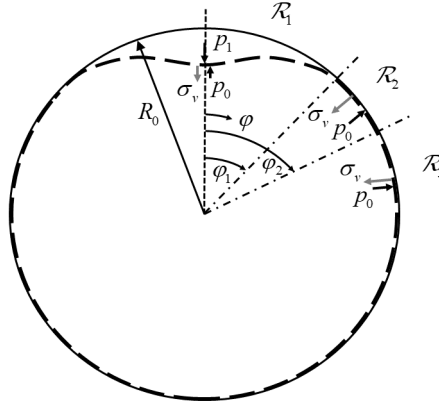
Figure 3.2: Schematic of the detaching retina in the emmetropic eye.

than the IOP, p_0, such that the pressure difference across the retina in the lift zone, p, acts in the direction of p_1 in Figure 3.2.

The problem is approached as a propagating boundary value problem in the calculus of variations, where the location of the boundary angle between the lift zone and contact zone,

φ_1, and between the contact zone and intact region, φ_2, are allowed to vary arbitrarily, as well as the elastic deflections of the detaching retina, $w_j(\varphi)$ and $u_j(\varphi)$. The potential energy functional, Π, for the ocular system reduces directly from the potential energy functional of the general shell in Eq. (2.117) of Chapter 2. For axisymmetric loading, the resultant in-plane shear force and resultant twisting moment shown in the elastic strain energy, U, of the general shell in Eq. (2.118) both vanish.

The work, $\mathcal{W}$, done by the ocular pressure difference across the retina and the applied stress from the vitreous fibrils replaces the general distributed loads given in Eq. (2.119). Hence, the work done on the retina takes the form,

$$\mathcal{W} = 2\pi R^2 \int_{\mathcal{R}_1} (p_1 - p_0 + \sigma_v) \, w_1 \sin \varphi \, \mathrm{d}\varphi + 2\pi R^2 \sum_{j=2}^{3} \int_{\mathcal{R}_j} (\sigma_v - p_0) \, w_j \sin \varphi \, \mathrm{d}\varphi \qquad (3.1)$$

In the constraint functional, Λ, given in Eq. (2.120), $\hat{\tau}_1^{(3)}$ is redefined here as $\hat{\tau}_3$ since $\hat{\tau}_2^{(3)}$ does not enter the formulation for axisymmetric loading and deformation. The formulation presented herein is the same as that of Bottega et $al.$ [12], but with the effects of the vitreous modeled through an applied stress from the vitreous fibrils, rather than as an elastic foundation.

The membrane forces and bending moments retain the form given in Eqs. (2.100) and (2.107), respectively. Hence,

$$N_{\varphi\varphi}^{(j)}(\varphi) = C\left[\varepsilon_{\varphi\varphi}^{(j)}(\varphi) + \nu\varepsilon_{\theta\theta}^{(j)}(\varphi)\right], \qquad N_{\theta\theta}^{(j)}(\varphi) = C\left[\varepsilon_{\theta\theta}^{(j)}(\varphi) + \nu\varepsilon_{\varphi\varphi}^{(j)}(\varphi)\right] \qquad (3.2)$$

$$M_{\varphi\varphi}^{(j)}(\varphi) = D\left[\chi_{\varphi\varphi}^{(j)}(\varphi) + \nu\chi_{\theta\theta}^{(j)}(\varphi)\right], \qquad M_{\theta\theta}^{(j)}(\varphi) = D\left[\chi_{\theta\theta}^{(j)}(\varphi) + \nu\chi_{\varphi\varphi}^{(j)}(\varphi)\right] \qquad (3.3)$$

where $C = Eh/\left(1 - \nu^2\right)$ is the membrane stiffness of the retina and $D = Ch^2/12$ is the corresponding bending stiffness of the retina. For thin spherical shells that are axisymmetric about $\varphi = 0$, Eqs. (2.86) and (2.88) for the strains and the bending measures in Region j $(j = 1 - 3)$ reduce to

$$\varepsilon_{\varphi\varphi}^{(j)}(\varphi) = \frac{1}{R}\left\{u_j'(\varphi) - w_j(\varphi)\right\}, \qquad \varepsilon_{\theta\theta}^{(j)}(\varphi) = \frac{1}{R}\left\{u_j(\varphi)\cot\varphi - w_j(\varphi)\right\} \qquad (3.4)$$

$$\chi_{\varphi\varphi}^{(j)}(\varphi) = \frac{1}{R^2}\left\{u_j'(\varphi) + w_j''(\varphi)\right\} = \frac{1}{R}\beta_\varphi^{(j)\prime}(\varphi),$$
$$\chi_{\theta\theta}^{(j)}(\varphi) = \frac{1}{R^2}\cot\varphi\left\{u_j(\varphi) + w_j'(\varphi)\right\} = \frac{1}{R}\cot\varphi\,\beta_\varphi^{(j)}(\varphi) \qquad (3.5)$$

where all derivatives are with respect to the coordinate φ. In Eqs. (3.5), β_φ is the component of the rotation vector with cross-section whose normal is tangent to the meridian direction of the retina. It is given directly by Eq. (2.87a) as

$$\beta_\varphi^{(j)}(\varphi) = \frac{1}{R}\left\{u_j(\varphi) + w_j'(\varphi)\right\} \tag{3.6}$$

For the axisymmetric deformation considered herein, the other components of the rotation vector in Eqs. (2.87b) and (2.87c), β_θ and β_ρ, vanish identically.

3.2.1 Equilibrium Equations

With Eqs. (2.117)-(2.121) reduced and interpreted with the parameters described above, the equations of equilibrium derived in Chapter 2, Eqs. (2.123) and (2.124), reduce to the following form for the emmetropic retina:

$$\left(Q_\varphi^{(j)}\sin\varphi\right)' - \left(N_{\varphi\varphi}^{(j)} + N_{\theta\theta}^{(j)}\right)\sin\varphi = \sigma_j R\sin\varphi \tag{3.7}$$

$$Q_\varphi^{(j)}\sin\varphi + \left(N_{\varphi\varphi}^{(j)}\sin\varphi\right)' - N_{\theta\theta}^{(j)}\cos\varphi = -\tau_j R\sin\varphi \tag{3.8}$$

$$\left(M_{\varphi\varphi}^{(j)}\sin\varphi\right)' - M_{\theta\theta}^{(j)}\cos\varphi = RQ_\varphi^{(j)}\sin\varphi \tag{3.9}$$

where the quantity $Q_\varphi^{(j)}(\varphi)$ is the resultant transverse shear force per unit length in region $\mathcal{R}_j$. In addition,

$$w_2(\varphi) = 0, \qquad u_3(\varphi) = w_3(\varphi) = 0 \tag{3.10}$$

In Eqs. (3.7)-(3.9), the parameters $\sigma_j(\varphi)$ and $\tau_j(\varphi)$ correspond to the radial normal stress and meridian shear stress, respectively, acting on the retina in Region $\mathcal{R}_j$. They are given in terms of the applied pressures, the stress from the vitreous fibrils, and the interfacial stresses (Lagrange multipliers) as

$$\sigma_j = \hat{\sigma}_j - p_0 + \sigma_v \tag{3.11}$$

where $\hat{\sigma}_1 = p_1$ and

$$\tau_1 = \tau_2 = 0, \qquad \tau_3 = \hat{\tau}_3 \tag{3.12}$$

The parameters $\hat{\sigma}_2(\varphi)$, $\hat{\sigma}_3(\varphi)$, and $\hat{\tau}_3(\varphi)$ are the Lagrange multipliers included in the formulation to insure continuity of displacements in the intact region and the contact zone.

These parameters can be evaluated as a function of the applied loading by substitution of the analytical solutions for the displacements into the pertinent equilibrium equation. The result correpsonds to the interfacial stresses acting between the retina and RPE in the contact zone and the intact region.

Substituting Eqs. (3.2)-(3.5) into the equations of equilibrium, Eqs. (3.7)-(3.9), yields a system of three equations with three unknowns: w_j, u_j, and $Q_\varphi^{(j)}$. In comparing Eqs. (3.7)-(3.9) to the equations of equilibrium of the general shell found in Section 2.5.2, it is clear that Eq. (3.7) is the simplified form of Eq. (2.123c). Similarly, Eq. (3.8) represents the simplified form of Eq. (2.123a) and Eq. (3.9) represents the simplified form of Eq. (2.124a).

3.2.2 Boundary Conditions

For shells with axisymmetric deformations, the boundary surfaces separating the lift zone, contact zone, and intact region are of a uniform value of φ for any given value of the coordinate θ. As such, the normal direction appearing in the boundary conditions of Section 2.5.4 is the φ direction and all boundary conditions applied in the tangential (θ) direction are satisfied identically by the axisymmetric nature of the deformation.

When *no retinal tear/hole* exists ($\varphi_0 = 0$), the conditions at $\varphi = 0$ are found to be

$$u_1(0) = 0, \quad \beta_\varphi^{(1)}(0) = 0, \quad Q_\varphi^{(1)}(0) = \left[\left(M_{\varphi\varphi}^{(1)}\sin\varphi\right)' - M_{\theta\theta}^{(1)}\cos\varphi\right]_{\varphi=0} = 0 \quad (3.13)$$

Alternatively, when a (*symmetric*) *retinal tear/hole* is present ($\varphi_0 > 0$), the boundary conditions at $\varphi = \varphi_0$ are

$$N_{\varphi\varphi}^{(1)}(\varphi_0) = 0, \quad M_{\varphi\varphi}^{(1)}(\varphi_0) = 0, \quad Q_\varphi^{(1)}(\varphi_0) = 0 \quad (3.14)$$

The remaining boundary conditions depend on the presence or absence of a contact zone (Region $\mathcal{R}_2$). While the model allows for a region of sliding contact, such a configuration of the structure is not necessarily physically realizable for a given detachment size and level of the applied loading. The transversality conditions, discussed below, establish the location of the boundary between the lifted region and the contact zone, and the location of the boundary of the detached region itself, that correspond to equilibrium configurations of the evolving ocular system. It follows that a contact zone will not be present if the transversality

condition for the contact zone boundary does not admit a physically realizable location of the contact zone boundary, for the given detachment size and load level.

When a contact zone is present, the boundary conditions at $\varphi = \varphi_1$ and $\varphi = \varphi_2$ are

$$u_1(\varphi_1) = u_2(\varphi_1), \qquad w_1(\varphi_1) = 0, \qquad \beta_\varphi^{(1)}(\varphi_1) = 0,$$
$$N_{\varphi\varphi}^{(1)}(\varphi_1) = N_{\varphi\varphi}^{(2)}(\varphi_1), \qquad u_2(\varphi_2) = 0 \tag{3.15}$$

When a contact zone is absent $(\varphi_1 = \varphi_2)$, Region $\mathcal{R}_2$ does not exist and Region $\mathcal{R}_1$ constitutes the entire detached area. For this case, the boundary conditions of Eq. (3.15) are superfluous and, hence, the boundary conditions at $\varphi = \varphi_2$ are

$$u_1(\varphi_2) = 0, \qquad w_1(\varphi_2) = 0, \qquad \beta_\varphi^{(1)}(\varphi_2) = 0 \tag{3.16}$$

3.2.3   Transversality Conditions

The boundaries of the detached area and of the contact zone are not fixed. Rather, they are found as part of the solution to the problem. Allowing these parameters to vary arbitrarily when performing the variations yields the *transversality conditions* that establish the location of the propagating boundaries φ_2 and φ_1 that correspond to equilibrium configurations of the evolving ocular system. Two possibilities are considered: (i) a contact zone is present and (ii) a contact zone is absent.

(i) *When a contact zone is present*, and when considering axisymmetic deformation and detachment of the spherical retina, the transversality conditions for the general shell in Eqs. (2.136)-(2.138) reduce to the following form:

$$\left[\mathcal{H}_\varphi^{(1)} - \mathcal{F}_\varphi^{(1)} \right]_{\varphi=\varphi_1} = \left[\mathcal{H}_\varphi^{(2)} - \mathcal{F}_\varphi^{(2)} \right]_{\varphi=\varphi_1} \tag{3.17}$$

where

$$\mathcal{F}_\varphi^{(j)} = \frac{1}{2} \left[N_{\varphi\varphi}^{(j)} \varepsilon_{\varphi\varphi}^{(j)} + N_{\theta\theta}^{(j)} \varepsilon_{\theta\theta}^{(j)} + M_{\varphi\varphi}^{(j)} \chi_{\varphi\varphi}^{(j)} + M_{\theta\theta}^{(j)} \chi_{\theta\theta}^{(j)} \right] \tag{3.18}$$

and

$$\mathcal{H}_\varphi^{(j)} = \frac{1}{R} \left[N_{\varphi\varphi}^{(j)} \frac{\partial u_j}{\partial \varphi} - Q_\varphi^{(j)} \frac{\partial w_j}{\partial \varphi} + M_{\varphi\varphi}^{(j)} \frac{\partial \beta_\varphi^{(j)}}{\partial \varphi} \right] \tag{3.19}$$

Upon incorporation of Eq. $(3.10)_1$ and the pertinent boundary conditions, Eq. (3.17) which establishes the contact zone boundary, $\varphi = \varphi_1$, further reduces to

$$w_1''(\varphi_1) = 0 \tag{3.20}$$

to which the following qualification applies

$$w_1'' \left(\varphi_1^- \right) > 0 \tag{3.21}$$

to rule out penetration[1].

In addition, Eq. (2.139) which establishes the location of the propagating detachment boundary, φ_2, takes the form

$$\mathcal{G} \left\{ \varphi_2 \right\} = \left[\mathcal{H}_\varphi^{(2)} - \mathcal{F}_\varphi^{(2)} \right]_{\varphi = \varphi_2} = 2\gamma \tag{3.22}$$

which upon incorporation of Eq. $(3.10)_1$ and the pertinent boundary conditions, reduces to

$$\mathcal{G} \left\{ \varphi_2 \right\} = \frac{1}{2R^2} \left[\left(\frac{D}{R^2} + C \right) u_2'^2 \right]_{\varphi = \varphi_2} = 2\gamma \tag{3.23}$$

where the function $\mathcal{G} \left\{ \varphi_2 \right\}$ is identified as the *energy release rate* (energy released per unit increase of detachment angle) of the detaching ocular system and γ is the energy required to produce a unit area of detachment (a property of the particular interface and retinal materials).

(ii) If, for a given detachment angle and level of the applied loading, Eq. (3.20) fails to yield a physically realizable value for the contact zone boundary, then a *contact zone is absent* ($\varphi_1 = \varphi_2$). In this case, Eq. (3.23) is superfluous and the transversality condition that establishes the detachment boundary, $\varphi = \varphi_2$, is given by

$$\mathcal{G} \left\{ \varphi_2 \right\} = \frac{1}{2R^2} \left[\frac{D}{R^2} \left(u_1' + w_1'' \right)^2 + C u_1'^2 \right]_{\varphi = \varphi_2} = 2\gamma \tag{3.24}$$

Equations (3.23) and (3.24) suggest the following Griffith-type criterion for detachment propagation (Griffith [32]); If $\mathcal{G} \left\{ \varphi^* \right\} \geq 2\gamma$ for some initial value, φ^*, of the detachment angle, φ_2, propagation of the detachment will occur with the detachment boundary angle, φ_2, increasing until the equality is satisfied. If $\mathcal{G} \left\{ \varphi^* \right\} < 2\gamma$, propagation will not occur. Equation (3.24) corresponds to Eq. (2.140) for the transversality condition governing the propagating detachment boundary of the general shell with no contact zone.

---

[1]In Eq. (3.21), the quantity φ_1^- indicates a value of φ infinitesimally close to, but less than, φ_1.

3.2.4 Non-dimensionalization

Thus far, all of the parameters presented have been given in dimensional form. In obtaining solutions to the governing equations and in presenting results, all of these parameters will be given in non-dimensional form. Non-dimensional parameters are henceforth signified by an overbar. Length scales are non-dimensionalized with respect to the nominal value of the radius of the emmetropic retina, R_0, as follows;

$$\bar{R} = R/R_0, \quad \bar{w} = w/R_0, \quad \bar{u} = u/R_0, \quad \bar{h} = h/R_0 \tag{3.25}$$

Biological materials present a large variability in the measurement of their mechanical properties. Hence, the remaining parameters are non-dimensionalized with respect to the bending stiffness of the retina at a reference value, D_0, which is given in terms of the Young's modulus of the retina at a nominal reference value, E_0. The nominal values for the reference radius R_0 and the reference Young's modulus E_0 are discussed in Section 3.4. The non-dimensional stiffnesses then take the following forms

$$\bar{D} = D/D_0 = E/E_0 \quad \text{and} \quad \bar{C} = CR_0^2/D_0 = 12\bar{D}/\bar{h}^2 \tag{3.26}$$

respectively. In this manner, the effects of variability in the measurement of the Young's modulus of the retina on the results of the detachment model can be investigated by varying the parameter $\bar{D}$. Similarly, the effects of the radius of the retina on the detachment behavior can be investigated by varying $\bar{R}$. Other non-dimensional parameters include

$$\bar{\sigma} = \sigma R_0^3/D_0, \quad \bar{\tau} = \tau R_0^3/D_0, \quad \bar{\gamma} = \gamma R_0^2/D_0, \quad \bar{Q}_\varphi = Q_\varphi R_0^2/D_0,$$

$$\bar{N}_{\varphi\varphi} = N_{\varphi\varphi} R_0^2/D_0, \quad \bar{N}_{\theta\theta} = N_{\theta\theta} R_0^2/D_0, \quad \bar{M}_{\varphi\varphi} = M_{\varphi\varphi} R_0/D_0, \quad \bar{M}_{\theta\theta} = M_{\theta\theta} R_0/D_0 \tag{3.27}$$

whose interpretations follow accordingly. The general solution for the mathematical model of retinal detachment in emmetropic eyes is presented in the next section.

3.3 Solution

In Bottega *et al.* [12], the meridian displacements were neglected in the solution to the equations of equilibrium derived therein in order to simplify the equations and obtain a

closed form solution for the transverse deflection. In this section, the meridian displacements are retained in Eqs. (3.7)-(3.9) and an exact analytical solution for an emmetropic detaching retina is presented. Solutions are obtained for the case when a retinal tear is present as well as for the case when it is absent.

The equations of equilibrium, Eqs. (3.7)-(3.9), are written in non-dimensional form to facilitate the solution procedure. The following equations are applicable to Region $\mathcal{R}_1$ since it is the only region that has both radial and meridian displacements and, hence, will be the focus of the solution procedure.

$$\left(\bar{Q}_\varphi^{(1)} \sin \varphi\right)' - \left(\bar{N}_{\varphi\varphi}^{(1)} + \bar{N}_{\theta\theta}^{(1)}\right) \sin \varphi = \bar{\sigma}_1 \bar{R} \sin \varphi \tag{3.28}$$

$$\bar{Q}_\varphi^{(1)} \sin \varphi + \left(\bar{N}_{\varphi\varphi}^{(1)} \sin \varphi\right)' - \bar{N}_{\theta\theta}^{(1)} \cos \varphi = 0 \tag{3.29}$$

$$\left(\bar{M}_{\varphi\varphi}^{(1)} \sin \varphi\right)' - \bar{M}_{\theta\theta}^{(1)} \cos \varphi = \bar{R}\bar{Q}_\varphi^{(1)} \sin \varphi \tag{3.30}$$

In order to solve the system of coupled differential equations given by Eqs. (3.28)-(3.30), a change of variables is introduced that will allow for a reduction of the fourth order coupled equations of equilibrium to two second order differential equations of a single variable. This method is motivated by similar procedures found in Timoshenko & Woinowsky-Krieger [76] and Flügge [21] for shells having the form of a surface of revolution and loaded symmetrically with respect to their axis. The non-dimensional form of the transverse shear force, $\bar{Q}_\varphi^{(1)}$ as defined in Eq. (3.30), is retained as one of the independent variables and the angle of rotation of a tangent to the meridian of the retina, $\beta_\varphi^{(1)}$ as defined in Eq. (3.6), is introduced as the other independent variable. When non-dimensionalized, the angle of rotation takes the form

$$\beta_\varphi^{(1)} = \frac{1}{\bar{R}} \left\{\bar{u}_1 + \bar{w}_1'\right\} \tag{3.31}$$

First, the straightforward step of expressing Eq. (3.30) in terms of these variables through substitution of Eqs. (3.3) and (3.5) results in

$$\frac{\bar{D}}{\bar{R}^2} \left[\beta_\varphi^{(1)''} + \cot\varphi\beta_\varphi^{(1)'} - \left(\nu + \cot^2\varphi\right)\beta_\varphi^{(1)}\right] = \bar{Q}_\varphi^{(1)} \tag{3.32}$$

In order to combine the equations of equilibrium given by Eqs. (3.28) and (3.29), it is necessary to rewrite the constitutive equations, Eqs. (3.2), in the following non-dimensional

forms:

$$\bar{u}_1' - \bar{w}_1 = \frac{\bar{R}}{\bar{C}\left(1 - \nu^2\right)}\left(\bar{N}_{\varphi\varphi}^{(1)} - \nu\bar{N}_{\theta\theta}^{(1)}\right) \tag{3.33}$$

and

$$\bar{u}_1\cot\varphi - \bar{w}_1 = \frac{\bar{R}}{\bar{C}\left(1 - \nu^2\right)}\left(\bar{N}_{\theta\theta}^{(1)} - \nu\bar{N}_{\varphi\varphi}^{(1)}\right) \tag{3.34}$$

Subtracting Eq. (3.34) from Eq. (3.33) will eliminate $\bar{w}_1$ and yield

$$\bar{u}_1' - \bar{u}_1\cot\varphi = \frac{\bar{R}}{\bar{C}\left(1 - \nu\right)}\left(\bar{N}_{\varphi\varphi}^{(1)} - \bar{N}_{\theta\theta}^{(1)}\right) \tag{3.35}$$

Now, subtracting the derivative of Eq. (3.34) from the product of Eq. (3.35) and $\cot\varphi$ leads to

$$\frac{\bar{R}}{\bar{C}\left(1 - \nu^2\right)}\left[\left(1 + \nu\right)\left(\bar{N}_{\varphi\varphi}^{(1)} - \bar{N}_{\theta\theta}^{(1)}\right)\cot\varphi - \left(\bar{N}_{\theta\theta}^{(1)} - \nu\bar{N}_{\varphi\varphi}^{(1)}\right)'\right] = \bar{u}_1 + \bar{w}_1' \tag{3.36}$$

Finally, substituting Eq. (3.29) into Eq. (3.36), followed by the substitution of the derivative of Eq. (3.28) into the resulting expression, leads to

$$\bar{Q}_{\varphi}^{(1)''} + \cot\varphi\bar{Q}_{\varphi}^{(1)'} + \left(\nu - \cot^2\varphi\right)\bar{Q}_{\varphi}^{(1)} = -\bar{C}\left(1 - \nu^2\right)\beta_{\varphi}^{(1)} \tag{3.37}$$

At this point the equations of equilibrium have been reduced from three equations in three variables to two equations in two variables. Now, recognizing the similar form of Eqs. (3.32) and (3.37), it is useful to define the mathematical operator

$$L(\cdot) = (\cdot)'' + \cot\varphi(\cdot)' - \cot^2(\cdot) \tag{3.38}$$

Thus, Eqs. (3.32) and (3.37) are rewritten in the following form:

$$L\left(\beta_{\varphi}^{(1)}\right) - \nu\beta_{\varphi}^{(1)} = \frac{\bar{D}}{\bar{R}^2}\bar{Q}_{\varphi}^{(1)} \tag{3.39}$$

$$L\left(\bar{Q}_{\varphi}^{(1)}\right) + \nu\bar{Q}_{\varphi}^{(1)} = -\bar{C}\left(1 - \nu^2\right)\beta_{\varphi}^{(1)} \tag{3.40}$$

The operator $L(\cdot)$ is now applied to Eqs. (3.39) and (3.40), which gives

$$LL\left(\beta_{\varphi}^{(1)}\right) - \nu L\left(\beta_{\varphi}^{(1)}\right) = \frac{\bar{D}}{\bar{R}^2}L\left(\bar{Q}_{\varphi}^{(1)}\right) \tag{3.41}$$

$$LL\left(\bar{Q}_{\varphi}^{(1)}\right) + \nu L\left(\bar{Q}_{\varphi}^{(1)}\right) = -\bar{C}\left(1 - \nu^2\right)L\left(\beta_{\varphi}^{(1)}\right) \tag{3.42}$$

The relations given in Eqs. (3.39) and (3.40) are next used to decouple Eqs. (3.41) and (3.42) into a single differential equation in $\beta_{\varphi}^{(1)}$ and another in $\bar{Q}_{\varphi}^{(1)}$. The resulting equations take the forms

$$LL\left(\bar{Q}_{\varphi}^{(1)}\right) + \left[\frac{\bar{R}^2\bar{C}}{\bar{D}}\left(1 - \nu^2\right) - \nu^2\right]\bar{Q}_{\varphi}^{(1)} = 0 \tag{3.43}$$

and

$$LL\left(\beta_\varphi^{(1)}\right) + \left[\frac{\bar{R}^2\bar{C}}{\bar{D}}\left(1-\nu^2\right) - \nu^2\right]\beta_\varphi^{(1)} = 0 \tag{3.44}$$

It is clear that Eqs. (3.43) and (3.44) are of identical form. As a result, it is only necessary to solve Eq. (3.43) to obtain a solution for the general form of the expression for $\bar{Q}_\varphi^{(1)}$. The expression for $\beta_\varphi^{(1)}$ is then readily found from Eq. (3.40). Upon closer examination, it is seen that Eq. (3.43) can be rewritten in either of the two following forms:

$$L\left[L\left(\bar{Q}_\varphi^{(1)}\right) + i\tfrac{1}{4}Z\bar{Q}_\varphi^{(1)}\right] - i\tfrac{1}{4}Z\left[L\left(\bar{Q}_\varphi^{(1)}\right) + i\tfrac{1}{4}Z\bar{Q}_\varphi^{(1)}\right] = 0 \tag{3.45}$$

or

$$L\left[L\left(\bar{Q}_\varphi^{(1)}\right) - i\tfrac{1}{4}Z\bar{Q}_\varphi^{(1)}\right] + i\tfrac{1}{4}Z\left[L\left(\bar{Q}_\varphi^{(1)}\right) - i\tfrac{1}{4}Z\bar{Q}_\varphi^{(1)}\right] = 0 \tag{3.46}$$

where i is the imaginary unit $\left(\sqrt{-1}\right)$ and

$$Z = 4\sqrt{\frac{\bar{R}^2\bar{C}}{\bar{D}}\left(1-\nu^2\right) - \nu^2} \tag{3.47}$$

Finally, Eqs. (3.45) and (3.46) are written as

$$L\left(\bar{Q}_\varphi^{(1)}\right) \pm i\tfrac{1}{4}Z\bar{Q}_\varphi^{(1)} = 0 \tag{3.48}$$

The linear combination of the solutions to the two second-order differential equations represented by Eq. (3.48) will satisfy the fourth-order differential equation given in Eq. (3.43). This linear combination will also form the final solution for the general form of $\bar{Q}_\varphi^{(1)}$, which is given as

$$\bar{Q}_\varphi^{(1)}(\varphi) = A_1 \sin\varphi\,_2F_1\left(\psi_a, \psi_b; 2; \sin^2\varphi\right) + A_2 \sin\varphi\,_2F_1\left(\hat{\psi}_a, \hat{\psi}_b; 2; \sin^2\varphi\right)$$
$$+ A_3 \sin\varphi\, G_{2,2}^{2,0}\left(\sin^2\varphi\,\middle|\,\begin{matrix}\psi_a - \tfrac{1}{2}, \psi_b - \tfrac{1}{2}\\ -1, 0\end{matrix}\right) + A_4 \sin\varphi\, G_{2,2}^{2,0}\left(\sin^2\varphi\,\middle|\,\begin{matrix}\hat{\psi}_a - \tfrac{1}{2}, \hat{\psi}_b - \tfrac{1}{2}\\ -1, 0\end{matrix}\right) \tag{3.49}$$

where

$$\psi_a = \frac{3 + \sqrt{5 + iZ}}{4}, \qquad \psi_b = \frac{3 - \sqrt{5 + iZ}}{4}, \qquad \hat{\psi}_a = \frac{3 + \sqrt{5 - iZ}}{4}, \qquad \hat{\psi}_b = \frac{3 - \sqrt{5 - iZ}}{4} \tag{3.50}$$

In addition, $_2F_1(\cdot)$ represents a Hypergeometric function, $G_{2,2}^{2,0}(\cdot)$ represents a Meijer G function, and A_1-A_4 are constants of integration. In order to apply the boundary conditions given in Eqs. (3.13)-(3.16) to solve for the constants of integration in Eq. (3.49), the functions

$\bar{w}_1$ and $\bar{u}_1$ must be expressed in terms of the function $\bar{Q}_\varphi^{(1)}$. This procedure begins with consideration of Eq. (3.28), which follows as

$$\bar{N}_{\varphi\varphi}^{(1)} + \bar{N}_{\theta\theta}^{(1)} = \bar{Q}_\varphi^{(1)'} + \bar{Q}_\varphi^{(1)} \cot\varphi - \bar{R}\bar{\sigma}_1 \tag{3.51}$$

This is followed by the combination of Eq. (3.29) and Eq. (3.51), which results in

$$2\bar{N}_{\varphi\varphi}^{(1)} + \bar{N}_{\varphi\varphi}^{(1)'} \tan\varphi = \bar{Q}_\varphi^{(1)'} + \bar{Q}_\varphi^{(1)} (\cot\varphi - \tan\varphi) - \bar{R}\bar{\sigma}_1 \tag{3.52}$$

This is integrated to obtain the expression for $\bar{N}_{\varphi\varphi}^{(1)}$ in terms of $\bar{Q}_\varphi^{(1)}$. Subsequently, substituting that expression into Eq. (3.51) yields the expression for $\bar{N}_{\theta\theta}^{(1)}$ in terms of $\bar{Q}_\varphi^{(1)}$. The expressions for the membrane forces in Region $\mathcal{R}_1$ are then

$$\bar{N}_{\varphi\varphi}^{(1)} = \bar{Q}_\varphi^{(1)} \cot\varphi + \tfrac{1}{2}\bar{R}\bar{\sigma}_1 \cot^2\varphi + A_5 \csc^2\varphi \tag{3.53}$$

$$\bar{N}_{\theta\theta}^{(1)} = \bar{Q}_\varphi^{(1)'} - \tfrac{1}{2}\bar{R}\bar{\sigma}_1 \left(\csc^2\varphi + 1\right) - A_5 \csc^2\varphi \tag{3.54}$$

where A_5 is a constant of integration.

In order to obtain an expression for the meridian displacement, Eqs. (3.53) and (3.54) are first substituted into Eq. (3.35). The resulting equation is then integrated to obtain

$$\bar{u}_1(\varphi) = A_6 \sin\varphi - \frac{\bar{R}}{\bar{C}(1-\nu)} \left[\bar{Q}_\varphi^{(1)} + \left(\frac{1}{2}\bar{R}\bar{\sigma}_1 + A_5\right) \left(\cot\varphi + \sin\varphi \ln\left\{\cot\frac{\varphi}{2}\right\}\right) \right] \tag{3.55}$$

where A_6 is a constant of integration.

To obtain an expression for the radial displacement, Eqs. (3.53)-(3.55) are substituted into Eq. (3.34) to obtain

$$\begin{aligned}
\bar{w}_1(\varphi) = {} & A_6 \cos\varphi + A_5 \frac{\bar{R}}{\bar{C}(1-\nu)} \left[1 - \cos\varphi \ln\left\{\cot\frac{\varphi}{2}\right\}\right] \\
& - \frac{\bar{R}}{\bar{C}(1-\nu^2)} \left[\bar{Q}_\varphi^{(1)'} + \bar{Q}_\varphi^{(1)} \cot\varphi\right] + \frac{\bar{R}^2\bar{\sigma}_1}{\bar{C}(1-\nu^2)} \left[1 - \frac{1}{2}(1+\nu)\cos\varphi \ln\left\{\cot\frac{\varphi}{2}\right\}\right]
\end{aligned} \tag{3.56}$$

With the expressions for the meridian and radial displacements established, Eqs. (3.55) and (3.56), respectively, it is now possible to solve for the constants of integration.

First, consideration is given to the case of a retina with no tear and then consideration is given to the case of a retina with a central tear/hole present. At this point, the boundary conditions in Eq. (3.15) or those of Eq. (3.16) are applied, depending upon the existence, or absence, of a contact zone, Region $\mathcal{R}_2$. In the ensuing analysis, both the situation of a

tear and that of no tear is considered. However, when applying Eq. (3.15) for an existing contact zone, it is found that the transversality condition given in Eq. (3.20) is not satisfied for any values of the boundary angles φ_1 and φ_2 for either case. This is done by plotting $\bar{w}_1''(\varphi)$ over the range of angle φ_1 for various values of angle φ_2. Upon doing this, it is observed that $\bar{w}_1''(\varphi_1)$ does not vanish for any combination of these boundary angles. The corresponding plots are omitted for brevity. Therefore, it is concluded that a contact zone will not exist for either the case of a tear or that of no tear, for the range of detachment sizes considered. As a result, Eq. (3.16) is used in the remainder of the solution procedure.

3.3.1   Case 1: No Retinal Tear

For the case when there is no retinal tear, the domain of definition of the detached segment of the retina is $\varphi \in [0, \varphi_2]$. The Meijer G function, as well as the cotangent function and natural logarithm, are singular at the origin, but it is required on physical grounds that the deflections be finite at the origin and throughout the domain of definition. The condition of finite deflection at the origin is then the 'boundary condition' at $\varphi = 0$, and replaces the three conditions of Eq. (3.13). As a result, the integration constants in Eqs. (3.55) and (3.56) are found to be

$$A_3 = 0, \quad A_4 = 0, \quad A_5 = -\frac{1}{2}\bar{R}\bar{\sigma}_1 \tag{3.57}$$

Imposing the other pertinent boundary conditions, as specified in Eq. (3.16), gives the remaining integration constants, A_1, A_2, and A_6, as

$$\left\{ \begin{array}{c} A_1 \\ A_2 \\ A_6 \end{array} \right\} = [\lambda_1]^{-1} \left\{ \begin{array}{c} \frac{1}{2}\bar{R}\bar{\sigma}_1(1-\nu) \\ 0 \\ 0 \end{array} \right\} \tag{3.58}$$

where

$$[\lambda_1] = \begin{bmatrix} \cos\varphi_2 X_1(\psi_a, \psi_b, \varphi_2) & \cos\varphi_2 X_1(\hat{\psi}_a, \hat{\psi}_b, \varphi_2) & -\frac{\bar{C}}{R}\cos\varphi_2(1-\nu^2) \\ X_2(\psi_a, \psi_b, \varphi_2) & X_2(\hat{\psi}_a, \hat{\psi}_b, \varphi_2) & -\frac{\bar{C}}{R}(1-\nu^2) \\ {}_2F_1(\psi_a, \psi_b; 2; \sin^2\varphi_2) & {}_2F_1(\hat{\psi}_a, \hat{\psi}_b; 2; \sin^2\varphi_2) & -\frac{\bar{C}}{R}(1-\nu) \end{bmatrix} \tag{3.59}$$

$$X_1(\psi_a, \psi_b, \varphi) = 2\,{}_2F_1(\psi_a, \psi_b; 2; \sin^2\varphi) + \psi_a\psi_b\sin^2\varphi\,{}_2F_1(\psi_a+1, \psi_b+1; 3; \sin^2\varphi) \tag{3.60}$$

$$X_2\left(\psi_a, \psi_b, \varphi\right) = 2\,{}_2F_1\left(\psi_a, \psi_b; 2; \sin^2 \varphi\right) + \left(1 - 5\cos^2 \varphi\right)\psi_a\psi_b\,{}_2F_1\left(\psi_a + 1, \psi_b + 1; 3; \sin^2 \varphi\right)$$

$$- \tfrac{2}{3}\sin^2 \varphi \cos^2 \varphi \psi_a\psi_b\left(\psi_a + 1\right)\left(\psi_b + 1\right){}_2F_1\left(\psi_a + 2, \psi_b + 2; 4; \sin^2 \varphi\right)$$

$$\tag{3.61}$$

3.3.2 Case 2: Retinal Tear/Hole Present

Next, the case where a retinal tear/hole of meridian angle φ_0 exists at the center of the detached region is considered. In this case, the domain of definition of the detached segment of the retina is $\varphi \in [\varphi_0, \varphi_2]$. Imposing the pertinent boundary conditions, Eqs. (3.14) and (3.16), yields the integration constants A_1-A_6 as

$$\begin{Bmatrix} A_1 \\ A_2 \\ A_3 \\ A_4 \\ A_5 \\ A_6 \end{Bmatrix} = [\lambda_2]^{-1} \begin{Bmatrix} \bar{R}\bar{\sigma}_1\left[\sec\varphi_2 - \tfrac{1}{2}\left(1 + \nu\right)g\left(\varphi_2\right)\right] \\ -\tfrac{1}{2}\bar{R}\bar{\sigma}_1\left(1 + \nu\right)\hat{g}\left(\varphi_2\right) \\ -\tfrac{1}{2}\bar{R}\bar{\sigma}_1\hat{g}\left(\varphi_2\right) \\ 0 \\ -\tfrac{1}{2}\bar{R}\bar{\sigma}_1\cot\varphi_0\csc\varphi_0 \\ 0 \end{Bmatrix} \tag{3.62}$$

where

$$[\lambda_2] = \begin{bmatrix} X_1\left(\psi_a, \psi_b, \varphi_2\right) & X_1\left(\hat{\psi}_a, \hat{\psi}_b, \varphi_2\right) & Y_1\left(\psi_a, \psi_b, \varphi_2\right) & Y_1\left(\hat{\psi}_a, \hat{\psi}_b, \varphi_2\right) & -\tilde{g}\left(\varphi_2\right) & -\tfrac{\bar{C}}{R}\left(1 - \nu^2\right) \\ X_2\left(\psi_a, \psi_b, \varphi_2\right) & X_2\left(\hat{\psi}_a, \hat{\psi}_b, \varphi_2\right) & Y_2\left(\psi_a, \psi_b, \varphi_2\right) & Y_2\left(\hat{\psi}_a, \hat{\psi}_b, \varphi_2\right) & \left(1 + \nu\right)\hat{g}\left(\varphi_2\right) & -\tfrac{\bar{C}}{R}\left(1 - \nu^2\right) \\ F\left(\psi_a, \psi_b, \varphi_2\right) & F\left(\hat{\psi}_a, \hat{\psi}_b, \varphi_2\right) & G\left(\psi_a, \psi_b, \varphi_2\right) & G\left(\hat{\psi}_a, \hat{\psi}_b, \varphi_2\right) & \hat{g}\left(\varphi_2\right) & -\tfrac{\bar{C}}{R}\left(1 - \nu\right) \\ F\left(\psi_a, \psi_b, \varphi_0\right) & F\left(\hat{\psi}_a, \hat{\psi}_b, \varphi_0\right) & G\left(\psi_a, \psi_b, \varphi_0\right) & G\left(\hat{\psi}_a, \hat{\psi}_b, \varphi_0\right) & 0 & 0 \\ F\left(\psi_a, \psi_b, \varphi_0\right) & F\left(\hat{\psi}_a, \hat{\psi}_b, \varphi_0\right) & G\left(\psi_a, \psi_b, \varphi_0\right) & G\left(\hat{\psi}_a, \hat{\psi}_b, \varphi_0\right) & \sec\varphi_0\csc^2\varphi_0 & 0 \\ X_3\left(\psi_a, \psi_b, \varphi_0\right) & X_3\left(\hat{\psi}_a, \hat{\psi}_b, \varphi_0\right) & Y_3\left(\psi_a, \psi_b, \varphi_0\right) & Y_3\left(\hat{\psi}_a, \hat{\psi}_b, \varphi_0\right) & 0 & 0 \end{bmatrix}$$

$$\tag{3.63}$$

$$F\left(\psi_a, \psi_b, \varphi\right) = {}_2F_1\left(\psi_a, \psi_b; 2; \sin^2 \varphi\right) \tag{3.64}$$

$$G\left(\psi_a, \psi_b, \varphi\right) = G_{2,2}^{2,0}\left(\sin^2 \varphi \,\middle|\, \begin{matrix} \psi_a - \tfrac{1}{2}, \psi_b - \tfrac{1}{2} \\ -1, 0 \end{matrix}\right) \tag{3.65}$$

$$Y_1\left(\psi_a, \psi_b, \varphi\right) = 2G\left(\psi_a, \psi_b, \varphi\right) + \tan\varphi G'\left(\psi_a, \psi_b, \varphi\right) \tag{3.66}$$

$$Y_2\left(\psi_a, \psi_b, \varphi\right) = 2G\left(\psi_a, \psi_b, \varphi\right) - 3\cot\varphi G'\left(\psi_a, \psi_b, \varphi\right) - G''\left(\psi_a, \psi_b, \varphi\right) \tag{3.67}$$

$$X_3\left(\psi_a, \psi_b, \varphi\right) = \left(1 - \nu^2\right){}_2F_1\left(\psi_a, \psi_b; 2; \sin^2\varphi\right)$$

$$+ \left(16\sin^2\varphi - 4\nu\cos^2\varphi - 4\right)\psi_a\psi_b\,{}_2F_1\left(\psi_a + 1, \psi_b + 1; 3; \sin^2\varphi\right)$$

$$- \tfrac{2}{3}\sin^2\varphi\left[(10 + \nu)\cos^2\varphi - 3\right]\psi_a\psi_b\left(\psi_a + 1\right)\left(\psi_b + 1\right){}_2F_1\left(\psi_a + 2, \psi_b + 2; 4; \sin^2\varphi\right)$$

$$- \tfrac{1}{3}\sin^4\varphi\cos^2\varphi\psi_a\psi_b\left(\psi_a + 1\right)\left(\psi_b + 1\right)\left(\psi_a + 2\right)\left(\psi_b + 2\right){}_2F_1\left(\psi_a + 3, \psi_b + 3; 5; \sin^2\varphi\right)$$

$$(3.68)$$

$$Y_3\left(\psi_a, \psi_b, \varphi\right) = \left(1 - \nu^2\right)G\left(\psi_a, \psi_b, \varphi\right) + \left[(4 - \nu)\tan\varphi - 3\nu\cot\varphi\right]G'\left(\psi_a, \psi_b, \varphi\right)$$

$$- (4 + \nu)\,G''\left(\psi_a, \psi_b, \varphi\right) - \tan\varphi\,G'''\left(\psi_a, \psi_b, \varphi\right)$$

$$(3.69)$$

$$g\left(\varphi\right) = \ln\left\{\cot\frac{\varphi}{2}\right\}, \qquad \hat{g}\left(\varphi\right) = \cot\varphi\csc\varphi + g\left(\varphi\right), \qquad \tilde{g}\left(\varphi\right) = (1 + \nu)\left[\sec\varphi - g\left(\varphi\right)\right] \quad (3.70)$$

The solutions obtained in this section are used to perform simulations of the evolution of retinal detachment in the emmetropic eye, the results of which are presented in Section 3.5.

3.4 Material Properties

The radius of the emmetropic retina in a human eye with average dimensions is given as $R_0 = 11$ mm in Wilkinson & Rice [84]. Wilkinson & Rice also give measurements for the thickness of the retina, which varies based on the location within the eye. At the periphery the thickness is given as $h = 0.1$ mm, while at the midperiphery the thickness is $h = 0.14$ mm and at the posterior of the eye the thickness is $h = 0.23$ mm.

The ora serrata and the optic nervehead are regions of strong retinal attachment from which the retina cannot detach and the location of each is also given in Wilkinson and Rice [84]. The retina ends anteriorly at the ora serrata which is located approximately 4.8 mm anterior to the center of the eye. The edge of the optic nervehead is approximately 3.4 mm nasal to the posterior pole and aligned horizontally with the posterior pole.

The Young's modulus employed in the present study is taken from data in Wollensak *et al.* [85], in which *in vitro* tensile tests were performed on retinal strips taken from post-mortem human eyes. From the data provided in Wollensak *et al.* [85], the Young's modulus of the human retina is calculated here to be $E_0 = (4.65 \pm 0.93)\cdot 10^4$ Pa based on the reported force-elongation measurements and the given sample dimensions.

Chen *et al.* [15] took *in vitro* measurements of the (tangent) elastic modulus and thickness of the retina, choroid, and sclera from human eyes in 37°C saline. The ratio of the

corresponding membrane stiffness of the retina, C, to that of the choroid, C_{chor}, is found to be $C/C_{chor} \sim O(10^{-2})$, while the ratio of the retina to that of the sclera, C_{scl}, is found to be $10^{-4} < C/C_{scl} < 10^{-3}$. The ratios of the bending stiffness of the retina, D, to the bending stiffness of the choroid, D_{chor}, and that of the retina to that of the sclera, D_{scl}, are found to be $D/D_{chor} \sim O(10^{-2})$ and $10^{-5} < D/D_{scl} < 10^{-4}$, respectively. Hence, modeling the retina as a thin elastic shell detaching from a rigid RPE-choroid-sclera composite structure is justified. Similar justification was provided in Bottega *et al.* [12] based upon the material properties of porcine ocular tissues provided in Chen *et al.* [14].

3.5   Results

In this section, the results of simulations based on the analytical solutions presented in Section 3.3 are presented for the case of a pre-existing retinal tear as well as for the case when no tear is present. The results of this study are compared to the corresponding results found by Bottega *et al.* [12] in order to assess the influence of the meridian displacements on the detachment process.

In order to compare the results of this study to those of Bottega *et al.* [12], the loading parameter that represents the contraction of the vitreous in the separate studies must be reconciled. Here, the stress from the vitreous fibrils is identified by the parameter σ_v, which appears in the transverse loading acting on the retina given in Eq. (3.11). In Bottega *et al.* [12], the vitreous and its fibrils are modeled as a pre-tensioned elastic foundation of stiffness k per unit area that is initially extended a radial distance, w_0, due to the contraction of the vitreous. Later, Bottega *et al.* [12] makes the assumption that the parameter the authors called η, a scaled ratio of the fibril stiffness to the membrane stiffness, is very small when compared with one. This assumption was applied in their study when performing numerical simulations of the results in all cases, with the exception of a parameter study on η. Physically this assumption considers the vitreous fibrils to be much more compliant in the radial direction than the retina is along the meridian direction. In this study, modeling the stress from the vitreous fibrils as

$$\sigma_v = kw_0 \tag{3.71}$$

is equivalent to the elastic foundation modeled by Bottega *et al.* [12] with the parameter $\eta \ll 1$. Physically this corresponds to modeling the stress from the vitreous fibrils as an elastic foundation, while neglecting the reduction in magnitude of the spring force as the retina detaches and the extended vitreous fibrils relax.

Based on the linear nature of the governing equations, it is evident that the normalized displacement fields given by Eqs. (3.55) and (3.56) will be proportional to $\bar{\sigma}_1$. Hence, these displacements fields can be written in the general form

$$\bar{u}_1\left(\varphi\right) = \bar{\sigma}_1 \bar{U}_1\left(\varphi\right), \qquad \bar{w}_1\left(\varphi\right) = \bar{\sigma}_1 \bar{W}_1\left(\varphi\right) \tag{3.72}$$

where $\bar{U}_1\left(\varphi\right)$ and $\bar{W}_1\left(\varphi\right)$ are the non-dimensional 'deflection profiles'. Results will be displayed in terms of these deflection profiles, as well as the critical effective applied stress and the critical 'crown-point' deflection as a function of the detachment angle, φ_2, which are obtained from the transversality condition, Eq. (3.24), governing detachment propagation. When non-dimensionalized, Eq. (3.24) takes the form

$$\bar{\mathcal{G}}\left\{\varphi_2\right\} = \frac{1}{2\bar{R}^2}\left[\frac{\bar{D}}{\bar{R}^2}\left(\bar{u}_1' + \bar{w}_1''\right)^2 + \bar{C}\bar{u}_1'^2\right]_{\varphi=\varphi_2} = 2\bar{\gamma} \tag{3.73}$$

Substituting the relations found in Eq. (3.72) into Eq. (3.73) gives the critical effective applied stress in the form

$$\bar{\sigma}_{cr} = \sqrt{\frac{4\bar{R}^4\bar{\gamma}}{\bar{D}\left[\bar{U}_1'\left(\varphi_2\right) + \bar{W}_1''\left(\varphi_2\right)\right]^2 + \bar{C}\bar{R}^2\bar{U}_1'^2\left(\varphi_2\right)}} \tag{3.74}$$

Now, the critical 'crown-point' deflection follows as

$$\bar{\Delta}_{cr} \equiv \bar{w}_1\left(0\right)\Big|_{\bar{\sigma}_1=\bar{\sigma}_{cr}} = \bar{\sigma}_{cr}\bar{W}_1\left(0\right) \tag{3.75}$$

Results are presented in the form of the rescaled stress and rescaled 'crown-point' deflection,

$$\tilde{\sigma}_{cr} = \frac{\bar{\sigma}_{cr}}{\sqrt{2\bar{\gamma}}}, \qquad \tilde{\Delta}_{cr} = \frac{\bar{\Delta}_{cr}}{\sqrt{2\bar{\gamma}}} \tag{3.76}$$

respectively. The critical stresses and deflections in Eq. (3.76) are presented in the form of threshold paths, where each point on such a path corresponds to an equilibrium configuration of the detaching retina at the threshold level. In interpreting the results of the threshold paths, it is of interest to determine whether the detachment process will propagate

in a stable or unstable manner. If the path is monotonically increasing, then an incremental increase in stress is required to produce an increment in detachment size, so detachment propagation is stable. If the path is in the form of a U-shape, initially decreasing with detachment angle and then increasing, then, when the stress achieves a critical value for a given detachment angle on the descending portion of the path, detachment will occur in an unstable manner at a constant stress level. In this case, detachment will progress dynamically, represented by a horizontal jump to the corresponding equilibrium configuration on the increasing segment of the path. Subsequent propagation along the increasing segment will be stable, as an increment in stress is required to produce an increment in detachment angle. If the threshold path is monotonically decreasing, then once the critical stress level is achieved for a given detachment angle, it is achieved for all subsequent angles at that stress level. As a result, detachment will propagate in an unstable and catastrophic manner.

3.5.1   Case 1: No Retinal Tear

Results for a detaching retina without a retinal tear are presented in Figures 3.3-3.10. The deflection profiles per unit applied stress, $\bar{U}_1\left(\varphi\right)$ and $\bar{W}_1\left(\varphi\right)$, for various values of detachment angle, φ_2, are presented in Figures 3.3 and 3.4, respectively. The representative normalized thickness $\bar{h} = 0.009$, reflects a thickness of $h = 0.1\,\mathrm{mm}$ and a reference radius of $R_0 = 11\,\mathrm{mm}$. These values correspond to the retina at the periphery of the eye as discussed in Section 3.4. The Poisson's ratio is chosen as $\nu = 0.49$ as biological tissues are considered to be nearly incompressible. A comparison between the radial deflection profile given in Section 3.3 and that of the radial deflection profile obtained by Bottega *et al.* [12], where meridian displacements were neglected, is also presented in Figure 3.4 for the same representative values for $\bar{h}$ and ν.

For the radial deflection profile, it is seen that qualitative behavior remains similar to that assuming vanishing meridian displacement. As for the previous study, it is found that 'dimpling' in the retina will occur for larger detachment angles ($\varphi \geq 0.3$). It is seen that, quantitatively, there is a substantial percentage increase in the value of the radial deflection profile when the meridian displacement is included. The meridian deflection profile in Figure 3.3 is seen to be an order of magnitude smaller than that of the radial deflection profile.

This result was assumed and acted as the original motivation for neglecting the meridian displacement in Bottega *et al.* [12]. However, it is found that neglecting this effect places an artificial constraint on the structure, and hence an artificial stiffness that has significant effects on the results for the other detachment characteristics of the retina.
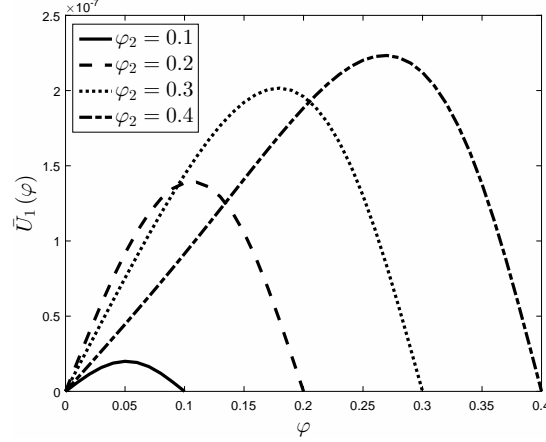
Figure 3.3: Comparison of the meridian deflection profiles (per unit effective applied stress) for various detachment angles, for a retina with no tear, $\bar{h} = 0.009$, $\nu = 0.49$, $\bar{R} = 1$, and $\bar{D} = 1$.
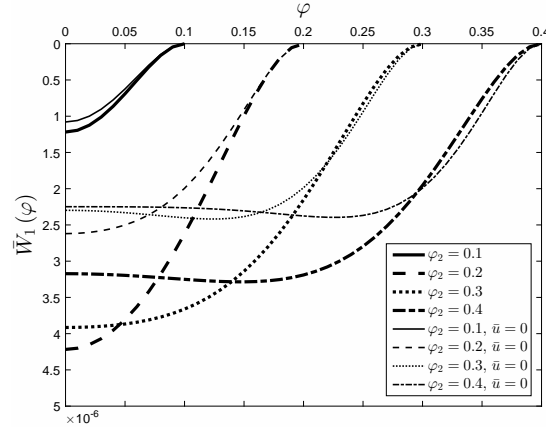
Figure 3.4: Comparison of the radial deflection profiles (per unit effective applied stress) from Eq. (3.56) to the radial deflection profile (per unit effective applied stress) obtained when neglecting the meridian displacement, for a retina with no tear, $\bar{h} = 0.009$, $\nu = 0.49$, $\bar{R} = 1$, and $\bar{D} = 1$.

The critical stress for detachment propagation, $\tilde{\sigma}_{cr}$, is presented in Figure 3.5 along with the resulting critical stress with the meridian deflections neglected. It is seen that both models predict that once detachment ensues it does so in an unstable manner and

is extensive in scope, which is in agreement with clinical observation. (See, for example, Wilkinson & Rice [84].) However, it is seen that including the meridian displacement lowers the critical stress, as the retina now represents a more compliant structure. This result is important since detachment propagation as predicted by the more accurate model will occur at lower stress levels for the same detachment angle. For the current study, the emergence of a very shallow unstable 'well' in the threshold path is noted for a detachment of approximately $\varphi_2 = 0.19$. At such a location, stable growth of the detachment boundary is possible. For values slightly less than $\varphi_2 = 0.19$, unstable but bounded growth is possible. The critical 'crown-point deflection', $\tilde{\Delta}_{cr}$, appears in Figure 3.6 along with the result ob-

Figure 3.5: Critical stress threshold path comparison for a retina with no tear, $\bar{h} = 0.009$, $\nu = 0.49$, $\bar{R} = 1$, and $\bar{D} = 1$. Current analysis appears as a solid line; analysis with meridian displacement neglected appears as a dashed line.

tained when neglecting the meridian deflections. Both curves take the same general shape with the current results having a much larger numerical value. This is expected, as the retina with the meridian displacements included represents a more compliant structure, as described previously.

A parameter study on the influence that the radius of the retina has on the critical stress for retinal detachment propagation in emmetropic eyes appears in Figure 3.7. It is seen that for emmetropic eyes of larger radius, detachment propagates at a lower value of the critical stress when the thickness of the retina is held constant. A similar parameter study on the Young's modulus of the retina and its influence on the critical stress appears in Figure 3.8. The elasticity of biological tissue is extremely difficult to measure accurately,
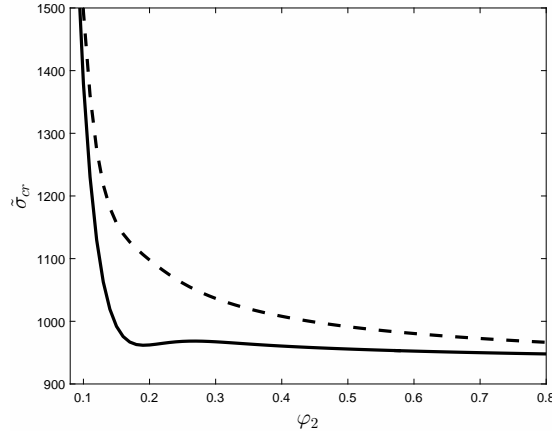
Figure 3.6: Critical crown-point deflection threshold path comparison for a retina with no tear, $\bar{h} = 0.009$, $\nu = 0.49$, $\bar{R} = 1$, and $\bar{D} = 1$. Current analysis appears as a solid line; analysis with meridian displacement neglected appears as a dashed line.

as the mechanical properties break down quickly upon death of the tissue. This leads to large variation in the measured elastic properties of the retina. The critical stress is shown in Figure 3.8 for a Young's modulus of both an order of magnitude less and an order of magnitude greater than the nominal value employed in this study. As the Young's modulus increases, the critical stress required for detachment propagation also increases since the structure is less compliant to loading.

It is also of interest to examine the influence of Poisson's ratio and of the thickness ratio of the retina on detachment propagation. Here, it is noted that the non-dimensional stress defined by Eq. $(3.27)_1$ is scaled by both ν and h. Hence, the normalized stress in that form is inappropriate for the intended comparison. Therefore, a set of alternative measures are introduced to perform the desired parameter study. Toward this end, the deflections can be expressed in the forms

$$\bar{u}_1 (\varphi) = \sigma_1^* \hat{U}_1 (\varphi), \qquad \bar{w}_1 (\varphi) = \sigma_1^* \hat{W}_1 (\varphi) \tag{3.77}$$

where

$$\sigma_1^* = \frac{\sigma_1}{E_0}, \qquad \hat{U}_1 (\varphi) = \frac{12 \left(1 - \nu^2\right)}{\bar{h}^3} \bar{U}_1 (\varphi), \qquad \hat{W}_1 (\varphi) = \frac{12 \left(1 - \nu^2\right)}{\bar{h}^3} \bar{W}_1 (\varphi) \tag{3.78}$$

Substituting Eq. (3.77) into the transversality condition, Eq. (3.24), leads to an alternative
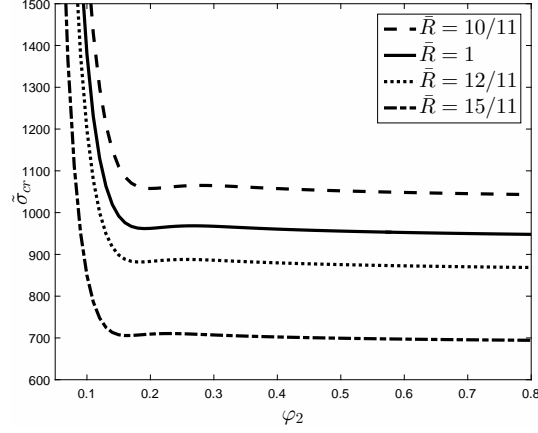
Figure 3.7: Critical stress threshold path comparison for a retina with no tear, $\bar{h} = 0.009$, $\nu = 0.49$, and $\bar{D} = 1$, for various values of $\bar{R}$ with R_0 held constant at 11 mm.

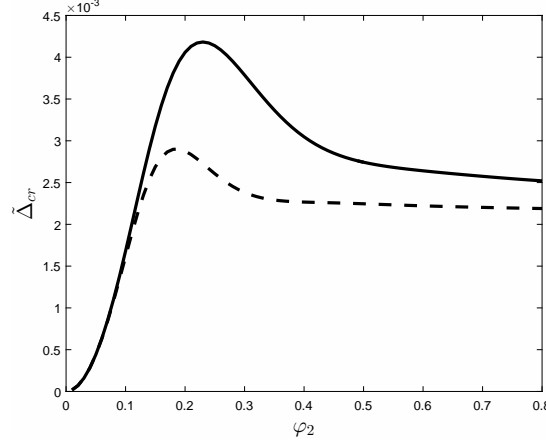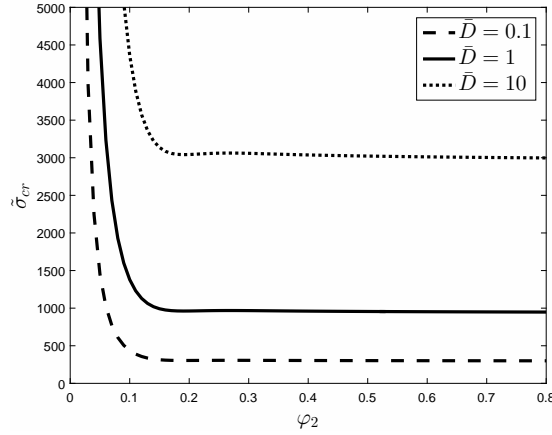

Figure 3.8: Critical stress threshold path comparison for a retina with no tear, $\bar{h} = 0.009$, $\nu = 0.49$, and $\bar{R} = 1$, for various values of $\bar{D}$.

form for the critical effective applied stress. Hence,

$$\sigma_{cr}^* = \sqrt{\frac{\bar{R}^4 \bar{h}^3 \hat{\gamma}}{3\left(1 - \nu^2\right)\left\{\bar{D}\left[\bar{U}_1'\left(\varphi_2\right) + \bar{W}_1''\left(\varphi_2\right)\right]^2 + \bar{C}\bar{R}^2\bar{U}_1'^2\left(\varphi_2\right)\right\}}} \tag{3.79}$$

where

$$\hat{\gamma} = \frac{\gamma}{E_0 R_0} \tag{3.80}$$

Results are presented in terms of the rescaled stress given by

$$\tilde{\sigma}_{cr}^* = \frac{\sigma_{cr}^*}{\sqrt{2\hat{\gamma}}} \tag{3.81}$$

The threshold curve in Figure 3.9 illustrates the influence of the thickness ratio on

the critical behavior of the detaching retina. As the thickness ratio increases, the critical stress for detachment propagation decreases since the thicker, less flexible, retina produces the same energy release rate at a smaller deflection and lower load. In accordance with Section 3.4, $\bar{h} = 0.009$ corresponds to the thickness of the retina at the periphery, $\bar{h} = 0.013$ corresponds to the midperiphery, and $\bar{h} = 0.021$ corresponds to the posterior of the eye. At the posterior, at $\varphi_2 \approx 0.27$ the axisymmetry of the model would be affected by the presence of the optic nervehead, which is a strong point of retinal adhesion. Similarly at the periphery, the presence of the ora serrata at $\varphi_2 \approx 0.45$ would affect the axisymmetric idealization of the model.
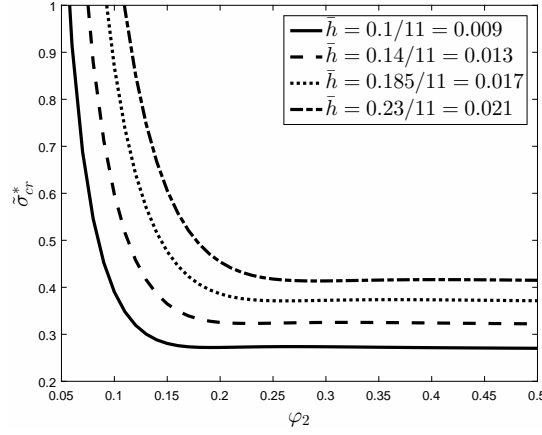
Figure 3.9: Dependence of the critical stress threshold path on the retinal thickness to radius ratio for a retina with no tear, $\nu = 0.49$, $\bar{R} = 1$, and $\bar{D} = 1$.

The threshold curve in Figure 3.10 illustrates the influence of Poisson's ratio on the critical behavior of the detaching retina. It is seen that as the Poisson's ratio decreases, the energy release rate is decreased, which results in the critical stress decreasing with decreasing Poisson's ratio. As the value of Poisson's ratio decreases, the shallow unstable 'well' in the growth path is no longer present. As with the Young's modulus, the value of Poisson's ratio for a given eye is difficult to mearure accurately, but biological tissue is generally assumed to be nearly incompressible with $\nu \approx 0.49$.
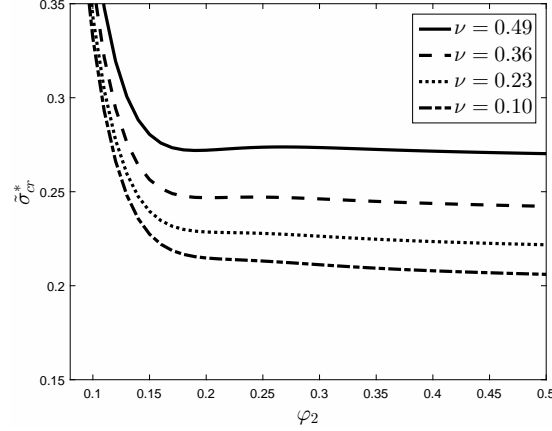
Figure 3.10: Dependence of the critical stress threshold path on Poisson's ratio for a retina with no tear, $\bar{h} = 0.009$, $\bar{R} = 1$, and $\bar{D} = 1$.

3.5.2   Case 2: Retinal Tear/Hole Present

Results are presented in Figures 3.11-3.18 for the situation where a retinal tear of angle φ_0 is present at the center of the detached region. The deflection profiles per unit applied stress, $\bar{U}_1(\varphi)$ and $\bar{W}_1(\varphi)$, for various values of detachment angle, φ_2, are presented in Figures 3.11 and 3.12, respectively, for a retina with a tear of angle $\varphi_0 = 0.05$ radians and the representative normalized thickness $\bar{h} = 0.009$ and Poisson's ratio $\nu = 0.49$. A comparison between the radial deflection profile given in Section 3.3 and that of the radial deflection profile obtained when the meridian displacements are neglected (Bottega *et al.* [12]), is also presented in Figure 3.12 for the same representative values of $\bar{h}$ and ν. The results are similar to that seen for a retina without a tear. The dimpling effect remains for larger detachment angles and the inclusion of the meridian displacements results in a substantial percentage increase in the radial deflection profile.

The critical stress and critical 'crown-point' deflection threshold paths for a retina with a tear of angle $\varphi_0 = 0.05$ are presented in Figures 3.13 and 3.14, respectively, along with the comparative results obtained when neglecting the meridian deflections. In this case, including the meridian displacements is seen to lower the critical stress threshold path in a manner similar to that of the case without a tear. Here, however, the unstable, 'well' in the critical stress path of Figure 3.13 has grown deeper when compared with the threshold path of Figure 3.5 for no tear in the retina. For the small range of detachment angles within
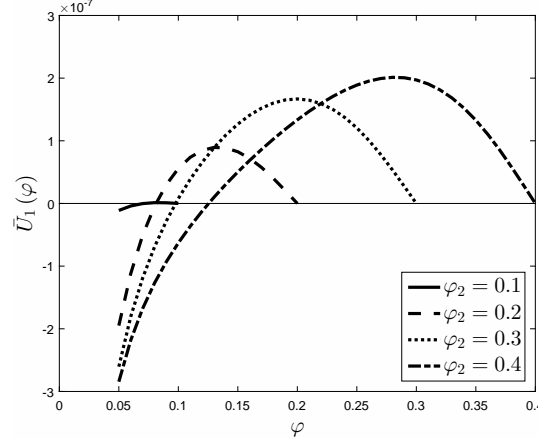
Figure 3.11: Comparison of the meridian deflection profiles (per unit effective applied stress) for various detachment angles, for a torn retina with $\varphi_0 = 0.05$, $\bar{h} = 0.009$, $\nu = 0.49$, $\bar{R} = 1$, and $\bar{D} = 1$.

the 'well', unstable but bounded growth of the detached area is possible for a limited range of the effective applied stress. For detachment angles outside but less than those that fall within the well, the presence of the tear is seen to raise the critical stress for propagation over that for a retina without a tear (Figure 3.15). For detachment angles outside but greater than those within the well, the stress threshold paths with or without a tear are seen to tend to a common asymptote. Hence, a retinal tear seems to have a stabilizing effect with regard to detachment propagation.

The results displayed in Figures 3.16-3.18 show the influence of the size of the retinal tear on detachment propagation. Deflection profiles with a detachment angle of $\varphi_2 = 0.3$ radians are shown for various tear sizes in Figure 3.16. The dependence of the critical stress on the size of a tear is shown in Figure 3.17. It is seen that the critical stress increases as the tear size increases for smaller detachment angles. It is also seen that as the tear size increases the unstable 'well' that was evident in Figure 3.13 increases in depth and breadth and shifts to the right. This reaffirms the deduction that, while a tear in the retina may have many negative effects, it seems to have a stabilizing effect with regard to detachment propagation. The dependence of the critical 'crown-point' deflection on the size of the retinal tear is shown in Figure 3.18.
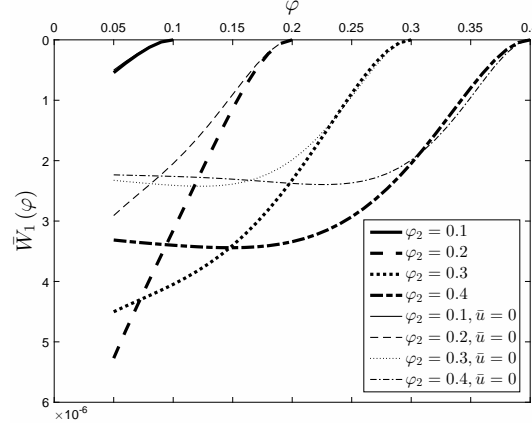
Figure 3.12: Comparison of the radial deflection profiles (per unit effective applied stress) from Eq. (3.56) to the radial deflection profile (per unit effective applied stress) obtained when neglecting the meridian displacement, for a torn retina with $\varphi_0 = 0.05$, $\bar{h} = 0.009$, $\nu = 0.49$, $\bar{R} = 1$, and $\bar{D} = 1$.

3.5.3 Bond Energy of the Retina to RPE Interface

A value for the bond energy, γ, of the retina to RPE interface is determined by applying the results of this study to experimental data published in the literature. Kain [36] studied retinal adhesion by injecting saline solution into the retina-RPE interface of *in vitro* rabbit eyes. The author found that retinal detachments formed in circular blisters and hence concluded that the adhesion of the retina to the RPE and the elasticity of the retina were uniform in all directions. The author also found that normal adhesion was found up to ten minutes after enucleation of the rabbit eyes, and that adhesion was subsequently reduced with further elapsed time post enucleation.

Kita *et al.* [38] studied retinal adhesion by injecting salt solution into the retina-RPE interface of *in vivo* rabbit eyes. The authors measured the IOP, the pressure within the dome-shaped retinal detachment, and the size of the detachment as the solution was injected into the subretinal space. Hence the authors were able to measure the critical pressure difference across the retina for which detachment would begin to propagate for various detachment sizes. Kita and Marmor [37] conducted the same *in vivo* experiment on cat and monkey eyes in addition to rabbit eyes and found that the adhesive force of the retina to RPE interface in monkey eyes is 140% greater than that in rabbit eyes.

In both Kita *et al.* [38] and Kita and Marmor [37] the authors used their data to

Figure 3.13: Critical stress threshold path comparison for a torn retina with $\varphi_0 = 0.05$, $\bar{h} = 0.009$, $\nu = 0.49$, $\bar{R} = 1$, and $\bar{D} = 1$. Current analysis appears as a solid line; analysis with meridian displacement neglected appears as a dashed line.

determine the adhesive force per unit length of the retina to RPE interface. However, for an energy based detachment criterion, as employed in this study, it is necessary to determine the energy required to produce a unit area of detachment, γ, of the retina-RPE interface. In doing so, we assume that the adhesion of a human retina will more closely match that of a primate than that of a rabbit and, hence, that adhesion in humans will be 140% greater than that in rabbit eyes, in accordance with Kita and Marmor [37] for monkey retinas. As a result, we increase the raw data for the critical pressure presented in Kita *et al.* [38] for rabbit retinas by 140% while holding the detachment size constant when calculating a value for the energy of detachment in the human retina. The modified critical pressure data is then taken as the critical stress found in Eq. (3.74). The corresponding detachment size is also taken from the experimental data, from which the deflection profiles are determined. In this calculation, the retinal radius of $R_0 = 11$ mm and the Young's modulus of $E_0 = 4.65 \cdot 10^4$ Pa along with a Poisson's ratio of $\nu = 0.49$ and the average of the midperiphery and posterior retinal thicknesses, $h = 0.185$ mm, are substituted into Eq. (3.74). The energy of detachment per unit area is thus found to be $\gamma = 0.0384$ N/m.
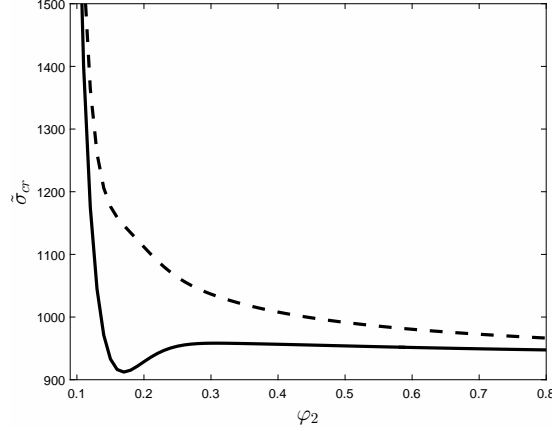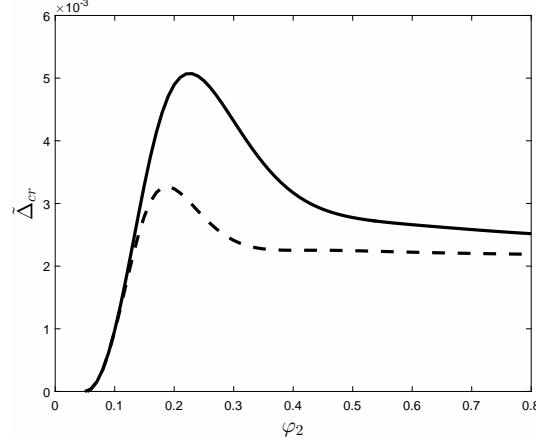
Figure 3.14: Critical crown-point deflection threshold path comparison for a torn retina with $\varphi_0 = 0.05$, $\bar{h} = 0.009$, $\nu = 0.49$, $\bar{R} = 1$, and $\bar{D} = 1$. Current analysis appears as a solid line; analysis with meridian displacement neglected appears as a dashed line.

3.6   Conclusions

The mechanical behavior of retinal detachment propagation in emmetropic eyes has been studied. The formulation of a mechanics based mathematical model for retinal detachment that considers axisymmetric deformation and detachment of the retina was presented. The stress resulting from the contraction of the vitreous and the extension of its fibrils, along with interfacial pressure, were taken as the impetus for detachment propagation. The simplifying assumption of negligible meridian deflection used in the solution procedure of the model presented in Bottega *et al.* [12] was removed in order to obtain an improved solution that more accurately models the behavior of a detaching retina. Exact, analytical solutions for the radial displacements, and the corresponding meridian displacements, were obtained for detaching retinas with a central tear as well as for retinas without a tear. Although the formulation allows for a region of sliding contact adjacent to the intact region, results indicate that a contact zone does not physically occur for the range of detachment sizes considered. Simulations based on the analytical solutions were performed, revealing critical characteristic behavior of detachment propagation. The results are summarized below, beginning with retinas without a central tear.

Case 1: No retinal tear

It was seen that including the meridian displacements results in a substantial percentage
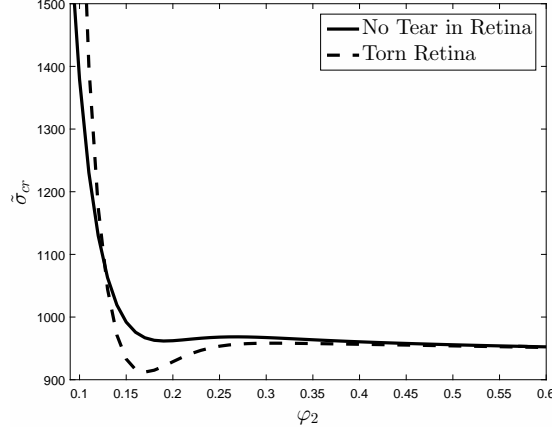
Figure 3.15: Critical stress threshold path comparison between a torn retina with $\varphi_0 = 0.05$ and a retina without a tear with $\bar{h} = 0.009$, $\nu = 0.49$, $\bar{R} = 1$, and $\bar{D} = 1$.

increase in the magnitude of the radial deflection profile. However, the qualitative behavior of the radial deflection profile remains similar, with 'dimpling' in the retina occurring for larger detachment angles. The meridian deflection profile was seen to be an order of magnitude smaller than that of the radial deflection profile, but its inclusion is seen to have significant effects on the critical condition for detachment propagation. The threshold path for the applied effective stress shows that detachment propagation is catastrophic in nature, which is in agreement with the results of Bottega *et al.* [12], as well as with clinical observations. However, the inclusion of the meridian displacements resulted in a lower critical stress than that found by Bottega *et al.* [12]. This, of course, has important ramifications.

Parameter studies were performed in order to determine the influence of Poisson's ratio, the thickness to radius ratio of the retina, the radius of the retina, and the Young's modulus of the retina on characteristic behavior of detachment propagation. Results indicated that as the radius increased, the critical stress required for detachment propagation decreased. Results also indicated that as the Young's modulus, Poisson's ratio, or thickness ratio increased, the critical stress tended to decrease.

Case 2: Retinal Tear Present

It was seen that including the meridian displacements with a tear present had similar effects on the radial deflection profile as for when no tear was present. The radial deflection profile displayed a substantial percentage increase in magnitude while 'dimpling' was present
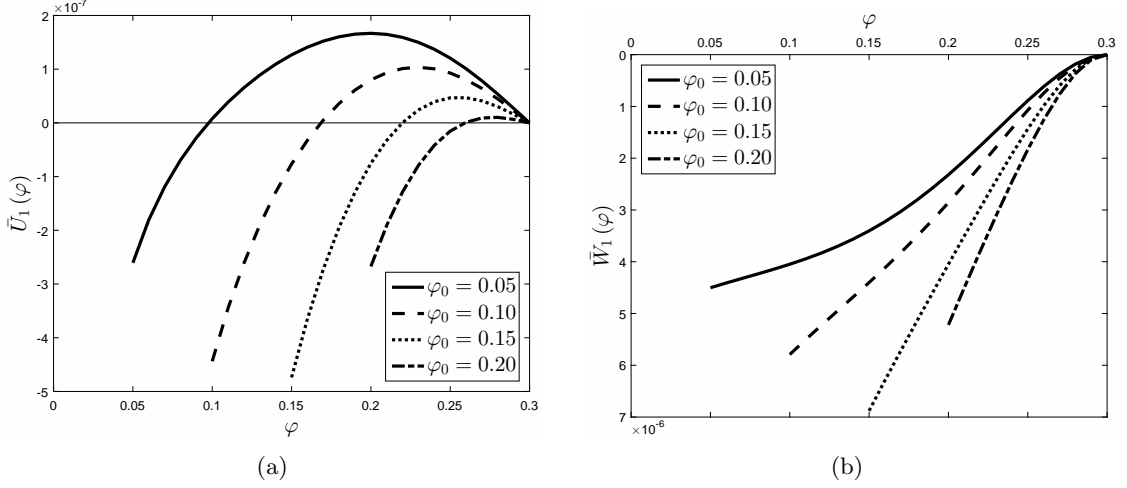
Figure 3.16: Comparison of the deflection profiles (per unit effective applied stress) for torn retinas with selected tear angles, $\bar{h} = 0.009$, $\nu = 0.49$, $\bar{R} = 1$, and $\bar{D} = 1$: (a) the meridian deflection profile and (b) the radial deflection profile.

for 'larger' detachment sizes. The inclusion of the meridian displacement was seen to lower the critical stress, as for retinas without a tear, as well as to facilitate the development of unstable 'wells' in the threshold paths. When compared to the results of Bottega *et al.* [12], the unstable 'wells' are seen to develop at smaller tear sizes and are larger in depth and breadth for a given tear size. When compared to retinas without a tear, it was seen that, for detachment angles outside but less than those that fall within the 'well', the presence of the tear raises the critical stress. Hence, it appears that the tear has a stabilizing effect with regard to detachment propagation in this sense, and that this stabilizing effect is more pronounced with the inclusion of the meridian displacements.
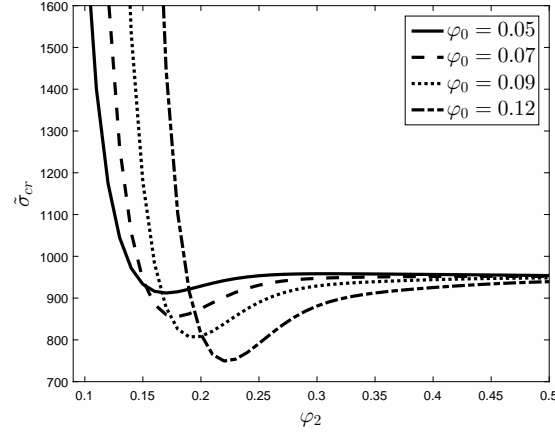
Figure 3.17: Critical stress threshold paths for torn retinas with selected tear angles with $\bar{h} = 0.009$, $\nu = 0.49$, $\bar{R} = 1$, and $\bar{D} = 1$.
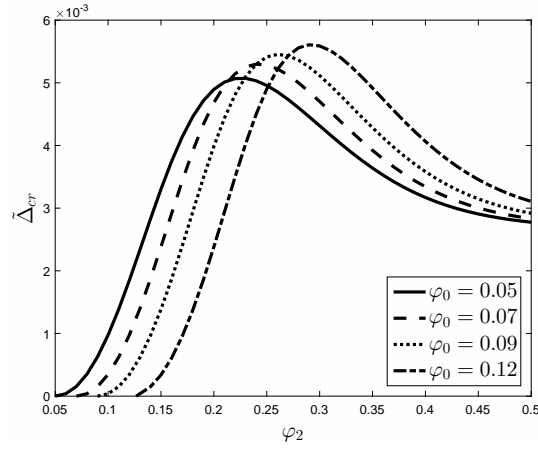
Figure 3.18: Critical crown-point deflection threshold paths for torn retinas with selected tear angles with $\bar{h} = 0.009$, $\nu = 0.49$, $\bar{R} = 1$, and $\bar{D} = 1$.

Chapter 4

The Mechanics of Myopia and Its Influence on Retinal Detachment

4.1   Introduction

In a review of epidemiology studies concerning rhegmatogenous retinal detachment detachment (RRD) dating from 1970 to 2009, Mitry *et al.* [52] found that the largest annual incidence of RRD occurred in the 60-70 year age group with a secondary peak in young myopic patients. The model for the emmetropic eye presented in Chapter 3 investigated the mechanical factors that contribute to retinal detachment that are associated with aging and would largely effect the 60-70 year age group. In this Chapter, the mechanical factors contributing to the increased prevalence of retinal detachment in individuals with myopic eyes, when compared to individuals with emmetropic or hyperopic eyes, are investigated. The theory of thin elastic shells developed in Chapter 2 is again applied to model the propagation of retinal detachment in the myopic eye. The corresponding growth law for detachment propagation in the myopic eye cannot, however, be obtained from the growth law for the general shell presented in Chapter 2. As the outer layers of the myopic eye do not remain in a spherical configuration, the derived growth law for the myopic eye is similar in form to that of a shell with a compliant outer layer.

The myopic eye is known to be larger when compared to the emmetropic eye, particularly in antero-posterior axial length, which has led to much research on measuring the shape of the retina and outer eye in myopic and emmetropic eyes (these shapes may differ due to variations in the thickness of the choroid and sclera [79]). Atchison *et al.* [3] measured

---

Portions of this Chapter previously appeared as: Lakawicz, J.M., Bottega, W.J., Fine, H.F., and Prenner, J.L., 2017. *On the mechanics of myopia and its influence on retinal detachment.* Revision in review.

axial (anterior-posterior), vertical (superior-inferior), and horizontal (nasal-temporal) retinal dimensions of emmetropic and myopic subjects using T1-weighted magnetic resonance imaging (MRI). From a linear fit of their data, the authors found changes in dimension per diopter of refractive error (D) increasing at a rate of 0.35 mm/D in axial length, 0.19 mm/D in height, and 0.10 mm/D in width as myopia increases. The same MRI measurements were fit to three dimensional ellipsoids by Atchison *et al.* [4], in which the authors found that emmetropic retinas tend to be oblate in shape (larger in height and width than axial length). The authors also found that retinal oblateness decreases with increasing myopia but that few myopic retinas reached a prolate shape. The subjects in Atchison *et al.* [3],[4] ranged from 18 to 36 years in age and were 84% white. Similar observations were found in Gilmartin *et al.* [29] using T2-weighted MRI of the retinas of adult subjects in the United Kingdom with no mention of race. Ishii *et al.* [34] found the retinal shape to be oblate near birth and trend toward a prolate shape during childhood eye development in their MRI study of Japanese patients ranging in age from 1 month to 19 years old. Both the data from Atchison *et al.* [3],[4] and the data from Ishii *et al.* [34] display large variability in retinal shape for eyes possessing the same refractive error, which is evident for the entire range of refractive errors measured in the data. A literature review of studies measuring retinal shape and eye shape using both MRI and other techniques is found in Verkicharla *et al.* [79], where the large variation in retinal shape for eyes displaying the same refractive error is a common theme among the reviewed studies.

While it is known that the axial length of the eye increases in myopic patients, the exact etiology of myopia and its progression in human patients is not yet known. Numerous studies have been conducted in which myopia is experimentally induced in animal subjects through form deprivation or disruption of the visual field (i.e. Young [87], Smith *et al.* [73], Wallman *et al.* [81], [82], Miles & Wallman [51], and Schaeffel *et al.* [69]). All experiments required young animals in order to produce myopia and the relation of these studies to normal eye growth in humans is not known. Feldkaemper & Schaeffel [20] provide a literature review on the effects of dopamine and other biochemical agents on the development of myopia. Greene [31] studied the stress exerted on the posterior sclera from the extraocular muscles, as well as the stress that would develop in the sclera from changes in intraocular pressure

(IOP) during accommodation and convergence. A further literature review on the effects of IOP on myopia is found in Pruett [59]. McBrien *et al.* [48] studied changes in the scleral matrix of myopic eyes and found it to be weaker with reduced collagen content in myopic mammalians. A potential theory for unifying many of these factors in the development of myopia has been proposed by Hung *et al.* [33].

At birth, the retina has almost entirely all of the cells it will have throughout life, which leads to thinning of the retina during normal development in order to maintain its coverage of the inner surface of the choroid-scleral shell [66]. However, there is evidence of increased retinal elongation and thinning in myopic eyes when compared to emmetropic eyes. Lin *et al.* [45] found that the total area of the retinal pigment epithelium (RPE) was 11% greater after one week and 21% greater after two weeks in chick eyes with form deprivation myopia when compared to control eyes. The authors also indicate no evidence of cell division within the RPE and that the increased size of the RPE resulted from enlargement of individual RPE cells. Whether the enlarged size of the myopic RPE cells resulted from increased biological growth or from mechanical stretching could not be determined. Gella *et al.* [28], similarly, found increased thinning in the RPE in human myopic patients compared to emmetropic patients using SD-OCT scans. The thickness of the other retinal layers was not significantly different in comparing the two patient groups. The studies reviewed in the present study suggest both the change in shape of the sclera with the development of myopia and the corresponding changes in the retina result from a combination of mechanical and biochemical factors.

In the present work, a mathematical model for retinal detachment due to the geometric changes of the eye associated with myopia is introduced. The model for the deformation of the retina includes a change of shape due to biological growth of the retinal tissue, as well as elastic deformation imposed on the retina due to the change in shape of the much stiffer choroid and sclera. In Skalak [72], Rodriguez *et al.* [65], and others, the effects of growth and elastic deformation on biological tissues are modeled mathematically through a decomposition of the deformation gradient tensor for a given tissue into a growth deformation tensor and an elastic deformation tensor. Application of that decomposition to the retina, corresponds to a mapping of the retinal tissue from an emmetropic state to

a hyopothetical growth state, followed by a mapping of the hypothetical growth state to the myopic state that the retina is constrained to by the choroid and sclera. For small strains, such a decomposition is shown to be a linear summation of the strain induced on the tissue by growth and the strain induced by elastic deformation (see, for example, Nelson *et al.* [57]).

First, the mathematical model for myopia-induced retinal detachment is introduced in Section 4.2. The model incorporates both the growth of the retinal tissue and its elastic deformation due to the constraints imposed on it by the myopic shape of the choroid and sclera. Then analytical solutions for the model are presented in Section 4.3, along with the corresponding results based on those solutions in Section 4.4.

4.2 The Mathematical Model

The retina is modeled as a linearly elastic thin shell with thickness h, Young's modulus E_0, Poisson's ratio ν, and radius R_0 when in the emmetropic spherical state. The model considers axisymmetric deformation with the transverse displacement, $w(\varphi)$, positive outward[1] and the meridian displacement, $u(\varphi)$, positive in the direction of increasing azimuth angle, φ, as defined in Figure 4.1. Due to the axisymmetry about $\varphi = 0$, the deformation will be the same for all values of the polar angle, θ, and therefore the displacement in the polar direction vanishes.

4.2.1 Growth of the Retina Due to Myopia

First, consideration is given to the evolution of the intact retina due to the changes in geometry of the outer eye that accompany myopia. As stated in the Section 4.1, the measurement data on the dimensions of the myopic retina display large variability in retinal shape for eyes possessing the same refractive error. This is evident for the entire range of refractive errors measured ([3], [4], [29], [34], and [79]). Atchison *et al.* [3] and [4] found that, of their 66 myopic subjects who possessed a range of refractive errors from -0.75 D to -12 D, most had oblate retinal shapes with only 8 subjects having prolate retinal shapes.

---

[1]In both Chapters 2 and 3, the transverse displacement is taken as positive inward.

However, these 8 subjects had refractive errors of -1, -3.25, -3.25, -5.625, -6.25, -6.375, -7.25, and -7.50 D, which spans most of the myopic range of the subjects in the study. Ishii *et al.* [34] found that the retina trends toward a prolate shape during childhood eye development in their MRI study of Japanese patients ranging in age from 1 month to 19 years old, which calls into question age and race influences on retinal shape. Hence, due to the large variability in measured retinal shape, it is assumed that the emmetropic eye is spherical in shape for mathematical simplicity. As the outer eye changes from emmetropic to myopic, it is assumed that the retina will displace from a spherical state to an ellipsoidal state in order to remain in bonded contact with the RPE.
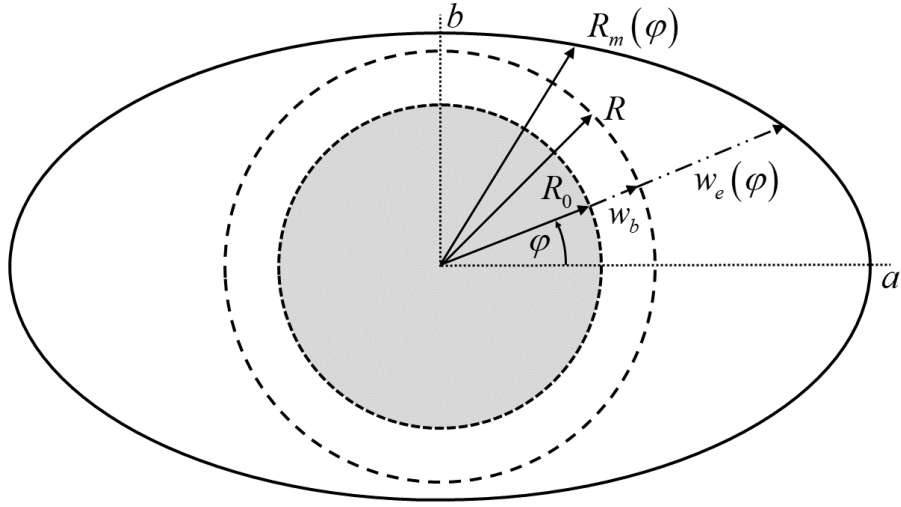
Figure 4.1: Schematic of the evolution of the intact retina due to the onset of myopia in the eye. (Image not drawn to scale.)

The mathematical model for the myopic retina is developed in accordance with the model for stress-dependent growth in elastic tissues presented in Rodriguez *et al.* [65]. The model includes an intermediate spherical state that defines the deformation of the retina due to stress-free biochemical growth. This corresponds to the state that the retinal tissue would occupy if it were to grow independently. That is, if not constrained by the outer layers of the eye. The retina is then mapped from the spherical stress-free growth state to the ellipsoidal myopic state by an elastic deformation resulting from the constrained shape imposed upon the retina by the outer layers of the eye.

Since the emmetropic retina is taken to be spherical, unconstrained growth of the retina would result in a uniform expansion of the emmetropic sphere. It is, therefore, natural to take the intermediate growth state as spherical as well. As the mapping from the emmetropic state to the intermediate growth state is unconstrained, it is taken to be stress free. The growth displacement field from the emmetropic coordinates $(R_0, \varphi_0, \theta_0)$ to the growth coordinates (R, φ, θ) is prescribed as

$$R = R_0 + w_b, \qquad \varphi = \varphi_0, \qquad \theta = \theta_0 \tag{4.1}$$

where w_b is the radial displacement of the growth state, as shown in Figure 4.1. With the retina modeled as a thin shell, the transverse displacement is constant through the thickness of the retina. Hence, the deformation gradient from the emmetropic spherical state to the spherical stress-free growth state takes the form,

$$\boldsymbol{F}_g = \begin{bmatrix} 1 & 0 & 0 \\ 0 & 1 + \frac{w_b}{R_0} & 0 \\ 0 & 0 & 1 + \frac{w_b}{R_0} \end{bmatrix} \tag{4.2}$$

The retina is then mapped from the stress-free growth state to the final myopic state with coordinates $(R_m, \varphi_m, \theta_m)$ by a displacement of the form,

$$R_m = R + w_e(\varphi), \qquad \varphi_m = \varphi + \frac{1}{R}\tilde{u}_e(\rho, \varphi), \qquad \theta_m = \theta \tag{4.3}$$

where $w_e(\varphi)$ is the transverse elastic displacement, which is constant through the thickness of the retina when modeled as a thin shell. The transverse elastic displacement is coupled with the elastic meridian displacement, $\tilde{u}_e(\rho, \varphi)$, which varies linearly through the thickness of the retina as was shown for the general shell in Eq. (2.91a). Hence,

$$\tilde{u}_e(\rho, \varphi) = u_e(\varphi) + \rho\beta_\varphi(\varphi) \tag{4.4}$$

where $u_e(\varphi)$ is the elastic meridian displacement at the center line of the retina and $\beta_\varphi(\varphi)$ is the component of the rotation vector whose normal is tangent to the meridian direction of the retina. In this Chapter, R is taken as the radius of the stress-free growth state and ρ is a coordinate measured positive outward from the center line of the retina.

The resulting elastic deformation gradient from the stress-free growth state to the ellipsoidal myopic states takes the form,

$$
\boldsymbol{F}_e =
\begin{bmatrix}
1 & \frac{1}{R}\left(\frac{\partial w_e}{\partial \varphi} - u_e - \rho\beta_\varphi\right) & 0 \\
\beta_\varphi & 1 + \frac{1}{R}\left(w_e + \frac{\partial u_e}{\partial \varphi} + \rho\frac{\partial \beta_\varphi}{\partial \varphi}\right) & 0 \\
0 & 0 & 1 + \frac{1}{R}\left\{w_e + \cot\varphi\left(u_e + \rho\beta_\varphi\right)\right\}
\end{bmatrix}
\tag{4.5}
$$

The deformation gradient of the ellipsoidal myopic state follows from the formulation for stress-dependent growth of elastic tissues in Rodriguez *et al.* [65] as

$$
\boldsymbol{F}_{eg} = \boldsymbol{F}_e \boldsymbol{F}_g
\tag{4.6}
$$

The strain tensor, $\boldsymbol{\varepsilon}$, for the myopic retina is determined entirely by the elastic deformation gradient as follows,

$$
\boldsymbol{\varepsilon} = \frac{1}{2}\left(\boldsymbol{F}_e^T \boldsymbol{F}_e - \boldsymbol{I}\right)
\tag{4.7}
$$

In this development, the corresponding results for the elastic displacements $w_e\left(\varphi\right)$ and $u_e\left(\varphi\right)$ are assumed to be small when compared to the radius of the growth state, R. (That is, $w_e/R \ll 1$ and $u_e/R \ll 1$.) However, no limitations are placed upon the magnitude of the radial growth displacement, w_b. Before proceeding, some additional concepts with regard to the prescribed shapes of the intermediate growth state and of the final myopic state are addressed.

The two dimensional cross-section of the myopic state of the intact retina is taken as an elliptic shape, as shown in Figure 4.1. The cross-section is then rotated about the $\varphi = 0$ axis to form a three dimensional ellipsoid. The equation for an ellipse in polar coordinates relative to its center is given as

$$
R_m\left(\varphi\right) = \frac{ab}{\sqrt{a^2 \sin^2\varphi + b^2 \cos^2\varphi}}
\tag{4.8}
$$

where $R_m\left(\varphi\right)$ is the distance from the center of the ellipse to its edge as given in Eq. (4.3), and a and b are the major and minor axes of the ellipse as shown in Figure 4.1.

The size of the intermediate growth state is characterized by its relative surface area as follows. First, the surface area of the final myopic ellipsoidal state of the retina is matched to the surface area of an equivalent sphere. The radius of this equivalent sphere is readily

shown to be given by the relation

$$R_G = \sqrt{\frac{1}{2}b^2 \left[1 + \frac{a}{b\sqrt{1 - b^2/a^2}} \arcsin\left(\sqrt{1 - \frac{b^2}{a^2}}\right)\right]} \qquad (4.9)$$

where a and b are the major and minor axis, respectively, of a prolate ellipsoid, as shown in Figure 4.1. Since biochemical growth is believed to play a small part in the deformation of the retina during the evolution of myopia ([28], [45], [66]), the surface area of the intermediate growth state is taken to be a percentage of the surface area of the equivalent sphere whose radius is given by Eq. (4.9). This percentage is defined as the growth parameter α, which is given as

$$\alpha = \frac{R^2 - R_0^2}{R_G^2 - R_0^2} \qquad (4.10)$$

where R_0 is the radius of the emmetropic retina and R is the radius of the intermediate growth state. The form of Eq. (4.10) establishes that when $\alpha = 0$ ($R = R_0$), the entirety of the myopic displacement of the retina is due to elastic deformation. When $\alpha = 1$ ($R = R_G$), the growth of the retina independent from the constraint imposed upon it by the outer eye has the same surface area as that of the myopic shape of the inner surface of the choroid[2].

The growth parameter, α, is taken as a prescribed value between zero and one. Solving Eq. (4.10) for R gives the radius of the intermediate growth state in terms of the growth parameter. Hence,

$$R = \sqrt{R_0^2 + \alpha\left(R_G^2 - R_0^2\right)} \qquad (4.11)$$

where R_G is solely dependent on the major and minor axes of the final myopic state of the retina as shown in Eq. (4.9). The final shape of the myopic state of the retina will enter the model as a prescribed parameter using the measurements of the size of myopic retinas available in Atchison *et al.* [3]. This will be discussed in Section 4.3.

4.2.2 Energy Formulation for Detachment

As the retina transforms from the stress-free growth state to the ellipsoidal myopic state, strain energy is stored within the retina. This strain energy associated with the geometric

---

[2]Although the surface areas are of equal value, the final myopic state of the retina will not be stress free when $\alpha = 1$. This is due to the constrained shape that the outer eye imposes on the growth of the retina ([65],[72]).

changes of the retina found in myopia, along with that due to pressure differences across the retina and stress acting on the retina from vitreous fibrils, may cause the retina to detach from the outer layers of the eye. In this section, the size and shape of the detached area of the retina if it were to detach from the outer eye during its myopic evolution is determined through an energy formulation similar to that presented for the emmetropic retina in Chapter 3.

The retina is taken to be detaching from a 'rigid' RPE-choroid-sclera foundation as justified in Section 3.4 for retinal detachment in emmetropic eyes. As in the previous Chapter concerning emmetropic eyes, the retina is divided into three regions; Region $\mathcal{R}_1$: the 'lift zone' for $0 \leq \varphi \leq \varphi_1$, Region $\mathcal{R}_2$: the 'contact zone' for $\varphi_1 \leq \varphi \leq \varphi_2$ where the retina maintains sliding contact with the RPE, and Region $\mathcal{R}_3$: the 'intact region' for $\varphi_2 \leq \varphi \leq \pi/2$ where the retina remains bonded to the RPE, all as shown in Figure 4.2. In Regions $\mathcal{R}_1 - \mathcal{R}_3$, the IOP, p_0, acts outward against the retina while stress acting
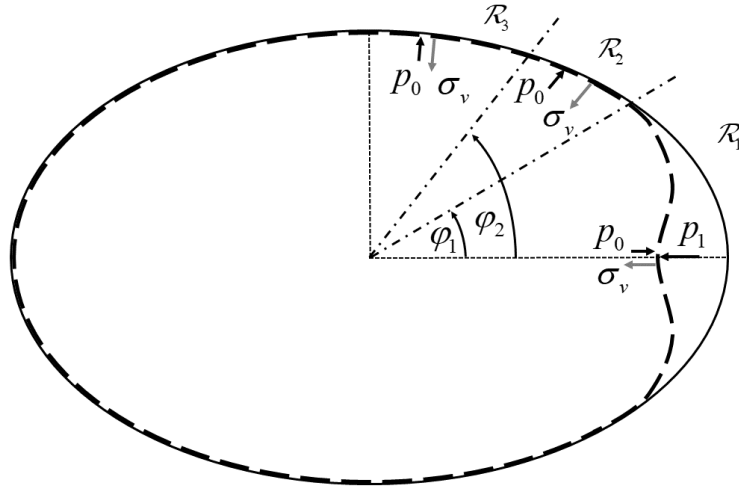
Figure 4.2: Schematic of the detaching retina in the myopic eye. (Image not drawn to scale.)

from the vitreous fibrils, σ_v, acts inward. In Region S_1, a pressure p_1 resulting from the accumulation of subretinal fluid acts inward in the subretinal space formed by the lift zone and will contribute to detachment when greater than the outward IOP.

The problem is approached as a propagating boundary value problem in the calculus

of variations, where the location of the boundary angles between the lift zone and contact zone, φ_1, and between the contact zone and intact region, φ_2, are allowed to vary arbitrarily, as well as the elastic deflections of the detaching retina, $w_j(\varphi)$ and $u_j(\varphi)$. The elastic deflections of the detaching retina are defined with reference to the stress-free growth state in the same manner as were the elastic deflections of the intact retina, $w_e(\varphi)$ and $u_e(\varphi)$, in Eq. (4.3). The final shape of the detaching retina is determined by matching the solution for the shape of the detaching retina to the shape of the intact retina at the detachment boundaries.

The potential energy functional, Π, for the ocular system in the myopic eye does not reduce directly from the formulation of the general shell in Chapter 2 due to the constraints imposed on the retina by the outer layers of the myopic eye. The potential energy functional is, however, still comprised of the elastic strain energy of the retina, U, and the work done by the applied stresses acting on the retina, $\mathcal{W}$ as in Eq. (2.117). In addition, a constraint functional, Λ, is included to insure the appropriate continuity of the displacements of the retina with those of the outer eye in the contact zone and in the intact region. Lastly, the energy of detachment, Γ, is the energy required to produce detachment propagation between the retina and the RPE.

The elastic strain energy takes the form

$$U = 2\pi R^2 \sum_{j=1}^{3} \int_{\mathcal{R}_j} \left[\tfrac{1}{2} N_{\varphi\varphi}^{(j)} \varepsilon_{\varphi\varphi}^{(j)} + \tfrac{1}{2} N_{\theta\theta}^{(j)} \varepsilon_{\theta\theta}^{(j)} + \tfrac{1}{2} M_{\varphi\varphi}^{(j)} \chi_{\varphi\varphi}^{(j)} + \tfrac{1}{2} M_{\theta\theta}^{(j)} \chi_{\theta\theta}^{(j)} \right] \sin\varphi \, \mathrm{d}\varphi \qquad (4.12)$$

The strains and bending measures that appear in the elastic strain energy functional are measured at the center line of the retina. The form of these parameters at the center line is obtained from the strain tensor found in Eq. (4.7). For thin shells that are axisymmetric about $\varphi = 0$, the strains and the bending measures in Region $\mathcal{R}_j$ ($j = 1 - 3$) are related to the corresponding displacements as

$$\varepsilon_{\varphi\varphi}^{(j)}(\varphi) = \frac{1}{R} \left\{ u_j'(\varphi) + w_j(\varphi) \right\}, \qquad \varepsilon_{\theta\theta}^{(j)}(\varphi) = \frac{1}{R} \left\{ u_j(\varphi) \cot\varphi + w_j(\varphi) \right\} \qquad (4.13)$$

$$\begin{aligned}
\chi_{\varphi\varphi}^{(j)}(\varphi) &= \frac{1}{R^2} \left\{ u_j'(\varphi) - w_j''(\varphi) \right\} = \frac{1}{R} \beta_\varphi^{(j)'}(\varphi), \\
\chi_{\theta\theta}^{(j)}(\varphi) &= \frac{1}{R^2} \cot\varphi \left\{ u_j(\varphi) - w_j'(\varphi) \right\} = \frac{1}{R} \cot\varphi \beta_\varphi^{(j)}(\varphi)
\end{aligned} \qquad (4.14)$$

where all derivatives are with respect to the coordinate φ. In Eqs. (4.14), β_φ is the component of the rotation vector with cross-section whose normal is tangent to the meridian direction of the retina. Its form is also found from the strain tensor of Eq. (4.7), since the transverse shear strains vanish for first order shell theories. Hence,

$$\beta_\varphi^{(j)}(\varphi) = \frac{1}{R}\left\{u_j(\varphi) - w_j'(\varphi)\right\} \tag{4.15}$$

For the axisymmetric deformation considered herein, the component of the rotation vector with cross-section whose normal is tangent to the polar direction, β_θ, vanishes. The strains, bending measures, and rotations given in Eqs. (4.13)-(4.15) are of the same form as in Chapters 2 and 3, but with the sign of w_j reversed, since in those Chapters the radial displacement was positive inward.

The work done on the myopic retina by the ocular pressure difference across the retina and the applied stress from the vitreous fibrils takes an alternate form when compared to the work done on the general shell in Eq. (2.119). The work of the applied stresses now acts through the deformation of the retina from the intermediate growth state to the final myopic state. Hence,

$$\mathcal{W} = 2\pi R^2 \int_{\mathcal{R}_1}(p_1 - p_0 + \sigma_v)(w_e - w_1)\sin\varphi\,\mathrm{d}\varphi + 2\pi R^2\sum_{j=2}^{3}\int_{\mathcal{R}_j}(\sigma_v - p_0)(w_e - w_j)\sin\varphi\,\mathrm{d}\varphi \tag{4.16}$$

where the pressures p_0 and p_1 and the stress σ_v act in the directions indicated in Figure 4.2.

The constraint functional for the myopic retina is modified from that of general shell in Eq. (2.120) in the same way as the work on the myopic retina was in Eq. (4.16). Hence,

$$\Lambda = 2\pi R^2\sum_{j=2}^{3}\int_{\mathcal{R}_j}\hat{\sigma}_j(w_e - w_j)\sin\varphi\,\mathrm{d}\varphi + 2\pi R^2\int_{\mathcal{R}_3}\hat{\tau}_3(u_e - u_3)\sin\varphi\,\mathrm{d}\varphi \tag{4.17}$$

where $\hat{\sigma}_2$, $\hat{\sigma}_3$, and $\hat{\tau}_3$ are Lagrange multipliers that ensure continuity of the transverse and meridian displacements of the retina with the RPE in the intact region and continuity of the transverse displacement in the contact zone.

The energy of detachment is given as

$$\Gamma = 2\pi R^2\int_{\mathcal{R}_1 + \mathcal{R}_2}2\gamma\sin\varphi\mathrm{d}\varphi - 2\pi R^2\int_{\mathcal{R}_{1_0} + \mathcal{R}_{2_0}}2\gamma\sin\varphi\mathrm{d}\varphi \tag{4.18}$$

where γ remains the energy required to produce a unit area of detachment between the retina and the RPE.

Applying the Principle of Stationary Potential Energy, while allowing the displacements $w_j(\varphi)$ and $u_j(\varphi)$, along with the boundaries φ_1 and φ_2 to vary, yields the self consistent governing equations, boundary conditions, and the transversality conditions that govern the location of the propagating boundaries of the detaching retina for the mathematical model for retinal detachment in myopic eyes presented herein.

4.2.3 Equilibrium Equations

The equations of equilibrium for the detaching retina are found from the variational formulation as

$$\left(Q_\varphi^{(j)} \sin \varphi\right)' - \left(N_{\varphi\varphi}^{(j)} + N_{\theta\theta}^{(j)}\right) \sin \varphi = \sigma_j R \sin \varphi \tag{4.19}$$

$$Q_\varphi^{(j)} \sin \varphi + \left(N_{\varphi\varphi}^{(j)} \sin \varphi\right)' - N_{\theta\theta}^{(j)} \cos \varphi = \tau_j R \sin \varphi \tag{4.20}$$

$$\left(M_{\varphi\varphi}^{(j)} \sin \varphi\right)' - M_{\theta\theta}^{(j)} \cos \varphi = R Q_\varphi^{(j)} \sin \varphi \tag{4.21}$$

where $Q_\varphi^{(j)}$ is the resultant transverse shear force per unit length in Region $\mathcal{R}_j$.

In addition, the constraint functional results in the transverse displacement in Region $\mathcal{R}_2$ given as

$$w_2(\varphi) = w_e(\varphi) \tag{4.22}$$

and the transverse and meridian displacements in Region $\mathcal{R}_3$ given as

$$w_3(\varphi) = w_e(\varphi), \qquad u_3(\varphi) = u_e(\varphi) \tag{4.23}$$

where the displacements with subscript e correspond to the elastic deformation associated with the myopic evolution of the intact retina.

In Eqs. (4.19)-(4.21), the parameters σ_j and τ_j correspond to the radial normal and meridian shear stress, respectively, acting on the retina in Region $\mathcal{R}_j$. They are given in terms of the applied pressures, the stress from the vitreous fibrils, and the interfacial stresses (Lagrange multipliers) as

$$\sigma_j = \hat{\sigma}_j - p_0 + \sigma_v \text{ for } j = 1 - 3 \tag{4.24}$$

where $\hat{\sigma}_1 = p_1$.

$$\tau_1 = \tau_2 = 0, \qquad \tau_3 = \hat{\tau}_3 \tag{4.25}$$

The interfacial stresses in Regions $\mathcal{R}_2$ and $\mathcal{R}_3$ can be evaluated through substitution of the analytical solutions for the displacements into the pertinent equilibrium equation.

4.2.4 Boundary Conditions

The boundary conditions for the detaching retina are also found from the variational formulation. The conditions at $\varphi = 0$ are found to be

$$u_1(0) = 0, \qquad \beta_\varphi^{(1)}(0) = 0, \qquad Q_\varphi^{(1)}(0) = 0 \tag{4.26}$$

The remaining boundary conditions depend on the existence or absence of the contact zone, Region $\mathcal{R}_2$. Although the model allows for a contact zone, one may not be physically realizable for a given detachment size and load condition, as was the case in Chapter 3. The transversality conditions, which are discussed in Section 4.2.5, determine the size and existence of the contact zone.

When a *contact zone is present*, the boundary conditions at $\varphi = \varphi_1$ and $\varphi = \varphi_2$ are

$$u_1(\varphi_1) = u_2(\varphi_1), \qquad w_1(\varphi_1) = w_e(\varphi_1), \qquad \beta_\varphi^{(1)}(\varphi_1) = \beta_\varphi^{(2)}(\varphi_1),$$
$$N_{\varphi\varphi}^{(1)}(\varphi_1) = N_{\varphi\varphi}^{(2)}(\varphi_1), \qquad u_2(\varphi_2) = u_e(\varphi_2) \tag{4.27}$$

where the displacements with subscript e correspond to the elastic deformation associated with the myopic evolution of the intact retina.

When a *contact zone is absent*, Region $\mathcal{R}_2$ does not exist and $\varphi = \varphi_2$ is taken as the boundary angle between the lift zone, $\mathcal{R}_1$, and the intact region, $\mathcal{R}_3$. In this case, the conditions stated in Eq. (4.27) are negated and the boundary conditions at $\varphi = \varphi_2$ are

$$u_1(\varphi_2) = u_e(\varphi_2), \qquad w_1(\varphi_2) = w_e(\varphi_2), \qquad \beta_\varphi^{(1)}(\varphi_2) = \beta_\varphi^{(e)}(\varphi_2) \tag{4.28}$$

where $\beta_\varphi^{(e)}$ is given by substituting w_e and u_e into Eq. (4.15).

The propagation of retinal detachment when an axisymmetric tear in the retina is present at $\varphi = 0$ with the boundary angle of the tear given at $\varphi = \varphi_0$ is also considered for the

myopic eye. In this case, the conditions stated in Eq. (4.26) at $\varphi = 0$ are negated and the boundary conditions applied at the edge of the tear, $\varphi = \varphi_0$, are

$$N_{\varphi\varphi}^{(1)}(\varphi_0) = 0, \qquad M_{\varphi\varphi}^{(1)}(\varphi_0) = 0, \qquad Q_{\varphi}^{(1)}(\varphi_0) = 0 \tag{4.29}$$

4.2.5 Transversality Conditions

The boundaries at $\varphi = \varphi_1$ and $\varphi = \varphi_2$ are not fixed. Rather, they are found as part of the solution to the mathematical problem. Allowing these parameters to vary arbitrarily when performing the variations yields the transversality conditions that establish the location of the propagating boundaries that correspond to equilibrium configurations of the detaching ocular system. The resulting transversality conditions for the myopic retina will differ in form when compared to those of the emmetropic retina in Chapter 3. Since the retina is constrained by the non-spherical geometry of the rigid outer layers of the myopic eye, the derived transversality conditions are similar in form to those of a shell with a compliant outer layer. At the contact zone and detachment boundaries, the jump in the strain energy that would cause detachment propagation is taken between the detaching retina and the elastic energy of the constrained shape of the intact retina. Two possibilities are considered: (i) a contact zone is present and (ii) a contact zone is absent.

(i) When a *contact zone is present*, the condition that establishes the location of the propagating contact zone boundary, $\varphi = \varphi_1$, is found to be

$$w_1''(\varphi_1) = w_e''(\varphi_1) \tag{4.30}$$

In addition, the condition that establishes the location of the propagating detachment boundary, $\varphi = \varphi_2$, takes the form

$$\mathcal{G}\{\varphi_2\} = \frac{1}{2R^2}\left[\left(\frac{D}{R^2} + C\right)\left\{\left(u_2'\right)^2 - \left(u_e'\right)^2\right\}\right.$$
$$\left.+ \frac{2D}{R^2}\left\{u_2'' - u_e'' + \left(u_2' - u_e'\right)\cot\varphi\right\}w_e'\right]_{\varphi=\varphi_2} = 2\gamma \tag{4.31}$$

where the function $\mathcal{G}\{\varphi_2\}$ is identified as the *energy release rate* (energy released per unit increase of the detachment angle) of the detaching retina.

(ii) When a *contact zone is absent*, Eq. (4.30) becomes invalid. For this case, $\varphi_1 = \varphi_2$ and Eq. (4.31) is superfluous. The transversality condition that establishes the detachment boundary, $\varphi = \varphi_2$, for this case is found to be given by

$$\mathcal{G}\left\{\varphi_2\right\} = \frac{1}{2R^2}\left[D\left\{\left(\beta_\varphi^{(1)'}\right)^2 - \left(\beta_\varphi^{(e)'}\right)^2\right\}\right.$$
$$\left. + C\left\{\left(u_1'\right)^2 - \left(u_e'\right)^2\right\} + 2R\left\{Q_\varphi^{(1)} - Q_\varphi^{(e)}\right\}w_1'\right]_{\varphi=\varphi_2} = 2\gamma \tag{4.32}$$

Equations (4.31) and (4.32) are associated with the following Griffith-type criterion [32]: if $\mathcal{G}\left\{\varphi^*\right\} \geq 2\gamma$ for some initial value, φ^*, of the detachment angle, φ_2, propagation of that detachment angle will occur with φ_2 increasing until the equality is satisfied. If $\mathcal{G}\left\{\varphi^*\right\} < 2\gamma$, propagation will not occur.

4.2.6 Non-dimensionalization

Thus far, all of the parameters presented in this Chapter have been given in dimensional form. In obtaining solutions to the governing equations and in presenting results, all of these parameters will be given in non-dimensional form. Non-dimensional parameters henceforth are denoted with an overbar. Length scales are non-dimensionalized with respect to the radius, R_0, of the emmetropic retina as follows;

$$\bar{R} = R/R_0, \quad \bar{w} = w/R_0, \quad \bar{u} = u/R_0, \quad \bar{h} = h/R_0, \quad \bar{a} = a/R_0, \quad \bar{b} = b/R_0 \tag{4.33}$$

The remaining parameters are non-dimensionalized with respect to the bending stiffness of the retina at a reference value, D_0, which is given in terms of the Young's modulus of the retina at a reference value, E_0. The non-dimensional stiffnesses then take the following form

$$\bar{D} = D/D_0 = E/E_0 \quad \text{and} \quad \bar{C} = CR_0^2/D_0 = 12\bar{D}/\bar{h}^2 \tag{4.34}$$

Other non-dimensional parameters include

$$\bar{\sigma} = \sigma R_0^3/D_0, \quad \bar{\tau} = \tau R_0^3/D_0, \quad \bar{\gamma} = \gamma R_0^2/D_0, \quad \bar{Q}_\varphi = Q_\varphi R_0^2/D_0,$$
$$\bar{N}_{\varphi\varphi} = N_{\varphi\varphi}R_0^2/D_0, \quad \bar{N}_{\theta\theta} = N_{\theta\theta}R_0^2/D_0, \quad \bar{M}_{\varphi\varphi} = M_{\varphi\varphi}R_0/D_0, \quad \bar{M}_{\theta\theta} = M_{\theta\theta}R_0/D_0 \tag{4.35}$$

whose interpretations follow accordingly. The general solution to the mathematical model for retinal detachment in myopic eyes follows in the next Section.

4.3   General Solution

The explicit form for the displacements of the intact retina due to the myopic changes of the outer eye that were introduced in Section 4.2.1 is presented first.

4.3.1   Influence of Myopia on the Intact Retina

As the outer eye undergoes the geometric changes associated with myopia, the intact retina will change from its emmetropic spherical shape to an ellipsoidal shape as governed by the displacements introduced in Section 4.2.1. Substitution of Eq. $(4.3)_1$ into Eq. (4.8) yields

$$R_m\left(\varphi\right) = R + w_e\left(\varphi\right) = \frac{ab}{\sqrt{a^2 \sin^2\varphi + b^2 \cos^2\varphi}} \tag{4.36}$$

where a and b are the major and minor axes of the ellipse as shown in Figure 4.1. The axes of the ellipse are further given in terms of the transverse elastic displacement of the intact retina, $w_e\left(\varphi\right)$, and the radius of the stress-free growth state, R, as

$$a = R_m\left(0\right) = R + w_e\left(0\right) \quad \text{and} \quad b = R_m\left(\pi/2\right) = R + w_e\left(\pi/2\right) \tag{4.37}$$

Substitution of Eqs. (4.37) into Eq. (4.36) yields

$$R + w_e\left(\varphi\right) = \frac{\left[R + w_e\left(0\right)\right]\left[R + w_e\left(\pi/2\right)\right]}{\sqrt{\left[R + w_e\left(0\right)\right]^2 \sin^2\varphi + \left[R + w_e\left(\pi/2\right)\right]^2 \cos^2\varphi}} \tag{4.38}$$

Then, dividing through by R in Eq. (4.38) results in

$$1 + \frac{w_e\left(\varphi\right)}{R} = \frac{\left[1 + \frac{w_e(0)}{R}\right]\left[1 + \frac{w_e(\pi/2)}{R}\right]}{\sqrt{\left[1 + \frac{w_e(0)}{R}\right]^2 \sin^2\varphi + \left[1 + \frac{w_e(\pi/2)}{R}\right]^2 \cos^2\varphi}} \tag{4.39}$$

which, when expanded, takes the form

$$1 + \frac{w_e\left(\varphi\right)}{R} = \frac{1 + \frac{w_e(0)}{R} + \frac{w_e(\pi/2)}{R} + \frac{w_e(0)w_e(\pi/2)}{R^2}}{\sqrt{\left[1 + 2\frac{w_e(0)}{R} + \frac{w_e(0)^2}{R^2}\right] \sin^2\varphi + \left[1 + 2\frac{w_e(\pi/2)}{R} + \frac{w_e(\pi/2)^2}{R^2}\right] \cos^2\varphi}} \tag{4.40}$$

The denominator of Eq. (4.40) is then expanded as a binomial series, which yields

$$1 + \frac{w_e\left(\varphi\right)}{R} = \left[1 + \frac{w_e\left(0\right)}{R} + \frac{w_e\left(\pi/2\right)}{R} + \frac{w_e\left(0\right)w_e\left(\pi/2\right)}{R^2}\right] \times$$
$$\left[1 - \left\{\frac{w_e\left(0\right)}{R} + \frac{w_e\left(0\right)^2}{2R^2}\right\}\sin^2\varphi - \left\{\frac{w_e\left(\pi/2\right)}{R} + \frac{w_e\left(\pi/2\right)^2}{2R^2}\right\}\cos^2\varphi + ...\right] \tag{4.41}$$

Next, terms of order w_e^2/R^2 are neglected in Eq. (4.41). This approximation is required for consistency with the linear thin structure theory employed for the elastic deflections of the retina in Section 4.2.1. When expanded and reduced appropriately, Eq. (4.41) reduces to the form

$$1 + \frac{w_e\left(\varphi\right)}{R} = 1 + \frac{w_e\left(0\right)}{R} + \frac{w_e\left(\pi/2\right)}{R} - \frac{w_e\left(0\right)}{R}\sin^2\varphi - \frac{w_e\left(\pi/2\right)}{R}\cos^2\varphi \qquad (4.42)$$

Regrouping terms and incorporating the relations given in Eqs. (4.37) leads to

$$w_e\left(\varphi\right) = a\cos^2\varphi + b\sin^2\varphi - R \qquad (4.43)$$

Lastly, Eq. (4.43) is non-dimensionalized with respect to the emmetropic radius, R_0, of the retina as

$$\bar{w}_e\left(\varphi\right) = \bar{a}\cos^2\varphi + \bar{b}\sin^2\varphi - \bar{R} \qquad (4.44)$$

where the non-dimensional parameters are given in Eq. (4.33).

With $\bar{w}_e\left(\varphi\right)$ established, $\bar{u}_e\left(\varphi\right)$ is found through the governing equation for the intact retina in the meridian direction, which is the same form as Eq. (4.20) for the detaching retina, when taking $\bar{\tau}_e = 0$. The governing equation for $\bar{u}_e\left(\varphi\right)$ given in terms of the known displacement $\bar{w}_e\left(\varphi\right)$ follows as

$$\bar{u}_e'' + \cot\varphi\bar{u}_e' - \left(\cot^2\varphi + \nu\right)\bar{u}_e = \frac{\bar{D}}{\bar{C}\bar{R} + \bar{D}}\left[\bar{w}_e''' + \cot\varphi\bar{w}_e'' - \left(\cot^2\varphi + \nu + \frac{\bar{C}\bar{R}\left(1+\nu\right)}{\bar{D}}\right)\bar{w}_e'\right] \qquad (4.45)$$

Upon substitution of Eq. (4.44), Eq. (4.45) reduces to the form

$$\bar{u}_e'' + \cot\varphi\bar{u}_e' - \left(\cot^2\varphi + \nu\right)\bar{u}_e = 4\lambda\cos\varphi\sin\varphi \qquad (4.46)$$

where

$$\lambda = \tfrac{1}{2}\left(\bar{a} - \bar{b}\right)\left[\frac{4\bar{D}}{\bar{C}\bar{R} + \bar{D}} + 1 + \nu\right] \qquad (4.47)$$

Equation (4.46) is subject to the symmetric boundary conditions

$$\bar{u}_e\left(0\right) = \bar{u}_e\left(\pi/2\right) = 0 \qquad (4.48)$$

Upon solving the governing differential equation, Eq. (4.46), and applying the boundary

conditions given in Eqs. (4.48), $\bar{u}_e \left(\varphi \right)$ is found as

$$\bar{u}_e \left(\varphi \right) = -\lambda \frac{\tilde{\Gamma} \left(2 - \psi_1 \right) \tilde{\Gamma} \left(2 - \psi_2 \right)}{\tilde{\Gamma} \left(\psi_1 + \psi_2 \right)} \left[\sin \varphi \cos \varphi \right] \times$$

$$\left[\tfrac{2}{3} \cos^2 \varphi \, _2F_1 \left(\psi_1, \psi_2; 2; \sin^2 \varphi \right) \, _2F_1 \left(1 - \psi_1, 1 - \psi_2; \tfrac{5}{2}; \cos^2 \varphi \right) \right. \tag{4.49}$$

$$\left. + \tfrac{1}{2} \sin^2 \varphi \, _2F_1 \left(\psi_1, \psi_2; 3; \sin^2 \varphi \right) \, _2F_1 \left(1 - \psi_1, 1 - \psi_2; \tfrac{3}{2}; \cos^2 \varphi \right) \right]$$

where

$$\psi_1 = \frac{3 - \sqrt{5 - 4\nu}}{4}, \qquad \psi_2 = \frac{3 + \sqrt{5 - 4\nu}}{4} \tag{4.50}$$

In addition, $\tilde{\Gamma}(\cdot)$ represents the gamma function and $_2F_1(\cdot)$ represents the hypergeometric function.

The final step in establishing the myopic shape of the intact retina is defining the length of the axes of the ellipse, $\bar{a}$ and $\bar{b}$. As stated in the Section 4.1, Atchison *et al.* [3] measured axial, vertical, and horizontal retinal dimensions of emmetropic and myopic eyes using MRI and found changes in dimension of 0.35 mm/D in axial length, 0.19 mm/D in height, and 0.10 mm/D in width as myopia increases. For the model presented herein, myopia is also classified by the best sphere correction and the increase in the axial length of the intact myopic retina is taken to be 0.35 mm/D as found in [3]. In order to maintain an axisymmetric model, both the height and the width of the retina are taken to increase by 0.15 mm/D, the average of the height and width increases found in [3].

Representative values for the displacements used in Eqs. (4.37) are listed in Table 4.1, where displacements have been non-dimensionalized by the radius of the retina in an emmetropic human eye with average dimensions as given in Wilkinson and Rice [84] as $R_0 = 11$ mm. Consideration is given to detachment of the retina occurring at the posterior pole of the eye as well as at the superior pole. The schematic in Figures 4.1 and 4.2 show the cross-section of the retina associated with detachment at the posterior pole. When considering detachment at the superior pole (or any other location along the equator of the eye), the displacements that are substituted into Eqs. (4.37) from Table 4.1 are interchanged.

For the myopic eye of -10 D, the displacement of major axis shown in Table 4.1 compared with the emmetropic radius exceeds 15% of the reference radius of the emmetropic retina. At this point if growth of the retina is not included ($\alpha = 0$), the model has reached the

Best sphere correction (D)	-2	-4	-6	-8	-10
Posterior $\bar{R}_m(0)$, Superior $\bar{R}_m(\pi/2)$	1.032	1.064	1.095	1.127	1.159
Posterior $\bar{R}_m(\pi/2)$, Superior $\bar{R}_m(0)$	1.014	1.027	1.041	1.055	1.068

Table 4.1: The representative shape of the major and minor axes of the intact myopic retina when non-dimensionalized with a radius of $R_0 = 11$ mm.

limits of the maximum displacement allowable when employing a small deflection model. Severe myopia is commonly considered to be greater than -6 D, so the model is applicable for the range of myopia from minor to severe.

As described earlier, the model for the ellipsoidal shape of the intact myopic retina is formed by rotating the two dimensional cross-section shown in Figures 4.1 and 4.2 about the $\varphi = 0$ axis. For detachment at the posterior pole, $\varphi = 0$ corresponds to the major axis of the two dimensional ellipse, which results in a prolate ellipsoidal shape of the intact retina in which the height and the width of the retina are the same dimensions, as desired and shown in Figure 4.3(a). This is not the case when considering detachment at the superior pole, as shown in Figure 4.3(b), since $\varphi = 0$ now corresponds to the minor axis of the two dimensional ellipse. This results in an oblate ellipsoid in which the width at the equator of the intact retina is equal to the axial length, not the height. While this is not the same shape of the myopic retina as that for detachment at the posterior pole, it cannot be avoided in the current axisymmetric model. As the displacements are small and there is large variability in the measurements of the dimensions of myopic retina, the oblate ellipsoidal shape can still yield insight into detachment propagation at the superior pole.

4.3.2 Retinal Detachment

The method for obtaining the general solution to the governing differential equations given in Eqs. (4.19)-(4.21) for the lift zone (Region $\mathcal{R}_1$) is adopted from Chapter 3. First, the resultant transverse shear force in the lift zone is found to be

$$
\begin{aligned}
\bar{Q}_\varphi^{(1)}(\varphi) &= A_1 \sin\varphi\, {}_2F_1\left(\psi_3, \psi_4; 2; \sin^2\varphi\right) + A_2 \sin\varphi\, {}_2F_1\left(\hat{\psi}_3, \hat{\psi}_4; 2; \sin^2\varphi\right) \\
&+ A_3 \sin\varphi\, G_{2,2}^{2,0}\left(\sin^2\varphi \left|\begin{array}{c} \psi_3 - \frac{1}{2}, \psi_4 - \frac{1}{2} \\ -1, 0 \end{array}\right.\right) + A_4 \sin\varphi\, G_{2,2}^{2,0}\left(\sin^2\varphi \left|\begin{array}{c} \hat{\psi}_3 - \frac{1}{2}, \hat{\psi}_4 - \frac{1}{2} \\ -1, 0 \end{array}\right.\right)
\end{aligned}
$$
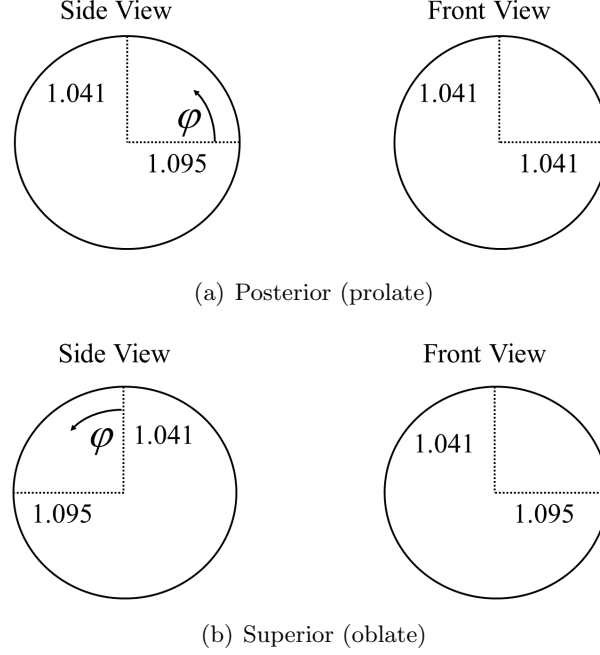
(4.51)

(a) Posterior (prolate)

(b) Superior (oblate)

Figure 4.3: Difference in the shape of the intact myopic retina of -6 D between the models for detachment in the posterior and superior regions: (a) the prolate shape when considering detachment in the posterior region and (b) the oblate shape when considering detachment in the superior region.

where

$$\psi_3 = \frac{3 + \sqrt{5 + \mathrm{i}Z}}{4}, \qquad \psi_4 = \frac{3 - \sqrt{5 + \mathrm{i}Z}}{4}, \qquad \hat{\psi}_3 = \frac{3 + \sqrt{5 - \mathrm{i}Z}}{4}, \qquad \hat{\psi}_4 = \frac{3 - \sqrt{5 - \mathrm{i}Z}}{4}$$

$$(4.52)$$

with i being the imaginary unit $\left(\sqrt{-1}\right)$ and Z given as

$$Z = 4\sqrt{\frac{\bar{C}\bar{R}^2}{\bar{D}}\left(1 - \nu^2\right) - \nu^2} \tag{4.53}$$

In Eq. (4.51), $_2F_1(\cdot)$ again represents the hypergeometric function, $G_{2,2}^{2,0}(\cdot)$ represents the Meijer G function, and A_1-A_4 are constants of integration.

The meridian and transverse displacements are then found in terms of the resultant transverse shear force in Eq. (4.51) as

$$\bar{u}_1\left(\varphi\right) = A_6 \sin\varphi - \frac{\bar{R}}{\bar{C}\left(1 - \nu\right)}\left[\bar{Q}_\varphi^{(1)} + \left(\frac{1}{2}\bar{R}\bar{\sigma}_1 + A_5\right)\left(\cot\varphi + \sin\varphi\ln\left\{\cot\frac{\varphi}{2}\right\}\right)\right] \tag{4.54}$$

and

$$\bar{w}_1\left(\varphi\right) = \frac{\bar{R}}{\bar{C}\left(1-\nu^2\right)}\left[\bar{Q}_\varphi^{(1)'} + \bar{Q}_\varphi^{(1)}\cot\varphi\right] - A_5\frac{\bar{R}}{\bar{C}\left(1-\nu\right)}\left[1 - \cos\varphi\ln\left\{\cot\frac{\varphi}{2}\right\}\right]$$
$$- A_6\cos\varphi - \frac{\bar{R}^2\bar{\sigma}_1}{\bar{C}\left(1-\nu^2\right)}\left[1 - \frac{1}{2}\left(1+\nu\right)\cos\varphi\ln\left\{\cot\frac{\varphi}{2}\right\}\right] \tag{4.55}$$

where A_5 and A_6 are additional constants of integration.

The general solution for the contact zone (Region $\mathcal{R}_2$) is not presented here. When applying the boundary conditions to the general solution for the case when a *contact zone is present* (Eqs. (4.27)), with either no tear in the retina (Eqs. (4.26)) or a tear in the retina at the origin (Eqs. (4.29)), it is found that the transversality condition given in Eq. (4.30) is not satisfied for any values of the boundary angles φ_1 and φ_2 considered. Hence, even though the model allows for a contact zone, a contact zone will not exist for the range of detachment sizes considered. Therefore, in the analysis that follows a *contact zone is absent*, so Region $\mathcal{R}_2$ does not exist and we take $\varphi = \varphi_2$ as the boundary angle between the lift zone and the intact region.

When considering detachment at the superior pole of the eye and using the values for the position of the myopic retina found in Table 4.1, the radius of the intermediate growth state, $\bar{R}$, is larger than the position of the myopic configuration of the retina at the pole, $\bar{R}_0 + \bar{w}_G\left(0\right)$, for larger values of the growth parameter, α. As a result, in the absence of applied stress to the retina, $\bar{\sigma}_1 = 0$, as the growth parameter approaches one, there will reach a value of α for which the only physically realizable position of the detaching retina is a full contact zone in which Region $\mathcal{R}_1$ is not present due to the linear strain-displacement relations employed in this model. As biochemical growth is believed to play a small part in the deformation of the retina during the evolution of myopia ([28], [45], [66]), larger values of the growth parameter are not relevant. Hence, we only consider values of the growth parameter at the superior pole for which Region $\mathcal{R}_1$, the lift zone, is present.

Case 1: No retinal tear present

In applying boundary conditions for Region $\mathcal{R}_1$, detachment of the retina at both the posterior and superior poles of the eye is considerd when no tear in the retina is present. The Meijer G function, along with the cotangent function and natural logarithm, are singular at the origin but, on physical grounds, the deflections at the origin must be finite. Therefore,

at both ocular locations, the boundary conditions of finite deflection at $\varphi = 0$ are applied in place of Eqs. (4.26). This results in the values

$$A_3 = 0, \quad A_4 = 0, \quad A_5 = -\bar{R}\bar{\sigma}_1/2 \tag{4.56}$$

Imposing the boundary conditions for the case of *no contact zone* given in Eqs. (4.28) allows for solution of the remaining integration constants A_1, A_2, and A_6, as

$$\left\{ \begin{array}{c} A_1 \\ A_2 \\ A_6 \end{array} \right\} = [\lambda_1]^{-1} \left\{ \begin{array}{c} \frac{\bar{C}}{R}\bar{w}_e\left(\varphi_2\right)\left(1 - \nu^2\right) + \frac{1}{2}\bar{R}\bar{\sigma}_1\left(1 - \nu\right) \\ -\frac{\bar{C}}{R}\bar{w}'_e\left(\varphi_2\right)\left(1 - \nu^2\right)\csc\varphi_2 \\ -\frac{\bar{C}}{R}\bar{u}_e\left(\varphi_2\right)\left(1 - \nu\right)\csc\varphi_2 \end{array} \right\} \tag{4.57}$$

where

$$[\lambda_1] = \begin{bmatrix} \cos\varphi_2 X_1\left(\psi_a, \psi_b, \varphi_2\right) & \cos\varphi_2 X_1\left(\hat{\psi}_a, \hat{\psi}_b, \varphi_2\right) & -\frac{\bar{C}}{R}\cos\varphi_2\left(1 - \nu^2\right) \\ X_2\left(\psi_a, \psi_b, \varphi_2\right) & X_2\left(\hat{\psi}_a, \hat{\psi}_b, \varphi_2\right) & -\frac{\bar{C}}{R}\left(1 - \nu^2\right) \\ {}_2F_1\left(\psi_a, \psi_b; 2; \sin^2\varphi_2\right) & {}_2F_1\left(\hat{\psi}_a, \hat{\psi}_b; 2; \sin^2\varphi_2\right) & -\frac{\bar{C}}{R}\left(1 - \nu\right) \end{bmatrix} \tag{4.58}$$

$$X_1\left(\psi_a, \psi_b, \varphi\right) = 2\,{}_2F_1\left(\psi_a, \psi_b; 2; \sin^2\varphi\right) + \psi_a\psi_b\sin^2\varphi\,{}_2F_1\left(\psi_a + 1, \psi_b + 1; 3; \sin^2\varphi\right) \tag{4.59}$$

$$X_2\left(\psi_a, \psi_b, \varphi\right) = 2\,{}_2F_1\left(\psi_a, \psi_b; 2; \sin^2\varphi\right) + \left(1 - 5\cos^2\varphi\right)\psi_a\psi_b\,{}_2F_1\left(\psi_a + 1, \psi_b + 1; 3; \sin^2\varphi\right)$$
$$- \tfrac{2}{3}\sin^2\varphi\cos^2\varphi\psi_a\psi_b\left(\psi_a + 1\right)\left(\psi_b + 1\right)\,{}_2F_1\left(\psi_a + 2, \psi_b + 2; 4; \sin^2\varphi\right) \tag{4.60}$$

Case 2: Retinal tear present

Retinal detachment at the superior pole of the eye is considered with a tear/hole in the retina present at the origin. For this case, the pertinent boundary conditions are found in Eqs. (4.28) and (4.29), which yields the integration constants A_1-A_6 as

$$\left\{ \begin{array}{c} A_1 \\ A_2 \\ A_3 \\ A_4 \\ A_5 \\ A_6 \end{array} \right\} = [\lambda_2]^{-1} \left\{ \begin{array}{c} \frac{\bar{C}}{R}\bar{w}_e\left(\varphi_2\right)\left(1 - \nu^2\right) + \bar{R}\bar{\sigma}_1\left[\sec\varphi_2 - \tfrac{1}{2}\left(1 + \nu\right)g\left(\varphi_2\right)\right] \\ -\frac{\bar{C}}{R}\bar{w}'_e\left(\varphi_2\right)\left(1 - \nu^2\right)\csc\varphi_2 - \tfrac{1}{2}\bar{R}\bar{\sigma}_1\left(1 + \nu\right)\hat{g}\left(\varphi_2\right) \\ -\frac{\bar{C}}{R}\bar{u}_e\left(\varphi_2\right)\left(1 - \nu\right)\csc\varphi_2 - \tfrac{1}{2}\bar{R}\bar{\sigma}_1\hat{g}\left(\varphi_2\right) \\ 0 \\ -\tfrac{1}{2}\bar{R}\bar{\sigma}_1\cot\varphi_0\csc\varphi_0 \\ 0 \end{array} \right\} \tag{4.61}$$

where

$$
[\lambda_2] =
\begin{bmatrix}
X_1\left(\psi_a,\psi_b,\varphi_2\right) & X_1\left(\hat{\psi}_a,\hat{\psi}_b,\varphi_2\right) & Y_1\left(\psi_a,\psi_b,\varphi_2\right) & Y_1\left(\hat{\psi}_a,\hat{\psi}_b,\varphi_2\right) & -\tilde{g}\left(\varphi_2\right) & -\frac{\bar{C}}{R}\left(1-\nu^2\right) \\
X_2\left(\psi_a,\psi_b,\varphi_2\right) & X_2\left(\hat{\psi}_a,\hat{\psi}_b,\varphi_2\right) & Y_2\left(\psi_a,\psi_b,\varphi_2\right) & Y_2\left(\hat{\psi}_a,\hat{\psi}_b,\varphi_2\right) & (1+\nu)\,\hat{g}\left(\varphi_2\right) & -\frac{\bar{C}}{R}\left(1-\nu^2\right) \\
F\left(\psi_a,\psi_b,\varphi_2\right) & F\left(\hat{\psi}_a,\hat{\psi}_b,\varphi_2\right) & G\left(\psi_a,\psi_b,\varphi_2\right) & G\left(\hat{\psi}_a,\hat{\psi}_b,\varphi_2\right) & \hat{g}\left(\varphi_2\right) & -\frac{\bar{C}}{R}\left(1-\nu\right) \\
F\left(\psi_a,\psi_b,\varphi_0\right) & F\left(\hat{\psi}_a,\hat{\psi}_b,\varphi_0\right) & G\left(\psi_a,\psi_b,\varphi_0\right) & G\left(\hat{\psi}_a,\hat{\psi}_b,\varphi_0\right) & 0 & 0 \\
F\left(\psi_a,\psi_b,\varphi_0\right) & F\left(\hat{\psi}_a,\hat{\psi}_b,\varphi_0\right) & G\left(\psi_a,\psi_b,\varphi_0\right) & G\left(\hat{\psi}_a,\hat{\psi}_b,\varphi_0\right) & \sec\varphi_0\csc^2\varphi_0 & 0 \\
X_3\left(\psi_a,\psi_b,\varphi_0\right) & X_3\left(\hat{\psi}_a,\hat{\psi}_b,\varphi_0\right) & Y_3\left(\psi_a,\psi_b,\varphi_0\right) & Y_3\left(\hat{\psi}_a,\hat{\psi}_b,\varphi_0\right) & 0 & 0
\end{bmatrix}
\tag{4.62}
$$

$$
F\left(\psi_a,\psi_b,\varphi\right) = {}_2F_1\left(\psi_a,\psi_b;2;\sin^2\varphi\right)
\tag{4.63}
$$

$$
G\left(\psi_a,\psi_b,\varphi\right) = G_{2,2}^{2,0}\left(\sin^2\varphi \left|\begin{array}{c} \psi_a-\frac{1}{2},\psi_b-\frac{1}{2} \\ -1,0 \end{array}\right.\right)
\tag{4.64}
$$

$$
Y_1\left(\psi_a,\psi_b,\varphi\right) = 2G\left(\psi_a,\psi_b,\varphi\right) + \tan\varphi\, G'\left(\psi_a,\psi_b,\varphi\right)
\tag{4.65}
$$

$$
Y_2\left(\psi_a,\psi_b,\varphi\right) = 2G\left(\psi_a,\psi_b,\varphi\right) - 3\cot\varphi\, G'\left(\psi_a,\psi_b,\varphi\right) - G''\left(\psi_a,\psi_b,\varphi\right)
\tag{4.66}
$$

$$
\begin{aligned}
X_3\left(\psi_a,\psi_b,\varphi\right) = & \left(1-\nu^2\right) {}_2F_1\left(\psi_a,\psi_b;2;\sin^2\varphi\right) \\
& + \left(16\sin^2\varphi - 4\nu\cos^2\varphi - 4\right)\psi_a\psi_b\, {}_2F_1\left(\psi_a+1,\psi_b+1;3;\sin^2\varphi\right) \\
& - \tfrac{2}{3}\sin^2\varphi\left[(10+\nu)\cos^2\varphi - 3\right]\psi_a\psi_b\left(\psi_a+1\right)\left(\psi_b+1\right){}_2F_1\left(\psi_a+2,\psi_b+2;4;\sin^2\varphi\right) \\
& - \tfrac{1}{3}\sin^4\varphi\cos^2\varphi\,\psi_a\psi_b\left(\psi_a+1\right)\left(\psi_b+1\right)\left(\psi_a+2\right)\left(\psi_b+2\right){}_2F_1\left(\psi_a+3,\psi_b+3;5;\sin^2\varphi\right)
\end{aligned}
\tag{4.67}
$$

$$
\begin{aligned}
Y_3\left(\psi_a,\psi_b,\varphi\right) = & \left(1-\nu^2\right)G\left(\psi_a,\psi_b,\varphi\right) + \left[(4-\nu)\tan\varphi - 3\nu\cot\varphi\right]G'\left(\psi_a,\psi_b,\varphi\right) \\
& - (4+\nu)\,G''\left(\psi_a,\psi_b,\varphi\right) - \tan\varphi\, G'''\left(\psi_a,\psi_b,\varphi\right)
\end{aligned}
\tag{4.68}
$$

$$
g\left(\varphi\right) = \ln\left\{\cot\frac{\varphi}{2}\right\}, \qquad \hat{g}\left(\varphi\right) = \cot\varphi\csc\varphi + g\left(\varphi\right), \qquad \tilde{g}\left(\varphi\right) = (1+\nu)\left[\sec\varphi - g\left(\varphi\right)\right]
\tag{4.69}
$$

The solutions obtained in this section are used to perform simulations of the evolution of retinal detachment in the myopic eye, the results of which are presented in Section 4.4.

4.4   Results and Discussion

In this section, results are presented for retinal detachment at the posterior pole of the eye without a tear present in the retina. Results for the posterior pole are calculated using a non-dimensional retinal thickness of $\bar{h} = 0.185/11 = 0.01682$ as $h = 0.185$ mm is the average of the midperiphery and posterior retinal thicknesses as discussed in Section 3.4. Additional results are presented for detachment at the superior pole (or any position along

the equator of the eye) with and without a tear in the retina present. Results for the superior pole are calculated using a non-dimensional retinal thickness of $\bar{h} = 0.1/11 = 0.00909$ as $h = 0.1$ mm is periphery retinal thicknesses as discussed in Section 3.4. All results, at both locations, employ a Poisson's ratio of $\nu = 0.49$, as biological tissues are considered to be nearly incompressible.

The displacement profiles for the detaching retina in the absence of applied stress ($\bar{\sigma}_1 = 0$) are considered in order to isolate the effects of the change in shape of the myopic retina on detachment. The transverse position of the detaching retina at the posterior pole is shown in the polar plot displayed in Figure 4.4(a), while the corresponding meridian displacement profile appears in the cartesion plot in Figure 4.4(b). In Figure 4.4(a), the location of the emmetropic retina and the location of the myopic RPE are shown for reference, while in Figure 4.4(b) the elastic meridian displacement of the fully intact retina is shown. In comparing the results for a detachment size of $\varphi_2 = 0.270$, it is seen that the displacement is smaller when a growth parameter of $\alpha = 0.5$ is prescribed when compared to that of $\alpha = 0$ since the retina stores less elastic strain energy during its myopic evolution for $\alpha = 0.5$. At the posterior, the largest detachment size shown is $\varphi_2 = 0.270$, as the optic nerve, with its location as discussed in Section 3.4, would break the axisymmetric nature of the detachment for larger detachment sizes.

Displacement profiles for detachment at the superior pole of the eye without a tear in the retina and with a tear in the retina are shown in Figures 4.5 and 4.6, respectively. Here, the largest detachment size shown is $\varphi_2 = 0.45$, as the ora serrata, with its location as discussed in Section 3.4, would break the axisymmetric nature of the detachment for larger detachment sizes. The qualitative behavior for the displacement profiles at the superior pole is similar to that of profiles at the posterior pole in Figure 4.4. In Figures 4.5(a) and 4.6(a), we see 'dimpling' in the retina for larger detachment sizes as was observed when studying retinal detachment in emmetropic eyes in Chapter 3. If the optic nerve were not present, similar 'dimpling' would occur for larger detachment sizes at the posterior pole as well. In Figures 4.4(b), 4.5(b), and 4.6(b), the meridian displacement of the intact retina is the same for $\alpha = 0$ and $\alpha = 0.5$ due to the membrane stiffness $\bar{C}$ in the denominator of Eq. (4.47), which is large in magnitude, controlling the value of λ.
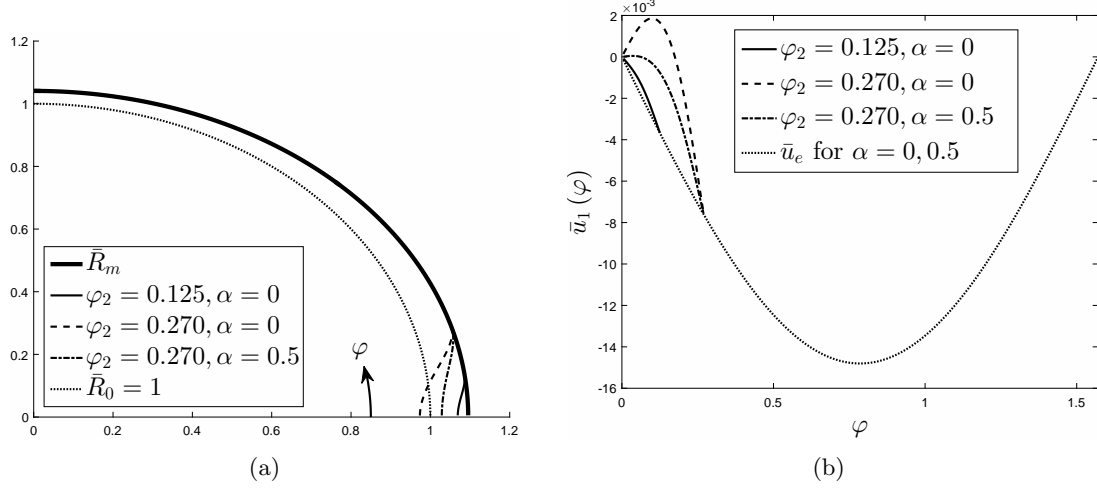
Figure 4.4: The deflection profile for detachment of the retina at the posterior pole of the myopic eye of -6 D with $\nu = 0.49$, $\bar{D} = 1$, $\bar{h} = 0.185/11 = 0.01682$, and $\bar{\sigma}_1 = 0$: (a) the transverse location of the retina compared to the myopic outer eye and the emmetropic eye and (b) the meridian displacement profile.

The *energy release rate* (ERR) for the case where a contact zone is absent, Eq. (4.32), is given in non-dimensional form as

$$\bar{\mathcal{G}}\left\{\varphi_2\right\} = \frac{1}{2\bar{R}^2}\left[\bar{D}\left\{\left(\beta_\varphi^{(1)'}\right)^2 - \left(\beta_\varphi^{(e)'}\right)^2\right\} \right.$$
$$\left. + \bar{C}\left\{\left(\bar{u}_1'\right)^2 - \left(\bar{u}_e'\right)^2\right\} + 2\bar{R}\left\{\bar{Q}_\varphi^{(1)} - \bar{Q}_\varphi^{(e)}\right\}\bar{w}_1'\right]_{\varphi=\varphi_2} = 2\bar{\gamma} \tag{4.70}$$

Both $\bar{\mathcal{G}}\left\{\varphi_2\right\}$ and $2\bar{\gamma}$ are normalized with respect to D_0, which is a parameter dependent on the thickness of the retina. As the thickness of the retina varies between the posterior and superior detachment locations, the ERR must be rescaled in order to directly compare the results between the two detachment locations. Hence, results are displayed in terms of

$$\tilde{\mathcal{G}}\left\{\varphi_2\right\} = \left(\frac{h}{h_0}\right)^3 \bar{\mathcal{G}}\left\{\varphi_2\right\} \quad \text{and} \quad \tilde{\gamma} = \left(\frac{h}{h_0}\right)^3 \bar{\gamma} \tag{4.71}$$

where h remains the thickness of the retina at the location of interest and $h_0 = 0.1$ is a nominal reference value. In this sense, the normalized and the rescaled values are the same at the superior of the eye and the values at the posterior are then directly comparable to the values at the superior.

The rescaled ERR is presented in Figures 4.7-4.9 as a function of detachment size for detachment at the posterior pole, detachment at the superior pole without a tear in the
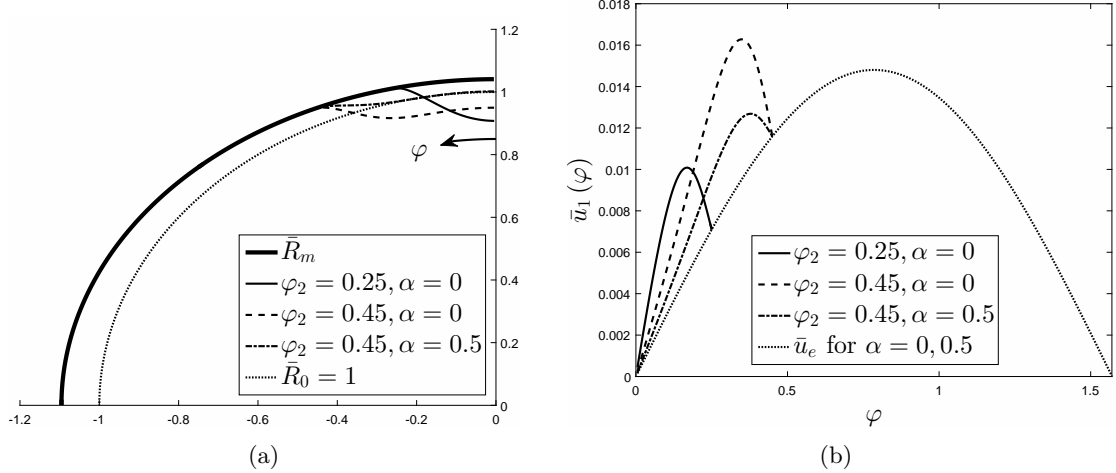
Figure 4.5: The deflection profile for detachment of the retina at the superior pole of the myopic eye of -6 D with $\nu = 0.49$, $\bar{D} = 1$, $\bar{h} = 0.1/11 = 0.00909$, and $\bar{\sigma}_1 = 0$: (a) the transverse location of the retina compared to the myopic outer eye and the emmetropic eye and (b) the meridian displacement profile.

retina, and detachment at the superior pole with a tear in the retina, respectively, all in the absence of applied stress acting on the retina ($\bar{\sigma}_1 = 0$). This again allows for isolation of the stored strain energy in the retina due solely to its change in shape during the evolution of myopia and the corresponding release of that strain energy during retinal detachment propagation. The ERR results from Eqs. (4.70) and (4.71) are shown in Figures (4.7)-(4.9) along with a horizontal line that gives the magnitude of the ERR required to produce a unit area of detachment ($2\tilde{\gamma}$). When $\tilde{\mathcal{G}}\{\varphi_2\} \geq 2\tilde{\gamma}$, the strain energy in the retina is sufficient to produce retinal detachment propagation.

For detachment at the posterior pole, we see from Figure 4.7(a) that, even in the absence of applied stress, the retina reaches a sufficient detachment energy for detachment propagation at -6 D of myopia when there is no biochemical induced growth in the retina. Figure 4.7(b) shows that at -6 D, if biochemical induced growth is present, the ERR decreases with an increasing growth parameter. The gray scale background in Figure 4.7 beginning at $\varphi_2 = 0.27$ represents the detachment size for which the presence of the optic nerve may begin to break the axisymmetric nature of the detachment shape.

For detachment at the superior pole without a tear in the retina and without biochemical growth, Figure 4.8(a), it is seen that a myopic eye of -8 D achieves sufficient energy release
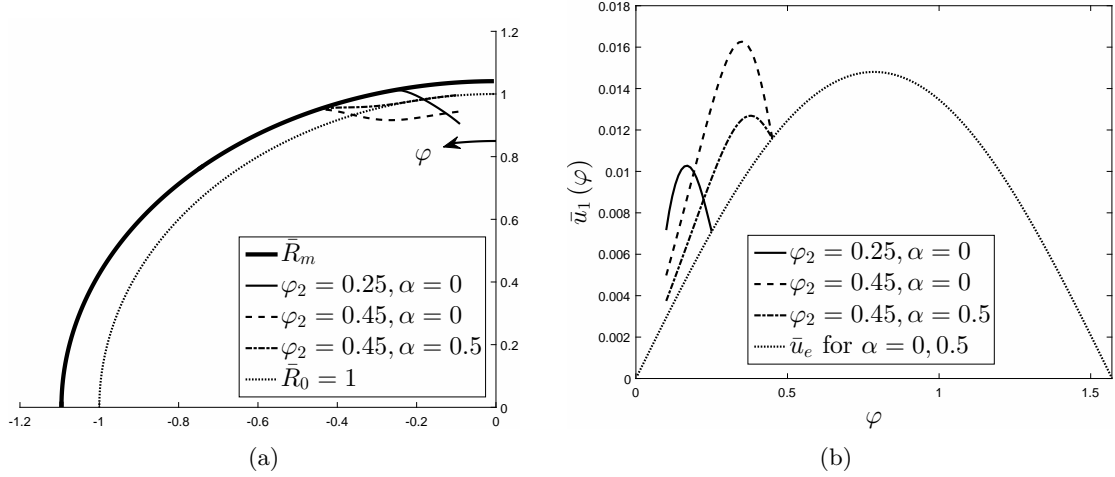
Figure 4.6: The deflection profile for detachment of the retina at the superior pole of the myopic eye of -6 D with a tear/hole of $\varphi_0 = 0.1$ and $\nu = 0.49$, $\bar{D} = 1$, $\bar{h} = 0.1/11 = 0.00909$, and $\bar{\sigma}_1 = 0$: (a) the transverse location of the retina compared to the myopic outer eye and the emmetropic eye and (b) the meridian displacement profile.

for detachment propagation. This occurs at a much larger detachment size when compared to the -6 D eye at the posterior pole in Figure 4.7(a). At all levels of myopia, the ERR is larger at the posterior pole in Figure 4.7(a) when compared to that of the same degree of myopia at the superior pole in Figure 4.8(a). The gray scale background in Figure 4.8 beginning at $\varphi_2 = 0.45$ represents the point at which the presence of the ora serrata may disrupt the axisymmetry of the detachment shape. Figure 4.8(b) again shows that increasing the growth parameter will decrease the ERR. For the superior pole, the largest growth parameter considered is $\alpha = 0.66$ since the linear model predicts a full contact zone solution at the superior pole as α approaches one. For the full contact zone solution, the ERR would be governed by Eq. (4.31), which is identically zero for this model with a full contact zone and no applied stress, and would not lead to detachment propagation.

When considering the influence of a tear in the retina on the ERR for detachment at the superior pole, Figure 4.9, similar qualitative and quantitative behavior to the results shown in Figure 4.8(a) are seen when sufficiently far from the tear. This is also shown to be independent of the size of the tear. Hence, the presence of a tear has a very localized effect on the ERR.

Finally, the effects of the applied stress on the retina, $\bar{\sigma}_1$, are combined with the effects of
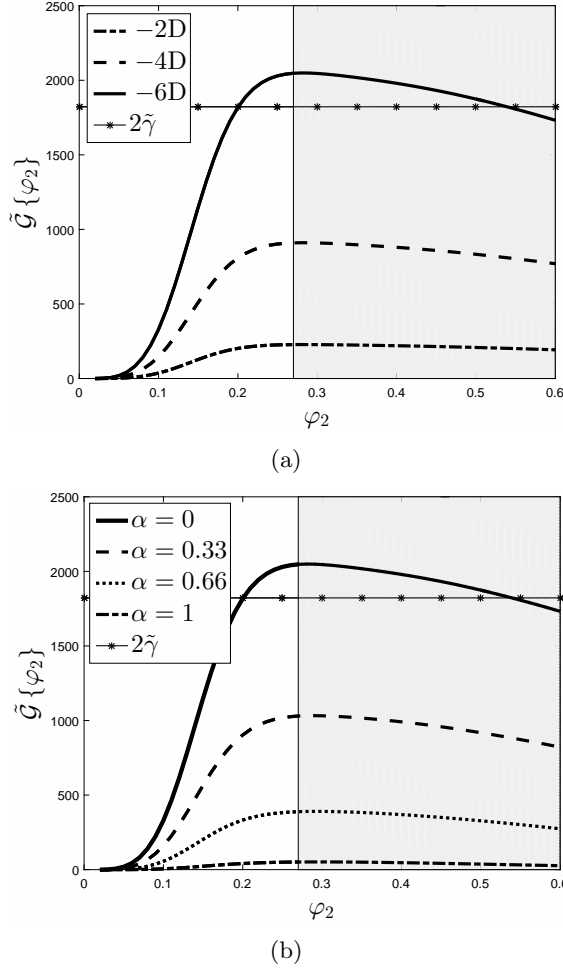
(a)

(b)

Figure 4.7: The *energy release rate* for propagation of retinal detachment at the posterior pole of the eye with $\nu = 0.49$, $\bar{D} = 1$, $\bar{h} = 0.185/11 = 0.01682$, $\bar{\gamma} = 143.9$, and $\bar{\sigma}_1 = 0$: (a) $\alpha = 0$ with various degrees of myopia (b) myopic eye of -6 D with various values of α.

the geometric changes associated with myopia to examine the critical stress for detachment propagation. The critical stress, $\bar{\sigma}_{cr}$, is found by solving Eq. (4.70) for the stress at which the ERR is equal to $2\bar{\gamma}$. This represents the critical threshold value of the applied stress for which detachment would begin to propagate. The critical stress results are also presented in rescaled form to facilitate comparison between the critical stress at the posterior and at the superior of the eye. Hence,

$$\tilde{\sigma}_{cr} = \left(\frac{h}{h_0}\right)^3 \bar{\sigma}_{cr} \tag{4.72}$$

where h and h_0 are defined in the same manner as in Eq. (4.71). A study of the critical stress for the myopic eye also allows for comparison to the critical stress for detachment
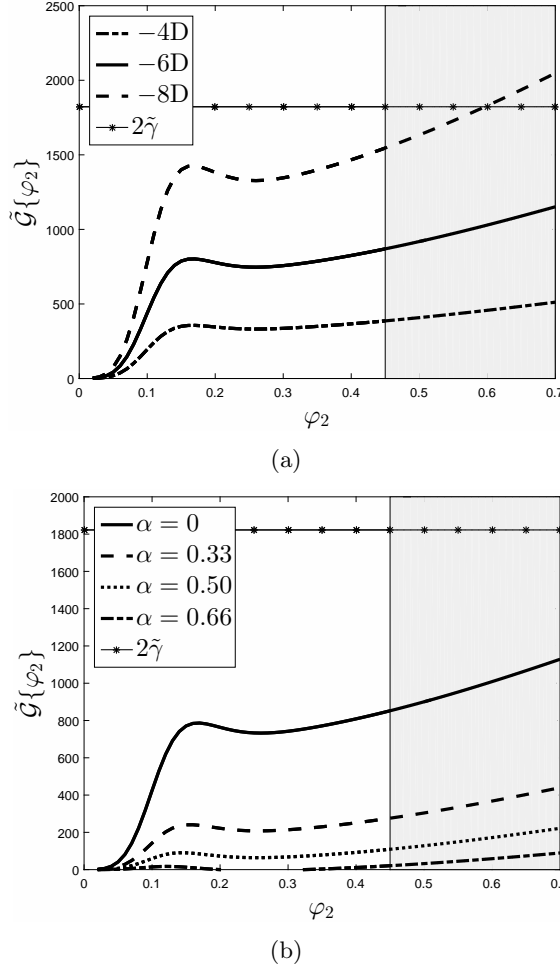
Figure 4.8: The *energy release rate* for propagation of retinal detachment at the superior pole of the eye with $\nu = 0.49$, $\bar{D} = 1$, $\bar{h} = 0.1/11 = 0.00909$, $\bar{\gamma} = 911.2$, and $\bar{\sigma}_1 = 0$: (a) $\alpha = 0$ with various degrees of myopia (b) myopic eye of -6 D with various values of α.

propagation of the retina in the emmetropic eye, found in Chapter 3.

In studying the results of the critical stress threshold paths, it is of interest to determine whether the detachment process will propagate in a stable or unstable manner ([12], [42]). If the path is monotonically increasing, then an incremental increase in stress will produce an increment in detachment size, so detachment propagation is stable. If the path is in the form of a U-shape, initially decreasing with detachment angle and then increasing, when the stress achieves a critical value for a given detachment angle on the descending portion of the path, detachment will occur in an unstable manner at a constant stress level. In this case, detachment will progress dynamically, represented by a horizontal jump to the
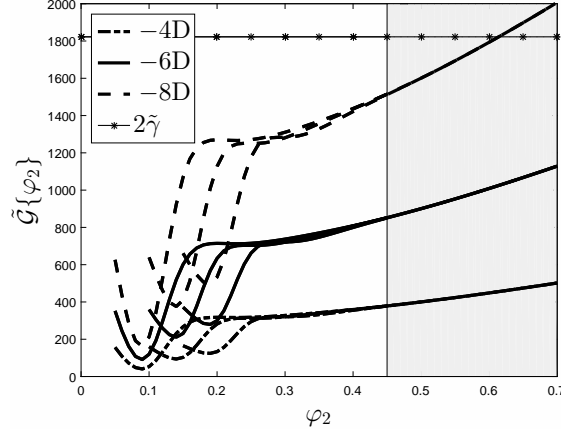
Figure 4.9: The *energy release rate* for propagation of retinal detachment at the superior pole of the eye with tears/holes of $\varphi_0 = 0.05$, $\varphi_0 = 0.1$, and $\varphi_0 = 0.15$ with $\alpha = 0$, $\nu = 0.49$, $\bar{D} = 1$, $\bar{h} = 0.1/11 = 0.00909$, $\bar{\gamma} = 911.2$, and $\bar{\sigma}_1 = 0$.

corresponding equilibrium configuration on the increasing segment of the path. Subsequent propagation along the increasing segment will be stable as an increment in stress will produce an increment in detachment angle. If the threshold path is monotonically decreasing, then once the critical stress level is achieved for a given detachment angle, it is achieved for all subsequent angles at that stress level. As a result, detachment will propagate in an unstable and catastrophic manner.

The critical stress for detachment at the posterior is shown for the case of no biochemical induced growth of the retina in Figure 4.10(a). When compared to the emmetropic retina, the degree of myopia significantly reduces the critical stress necessary for detachment propagation. At -6 D, the critical stress is seen to be zero for a detachment size around $\varphi_2 \approx 0.2$, since geometric changes alone are sufficient to produce detachment propagation at this refractive error, as shown in Figure 4.7(a). The influence of myopia is also seen to transform the catastrophic nature of the detachment of the emmetropic retina to unstable but non-catastrophic propagation for a range of detachment sizes as myopia increases. However, the right bound of the unstable well in the threshold path for -4 D and -6 D occurs beyond the detachment size for which the optic nerve would affect the axisymmetric results. For the -6 D myopic eye in Figure 4.10(b), as the growth parameter increases, the critical stress also increases. When $\alpha = 1$, the critical stress remains lower than that of the emmetropic retina, but the threshold path now has a large well for unstable propagation rather than
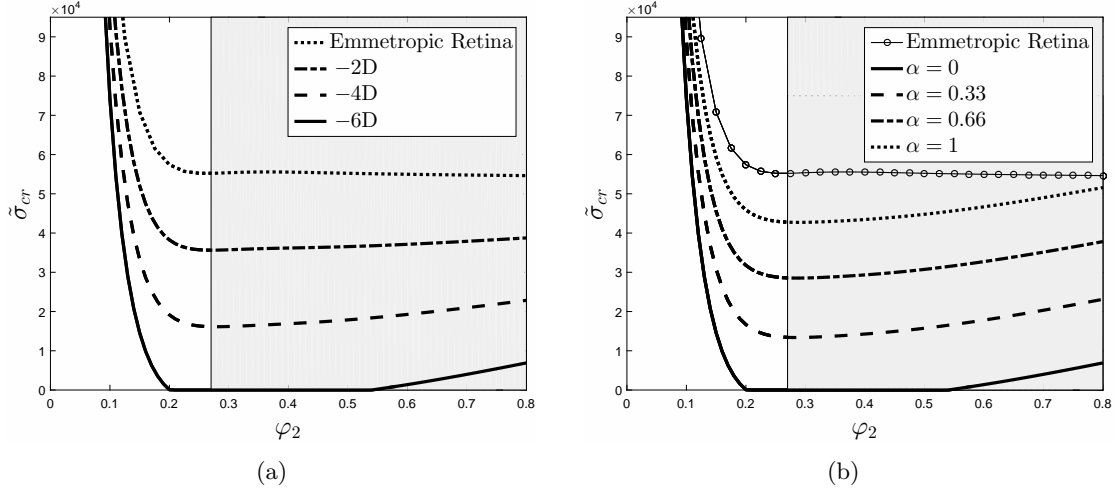
displaying entirely catastrophic propagation.

Figure 4.10: The critical stress for propagation of retinal detachment at the posterior pole of the eye with $\nu = 0.49$, $\bar{D} = 1$, $\bar{h} = 0.185/11 = 0.01682$, and $\bar{\gamma} = 143.9$: (a) $\alpha = 0$ with various degrees of myopia (b) myopic eye of -6 D with various values of α.

The results for the critical stress at the superior pole without a tear in the retina are shown in Figure 4.11. Figure 4.11(a) shows that as myopia increases the critical stress decreases and remains catastrophic in nature when compared to the emmetropic retina. As with the posterior pole, as the growth parameter increases so too does the critical stress in Figure 4.11(b). For $\alpha = 1$, the critical stress for the -6 D eye is higher than the emmetropic case for smaller detachment sizes because the applied stress in this case must first overcome the interfacial stress that would be associated with the full contact zone solution that develops as α approaches one at the superior pole.

The critical stress at the superior pole for retinas with tears of various sizes is shown in Figure 4.12. Tears in the myopic retina are seen to result in the formation of an unstable well in the threshold path for which unstable but non-catastrophic propagation is possible. This is consistent with the results of Chapter 3, in which unstable wells were found in the threshold paths for the emmetropic retina possessing a tear. As with the other results of this study concerning a tear in the retina, the size of the tear does not affect the behavior of the critical stress for detachment sizes sufficiently larger than the size of the tear itself.

In comparing Figsures 4.10(a) and 4.11(a), the critical stress in the emmetropic eye
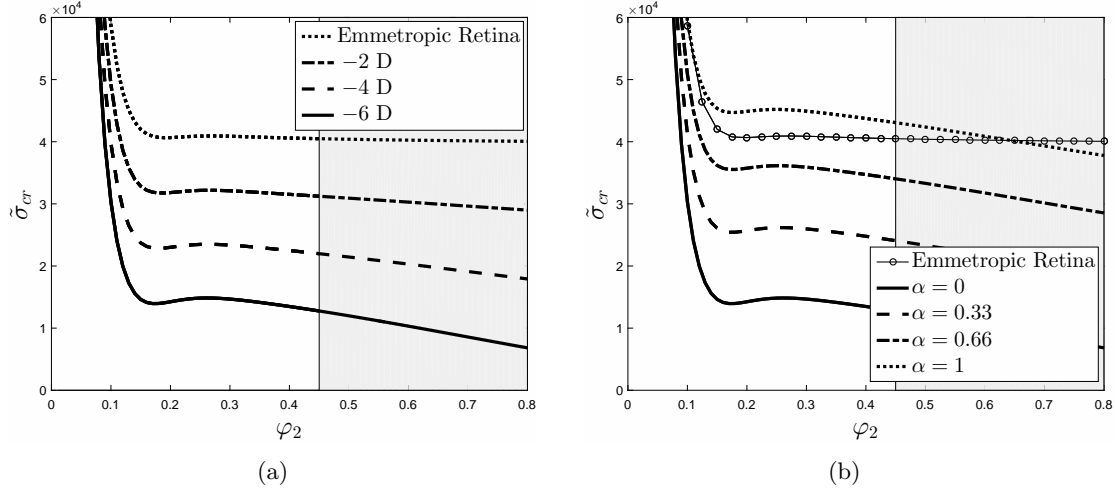
Figure 4.11: The critical stress for propagation of retinal detachment at the superior pole of the eye with $\nu = 0.49$, $\bar{D} = 1$, $\bar{h} = 0.1/11 = 0.00909$, and $\bar{\gamma} = 911.2$: (a) $\alpha = 0$ with various degrees of myopia (b) myopic eye of -6 D with various values of α.

is larger at the posterior pole than at the superior pole, where the only parameter that is different between these locations for the emmetropic eye is the thickness of the retina. As myopia reaches -2 D, the critical stress is of similar value at the two locations. Then as myopia continues to increase the critical stress for detachment propagation is lower in magnitude at the posterior pole for the same degree of myopia. Hence, the geometric changes associated with myopia that are occurring at the posterior pole affect the resistance to detachment of the retina in a much more severe manner than the geometric changes at the superior pole. However, the influence of myopia at the posterior pole shows some stabilizing wells in the critical stress threshold path, while detachment at the superior pole remains entirely catastrophic in nature.

4.5   Conclusions

A mechanics-based mathematical model of retinal detachment due to the geometric changes of the eye associated with the evolution of myopia has been developed. The model includes deformation of the retina due to biological growth of the retina, as well as elastic deformation imposed on the retina by the myopic change in shape of the much stiffer choroid and sclera. The problem was formulated as a propagating boundary value problem in the calculus
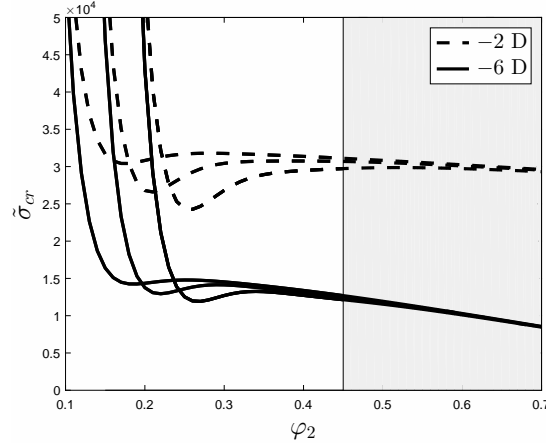
Figure 4.12: The critical stress for propagation of retinal detachment at the superior pole of the eye with tears/holes of $\varphi_0 = 0.05$, $\varphi_0 = 0.1$, and $\varphi_0 = 0.15$ with $\alpha = 0$, $\nu = 0.49$, $\bar{D} = 1$, $\bar{h} = 0.1/11 = 0.00909$, and $\bar{\gamma} = 911.2$.

of variations, which yields self-consistent governing equations, boundary conditions, and transversality conditions that establish the location of the propagating boundaries that correspond to equilibrium configurations of the detaching ocular system. Axisymmetric conditions are considered, and exact, analytical solutions to the corresponding boundary value problem were obtained for detaching retinas with and without a tear in the retina.

The results support the clinical finding of an increased prevalence of retinal detachment in myopic eyes and provide insight into the potential causation for the increased prevalence. From analysis of the *energy release rate*, it was seen that at severe levels of myopia, even in the absence of applied stress acting on the retina, a sufficient energy release for detachment propagation was achieved at both locations. Correspondingly, the critical stress for detachment propagation was found to be lower for the myopic retina when compared to that of the emmetropic retina at both locations. For the critical stress at the posterior pole, the evolution of myopia led to the development of unstable wells in the threshold paths, indicating that although detachment is more likely, it may not occur in as catastrophic a manner for this case. The results suggest that, for the emmetropic eye detachment is more resistant to propagation as one moves in a posterior direction from the equator but that due to the geometric changes associated with myopia, the myopic retina is far less resistant to detachment propagation moving posterior from the equator of the eye. As macular retinal

detachment can lead to permanent vision loss, this has severe clinical consequences.

Chapter 5

Concluding Remarks

A multi-directional growth law for layered shell structures was presented. Shells with a compliant inner layer separating from a rigid outer layer were considered and the delamination boundary between layers was allowed to take on an arbitrary shape. Subsequently, a mechanics based mathematical model for retinal detachment in the emmetropic eye that takes contraction of the vitreous and extension of its fibrils, along with a pressure difference across the retina, as the impetus for detachment propagation was presented. In the model for the emmetropic eye, retinal detachment propagation is governed by the growth law derived for layered shells. A second mechanics based mathematical model for retinal detachment due to the geometric changes of the eye associated with the evolution of myopia was developed. The model for retinal detachment in the myopic eye includes deformation of the retina due to biological growth of the retina, as well as elastic deformation imposed on the retina by the myopic change in shape of the much stiffer choroid and sclera. The latter of which acts as an additional impetus for retinal detachment in the myopic eye.

The mathematical models for both the emmetropic eye and the myopic eye were formulated as propagating boundary value problems in the calculus of variations, which yielded the self-consistent governing equations, boundary conditions, and transversality conditions that establish the location of the propagating boundaries that correspond to equilibrium configurations of each of the detaching ocular systems. Axisymmetric conditions were considered and exact analytical solutions to the corresponding boundary value problems were obtained for detaching retinas with and without a tear. Simulations based on the analytical solutions were performed, revealing the characteristic critical conditions for detachment propagation. The effects of changes in material and geometric parameters, as well as the influence of the presence and size of the retinal tear on detachment propagation was also

studied.

For the emmetropic eye, exact, analytical solutions for the radial displacements, and the corresponding meridian displacements, were obtained for detaching retinas with a central tear, as well as for retinas without a tear. The resulting characteristic detachment behavior was compared to the results of Bottega *et al.* [12], in which the meridian displacements were treated as negligible and approximate solutions to the governing equations based on that assumption were obtained. For both the case of a tear in the retina and no tear in the retina, it was seen that including the meridian displacements resulted in a substantial percentage increase in the magnitude of the radial deflection profile. However, the qualitative behavior of the radial deflection profile remained similar, with 'dimpling' in the retina occurring for larger detachment angles. The meridian deflection profile was seen to be an order of magnitude smaller than that of the radial deflection profile, but its inclusion was seen to have significant effects on the critical behavior of detachment propagation.

The threshold path for the applied effective stress showed that detachment propagation is catastrophic in nature, which is in agreement with the results of Bottega *et al.* [12], as well as with clinical observations. The inclusion of the meridian displacement was seen to lower the critical stress as well as to facilitate the development of unstable 'wells' in the threshold paths. When compared to the results of Bottega *et al.* [12], the unstable 'wells' were seen to develop at smaller tear sizes and were larger in depth and breadth for a given tear size. When compared to retinas without a tear it was seen that, for detachment angles outside but less than those that fall within the 'well', the presence of the tear raises the critical stress. Hence, it appears that the tear has a stabilizing effect with regard to detachment propagation in this sense, and that this stabilizing effect is more pronounced with the inclusion of the meridian displacements.

The results for the myopic eye support the clinical finding of an increased prevalence of retinal detachment in myopic eyes and provide insight into the potential causation for the increased prevalence. From analysis of the *energy release rate*, it was seen that at severe levels of myopia, even in the absence of applied stress acting on the retina, a sufficient energy release for detachment propagation was achieved at both the posterior and the superior regions of the retina. Correspondingly, the critical stress for detachment propagation was

found to be lower for the myopic retina when compared to that of the emmetropic retina at both locations. For the critical stress at the posterior pole, the evolution of myopia led to the development of unstable wells in the threshold paths, indicating that although detachment was more likely, it may not occur in as catastrophic a manner for this case. The results suggest that, for the emmetropic eye, detachment is more resistant to propagation in a posterior direction from the equator. However, the myopic retina is far less resistant to detachment propagation posterior from the equator of the eye due to the geometric changes associated with myopia. As macular retinal detachment can lead to permanent vision loss, this has severe clinical consequences.

5.1   Future Considerations

The current axisymmetric mathematical models for both the emmetropic eye and the myopic eye do not allow for consideration of several important phenomena with regards to retinal detachment. First, it is important to consider the effects of gravity on retinal detachment. Axisymmetric deformation does not allow for the non-symmetric nature of gravity acting upon the eye as a person goes about their day. In order to better understand the mechanics of detachment under gravity it is necessary to simulate the detachment behavior for the various orientations of the eye when a person is standing, as well as when a person is lying down, and any arbitrary line of action of gravity in between these two extremes.

It is also of importance to study horseshoe tears, which are common in clinical observations. Axisymmetric detachment only allows for circular tears in the retina. In order to analyze the effects of gravity and the behavior of horseshoe tears, both centrally located and off center, the full set of non-axisymmetric equilibrium equations derived in Chapter 2 are needed. These equations will be functions of both the polar angle, θ, and the azimuth angle, φ. In the axisymmetric case, it was clear that detachment would propagate uniformly outward from the center of the detached region. When considering non-axisymmetric deformation, detachment can propagate at different rates in different directions. This will result in a transversality condition that employs a point wise criterion about the periphery of the detached area to establish the detachment boundary (see, Chapter 2). It is proposed that the detachment boundary will advance along the path of steepest decent that most

efficiently releases energy.

The relevant relations for the strain, rotation, and bending measures for the spherical geometries associated with the emmetropic eye under non-axisymmetric conditions were given in Section 2.2.4. The corresponding equations of equilibrium for non-axisymmetric deformations of a spherical shell are taken from Eqs. (2.123) and (2.124) as

$$\frac{\partial}{\partial\varphi}\left(\sin\varphi N_{\varphi\varphi}^{(j)}\right) + \frac{\partial}{\partial\theta}\left(N_{\varphi\theta}^{(j)}\right) - \cos\varphi N_{22}^{(j)} + \sin\varphi Q_{\varphi}^{(j)} = -R\sin\varphi\left(q_1 + \hat{\tau}_1^{(j)}\right) \qquad (5.1a)$$

$$\frac{\partial}{\partial\varphi}\left(\sin\varphi N_{\varphi\theta}^{(j)}\right) + \frac{\partial}{\partial\theta}\left(N_{\theta\theta}^{(j)}\right) + \cos\varphi N_{\varphi\theta}^{(j)} + \sin\varphi Q_{\theta}^{(j)} = -R\sin\varphi\left(q_2 + \hat{\tau}_2^{(j)}\right) \qquad (5.1b)$$

$$\frac{\partial}{\partial\varphi}\left(\sin\varphi Q_{\varphi}^{(j)}\right) + \frac{\partial}{\partial\theta}\left(Q_{\theta}^{(j)}\right) - \sin\varphi\left(N_{\varphi\varphi}^{(j)} + N_{\theta\theta}^{(j)}\right) = R\sin\varphi\left(q_3 + \hat{\sigma}_j\right) \qquad (5.1c)$$

where

$$Q_{\varphi}^{(j)} = \frac{1}{R\sin\varphi}\left[\frac{\partial}{\partial\varphi}\left(\sin\varphi M_{\varphi\varphi}^{(j)}\right) + \frac{\partial}{\partial\theta}\left(M_{\varphi\theta}^{(j)}\right) - \cos\varphi M_{\theta\theta}^{(j)}\right] \qquad (5.2a)$$

$$Q_{\theta}^{(j)} = \frac{1}{R\sin\varphi}\left[\frac{\partial}{\partial\varphi}\left(\sin\varphi M_{\varphi\theta}^{(j)}\right) + \frac{\partial}{\partial\theta}\left(M_{\theta\theta}^{(j)}\right) + \cos\varphi M_{\varphi\theta}^{(j)}\right] \qquad (5.2b)$$

In Eqs. (5.1), q_j are the components of the generalized loading parameter and $\hat{\sigma}_j$, $\hat{\tau}_1^{(j)}$, and $\hat{\tau}_2^{(j)}$ are Lagrange multipliers that ensure continuity of the transverse and meridian displacements of the shell layers in the intact region and in the contact zone.

The influence of gravity on retinal detachment propagation and the critical detachment behavior of horseshoe tears in the retina can be investigated through Eqs. (5.1) and (5.2), in conjunction with Eqs. (2.86)-(2.90). Continuing to quantify the contributions of the various causes of retinal detachment through mathematical modeling, such as that found in this study, can aid physicians in better understanding the phenomena and promote thought on alternative treatment procedures.

References

[1] Akiba, J., 1993. Prevalence of posterior vitreous detachment in high myopia. *Ophthalmology*, 100(9), 1384-1388.

[2] Alkuraya, H., 2011. Myopic foveoschisis: A common complication in high myopia. *Retinal Physician*, March 2011.

[3] Atchison, D.A., Jones, C.E., Schmid, K.L., Pritchard, N., Pope, J.M., Strugnell, W.E., and Riley, R.A., 2004. Eye shape in emmetropia and myopia. *Invest. Ophthalmol. Vis. Sci.*, 45(10), 3380-3386.

[4] Atchison, D.A., Pritchard, N., Schmid, K.L., Scott, D.H., Jones, C.E. and Pope, J.M., 2005. Shape of the retinal surface in emmetropia and myopia. *Invest. Ophthalmol. Vis. Sci.*, 46(8), 2698-2707.

[5] Avtar, R. and Srivastava, S., 2017. Mathematical modeling of exudative retinal detachment. *Appl. Math.*, 8(01), 44-56.

[6] Bhardwaj, R., Ziegler, K., Seo, J.H., Ramesh, K.T., and Nguyen, T.D., 2014. A computational model of blast loading on the human eye. *Biomech. Model. Mech.*, 13(1), 123-140.

[7] Bottega, W.J., 1983. A growth law for propagation of arbitrary shaped delaminations in layered plates. *Int. J. Solids Structures*, 19(11), 1009-1017.

[8] Bottega, W.J., 1988a. Peeling of a cylindrical layer. *Int. J. Fract.*, 38(1), 3-14.

[9] Bottega, W.J., 1988b. On thin film delamination growth in a contracting cylinder. *Int. J. Solids Struct.*, 24(1), 13-26.

[10] Bottega, W.J., 1988c. Debonding of a predeflected segment of layer from the wall of a contracting cavity. *Eng. Fract. Mech.*, 31(6), 1001-1008.

[11] Bottega, W.J., 1993. On the separation of concentric elastic rings. *Int. J. Mech. Sci.*, 35(10), 851-866.

[12] Bottega, W.J., Bishay, P.L., Prenner, J.L., and Fine, H.F., 2013. On the mechanics of a detaching retina. *Math. Med. Biol.*, 30(4), 287-310.

[13] Celorio, J.M. and Pruett, R.C., 1991. Prevalence of lattice degeneration and its relation to axial length in severe myopia. *Am. J. Ophthalmol.*, 111(1), 20-23.

[14] Chen, K., Rowley, A.P., and Weiland, J.D., 2010. Elastic properties of porcine ocular posterior soft tissues. *J. Biomed. Mater. Res. Part A*, 93, 634-645.

[15] Chen, K., Rowley, A.P., Weiland, J.D., and Humayun, M.S., 2014. Elastic properties of human posterior eye. *J. Biomed. Mater. Res. Part A*, 102(6), 2001-2007.

[16] Chou, T. and Siegel, M., 2012. A mechanical model of retinal detachment. *Phys. Biol.*, 9(4), 046001.

[17] David, T., Smye, S., James, T., and Dabbs, T., 1997. Time-dependent stress and displacement of the eye wall tissue of the human eye. *Med. Eng. Phys.*, 19(2), 131-139.

[18] David, T., Smye, S., Dabbs, T., and James, T., 1998. A model for the fluid motion of vitreous humour of the human eye during saccadic movement. *Phys. Med. Biol.*, 43(6), 1385-1399.

[19] Dyson, R., Fitt, A.J., Jensen, O.E., Mottram, N., Miroshnychenko, D., Naire, S., Ocone, R., Siggers, J.H., and Smithbecker, A., 2004. Post re-attachment retinal re-detachment. *Proceedings of the fourth medical study group, University of Strathclyde, Glasgow.*

[20] Feldkaemper, M. and Schaeffel, F., 2013. An updated view on the role of dopamine in myopia. *Exp. Eye Res.*, 114, 241-251.

[21] Flügge, W., 1960. *Stesses in Shells*, Springer, Berlin, Germany.

[22] Foster, W.J. and Chou, T., 2004. Physical mechanisms of gas and perfluoron retinopexy and sub-retinal fluid displacement. *Phys. Med. Biol.*, 49(13), 2989-2997.

[23] Foster, W.J., Dowla, N., Joshi, S.Y., and Nikolaou, M., 2010. The fluid mechanics of scleral buckling surgery for the repair of retinal detachment. *Graefes Arch. Clin. Exp. Ophthalmol.*, 248(1), 31-36.

[24] Friedenwald, J.S., 1937. Contribution to the theory and practice of tonometry. *Am. J. Ophthalmol.*, 20(10), 985-1024.

[25] Gariano, R.F. and Kim, C.H., 2004. Evaluation and management of suspected retinal detachment. *Am. Fam. Phys.*, 69(7), 1691-1698.

[26] Ge, P., Bottega, W.J., Prenner, J.L., and Fine, H.F., 2016. On the influence of an equatorial cerclage on closure of posterior retinal detachment. *Math. Med. Biol.*, 33(4), 417-433.

[27] Ge, P., Bottega, W.J., Prenner, J.L., and Fine, H.F., 2017. On the behavior of an eye encircled by a scleral buckle. *J. Math. Biol.*, 74(1-2), 313-332.

[28] Gella, L., Raman, R., and Sharma, T., 2011. Evaluation of in vivo human retinal morphology and function in myopes. *Curr. Eye Res.*, 36(10), 943-946.

[29] Gilmartin, B., Nagra, M., and Logan, N.S., 2013. Shape of the posterior vitreous chamber in human emmetropia and myopia. *Invest. Ophthalmol. Vis. Sci.*, 54(12), 7240-7251.

[30] Gonzalez, G. and Fitt, A.D., 2003. The mathematical modelling of human eyes-a PhD study. *Mathematics Today*, 20-25.

[31] Greene, P.R., 1980. Mechanical considerations in myopia: relative effects of accommodation, convergence, intraocular pressure, and the extraocular muscles. *Am. J. Optom. Physiol. Opt.*, 57(12), 902-914.

[32] Griffith, A.A., 1921. The phenomena of rupture and flow in solids. *Philos. Trans. R. Soc. Lond. A*, 221, 106-119.

[33] Hung, G.K., Mahadas, K., and Mohammad, F., 2016. Eye growth and myopia development: Unifying theory and Matlab model. *Comput. Biol. Med.*, 70, 106-118.

[34] Ishii, K., Iwata, H., and Oshika, T., 2011. Quantitative evaluation of changes in eyeball shape in emmetropization and myopic changes based on elliptic fourier descriptors. *Invest. Ophthalmol. Vis. Sci.*, 52(12), 8585-8591.

[35] Ismail, Z., Fitt, A., and Please, C., 2014. The deformation of human eyeball when undergoing scleral buckling. *Appl. Mech. Mater.*, 695, 544-547.

[36] Kain, H.L., 1984. A new model for examining chorioretinal adhesion experimentally. *Arch. Ophthalmol.*, 102(4), 608-611.

[37] Kita, M. and Marmor, M.F., 1992. Retinal adhesive force in living rabbit, cat, and monkey eyes. Normative data and enhancement by mannitol and acetazolamide. *Invest. Ophthalmol. Vis. Sci.*, 33(6), 1879-1882.

[38] Kita, M., Negi, A., Kawano, S., Honda, Y., and Maegawa, S., 1990. Measurement of retinal adhesive force in the in vivo rabbit eye. *Invest. Ophthalmol. Vis. Sci.*, 31(4), 624-628.

[39] Keeling, S.L., Propst, G., Stadler, G., and Wackernagel, W., 2009. A mathematical model for the deformation of the eyeball by an elastic band. *Math. Med. Biol.*, 26(2), 165-185.

[40] Kobayashi, A.S., Woo, S.Y., Lawrence, C., and Schlegel, W.A., 1971. Analysis of the corneo-scleral shell by the method of direct stiffness. *J. Biomechanics*, 4(5), 323-330.

[41] Koiter, W.T., 1959. A consistent first approximation in the general theory of thin elastic shells. *Proc. I.U.T.A.M. Symp. on the Theory of Thin Elastic Shells*, North-Holland, Amsterdam, 12-33.

[42] Lakawicz, J.M., Bottega, W.J., Prenner, J.L., and Fine, H.F., 2015. An analysis of the mechanical behaviour of a detaching retina. *Math. Med. Biol.*, 32(2), 137-161.

[43] Lakawicz, J.M., Bottega, W.J., Fine, H.F., and Prenner, J.L., 2017. *On the mechanics of myopia and its influence on retinal detachment.* Revision in review.

[44] Lanchares, E., Buey, M.A.D., Cristbal, J.A., Calvo, B., Ascaso, F.J., and Malv, M., 2016. Computational simulation of scleral buckling surgery for rhegmatogenous retinal detachment: On the effect of the band size on the myopization. *J. Ophthalmol.*, 2016.

[45] Lin, T., Grimes, P.A., and Stone, R.A., 1993. Expansion of the retinal pigment epithelium in experimental myopia. *Vision Res.*, 33(14), 1881-1885.

[46] Liu, X., Wang, L., Wang, C., Sun, G., Liu, S., and Fan, Y., 2013. Mechanism of traumatic retinal detachment in blunt impact: a finite element study. *J. Biomechanics*, 46(7), 1321-1327.

[47] Love, A.E.H., 1944. *A Treatise on the Mathematical Theory of Elasticity*, 4th ed., Dover, New York, US.

[48] McBrien, N.A., Jobling, A.I., and Gentle, A., 2009. Biomechanics of the sclera in myopia: extracellular and cellular factors. *Optom. Vis. Sci.*, 86(1), E23-E30.

[49] Meskauskas, J., Repetto, R., and Siggers, J.H., 2012. Shape change of the vitreous chamber influences retinal detachment and reattachment processes: is mechanical stress during eye rotations a factor? *Invest. Ophthalmol. Vis. Sci.*, 53(10), 6271-6281.

[50] Michels, R.G., Thompson, J.T., Rice, T.A., and Freund, D., 1986. Effect of scleral buckling on vector forces caused by epiretinal membranes. *Am. J. Ophthalmol.*, 102(4), 449-451.

[51] Miles, F.A., and Wallman, J., 1990. Local ocular compensation for imposed local refractive error. *Vision Res.*, 30(3), 339-349.

[52] Mitry, D., Charteris, D.G., Fleck, B.W., Campbell, H., and Singh, J., 2010. The epidemiology of rhegmatogenous retinal detachment: geographical variation and clinical associations. *Br. J. Ophthalmol.*, 94(6), 678-684.

[53] Møllmann, H., 1981. *Introduction to the Theory of Thin Shells*, John Wiley & Sons, New York, US.

[54] Mow, C.C., 1968. A theoretical model of the cornea for use in studies of tonometry. *Bull. Math. Biol.*, 30(3), 437-453.

[55] Naghdi, P.M., 1956. Note on the equations of shallow elastic shells. *Quart. Appl. Math.*, 14(3), 331-333.

[56] Naghdi, P.M., 1963. Foundations of elastic shell theory. *Progress in Solid Mechanics* (Edited by I.N. Sneddon and R. Hill), 4, 1-90, North-Holland.

[57] Nelson, M.R., King, J.R., and Jensen, O.E., 2013. Buckling of a growing tissue and the emergence of two-dimensional patterns. *Math. Biosci.*, 246(2), 229-241.

[58] Pavlou, M.J., 2018. *A Mechanics Based Analytical Model of Vitreous Motion and Vitreous Detachment in the Human Eye When Subjected to Saccadic Movement.* Doctoral Dissertation, Rutgers University, NJ.

[59] Pruett, R.C., 1988. Progressive myopia and intraocular pressure: what is the linkage?: A literature review. *Acta Ophthalmol.*, 66(S185), 117-127.

[60] Reissner, E., 1941. A new derivation of the equations for the deformation of elastic shells. *Am. Jour. Math.*, 63(1), 177-184.

[61] Reissner, E., 1949 (March). *Small bending and stretching of sandwich-type shells.* NACA TN 1832.

[62] Repetto, R., Ghigo, I., Seminara, G., and Ciurlo, C., 2004. A simple hydro-elastic model of the dynamics of a vitreous membrane. *J. Fluid Mech.*, 503, 1-14.

[63] Repetto, R., Stocchino, A., and Cafferata, C., 2005. Experimental investigation of vitreous humour motion within a human eye model. *Phys. Med. Biol.*, 50(19), 4729-4743.

[64] Repetto, R., Tatone, A., Testa, A., and Colangeli, E., 2011. Traction on the retina induced by saccadic eye movements in the presence of posterior vitreous detachment. *Biomech. Model. Mechanobiol.*, 10(2), 191-202.

[65] Rodriguez, E.K., Hoger, A., and McCulloch, A.D., 1994. Stress-dependent finite growth in soft elastic tissues. *J. Biomechanics*, 27(4), 455-467.

[66] Rosenfield, M. and Gilmartin, B., 1998. *Myopia and Nearwork*, Butterworth-Heinemann, Boston, US.

[67] Rossi, T., Boccassini, B., Esposito, L., Clemente, C., Iossa, M., Placentino, L., and Bonora, N., 2012. Primary blast injury to the eye and orbit: finite element modeling. *Invest. Ophthalmol. Vis. Sci.*, 53(13), 8057-8066.

[68] Sanders, J.L., 1959. *An improved first-approximation theory for thin shells.* NASA TR-R24.

[69] Schaeffel, F., Glasser, A., and Howland, H.C., 1988. Accommodation, refractive error and eye growth in chickens. *Vision Res.*, 28(5), 639-657.

[70] Schwartz, N.J., Mackay, R.S., and Sackman, J.L., 1966. A theoretical and experimental study of the mechanical behavior of the cornea with application to the measurement of intraocular pressure. *Bull. Math. Biol.*, 28(4), 585-643.

[71] Sebag, J., 1987. Age-related changes in human vitreous structure. *Graefes Arch. Clin. Exp. Ophthalmol.*, 225(2), 89-93.

[72] Skalak, R., 1981. Growth as a finite displacement field. *Proceedings of the IUTAM Symposium on Finite Elasticity*, 347-355, Springer Netherlands.

[73] Smith, E.L., Harwerth, R.S., Crawford, M.L., and von Noorden, G.K., 1987. Observations on the effects of form deprivation on the refractive status of the monkey. *Invest. Ophthalmol. Vis. Sci.*, 28(8), 1236-1245.

[74] Soedel W., 1993. *Vibrations of Shells and Plates.* 2nd ed., Marcel Dekker, New York, US.

[75] Stitzel, J.D., Duma, S.M., Cormier, J.M., and Herring, I.P., 2002. A nonlinear finite element model of the eye with experimental validation for the prediction of globe rupture. *Stapp Car Crash J.*, 46, 81-102.

[76] Timoshenko, S. and Woinowsky-Krieger, S., 1959. *Theory of Plates and Shells*, McGraw-Hill, New York, US.

[77] Uchio, E., Ohno, S., Kudoh, J., Aoki, K., and Kisielewicz, L.T., 1999. Simulation model of an eyeball based on finite element analysis on a supercomputer. *Br. J. Ophthalmol.*, 83(10), 1106-1111.

[78] Ventsel, E. and Krauthammer, T., 2001. *Thin plates and shells: theory, analysis, and applications*, Marcel Dekker, New York, US.

[79] Verkicharla, P.K., Mathur, A., Mallen, E.A., Pope, J.M., and Atchison, D.A., 2012. Eye shape and retinal shape, and their relation to peripheral refraction. *Ophthalmic Physiol. Opt.*, 32(3), 184-199.

[80] Voltairas, P.A., Fotiadis, D.I., and Massalas, C.V., 2001. Elastic stability of silicone ferrofluid internal tamponade (SFIT) in retinal detachment surgery. *J. Magn. Magn. Mater.*, 225(1), 248-255.

[81] Wallman, J., Turkel, J., and Trachtman, J., 1978. Extreme myopia produced by modest change in early visual experience. *Science*, 201(4362), 1249-1251.

[82] Wallman, J., Gottlieb, M.D., Rajaram, V., and Fugate-Wentzek, L.A., 1987. Local retinal regions control local eye growth and myopia. *Science*, 237(4810), 73-77.

[83] Wang, F., Lee, H.P., and Lu, C., 2007. Biomechanical effect of segmental scleral buckling surgery. *Curr. Eye Res.*, 32(2), 133-142.

[84] Wilkinson, R.P. and Rice, T.A., 1997. *Michels Retinal Detachment*, 2nd ed., Mosby, St. Louis, US.

[85] Wollensak, G., Spoerl, E., Grosse, G., and Wirbelauer, C., 2006. Biomechanical significance of the human internal limiting lamina. *Retina*, 26(8), 965-968.

[86] Woo, S.L., Kobayashi, A.S., Lawrence, C., and Schlegel, W.A., 1972. Mathematical model of the corneo-scleral shell as applied to intraocular pressure-volume relations and applanation tonometry. *Ann. Biomed. Eng.*, 1(1), 87-98.

[87] Young, F.A., 1963. The effect of restricted visual space on the refractive error of the young monkey. *Invest. Ophthalmol. Vis. Sci.*, 2(6), 571-577.